

DEVELOPMENT OF AN INTEGRATED RESONANT MEMS TEMPERATURE
SENSOR

A THESIS SUBMITTED TO
THE GRADUATE SCHOOL OF NATURAL AND APPLIED SCIENCES
OF
MIDDLE EAST TECHNICAL UNIVERSITY

BY

TALHA KÖSE

IN PARTIAL FULFILLMENT OF THE REQUIREMENTS
FOR
THE DEGREE OF MASTER OF SCIENCE
IN
MECHANICAL ENGINEERING

JANUARY 2016

Approval of the thesis:

**DEVELOPMENT OF AN INTEGRATED RESONANT MEMS TEMPERATURE
SENSOR**

submitted by **TALHA KÖSE** in partial fulfillment of the requirements for the degree of
**Master of Science in Mechanical Engineering Department, Middle East Technical
University** by,

Prof. Dr. Gülbin Dural Ünver

Dean, Graduate School of **Natural and Applied Sciences**

Prof. Dr. Tuna Balkan

Head of Department, **Mechanical Eng.**

Assist. Prof. Dr. Kıvanç Azgın

Supervisor, **Mechanical Eng. Dept., METU**

Prof. Dr. Tayfun Akın

Co-supervisor, **Electrical and Electronics Eng. Dept., METU**

Examining Committee Members:

Prof. Dr. Mehmet Çalışkan

Mechanical Eng. Dept., METU

Assist. Prof. Dr. Kıvanç Azgın

Mechanical Eng. Dept., METU

Prof. Dr. Tayfun Akın

Electrical and Electronics Eng. Dept., METU

Assist. Prof. Dr. Fatma Nazlı Dönmezer Akgün

Mechanical Eng. Dept., METU

Assist. Prof. Dr. Necmi Bıyıklı

Ins. of Materials Science and Nanotechnology, Bilkent Uni.

I hereby declare that all information in this document has been obtained and presented in accordance with academic rules and ethical conduct. I also declare that, as required by the rules and conduct, I have fully cited and referenced all materials and results that are not original to this work.

Name, Last Name: Talha Köse

Signature :

ABSTRACT

DEVELOPMENT OF AN INTEGRATED RESONANT MEMS TEMPERATURE SENSOR

Köse, Talha

M.S., Department of Mechanical Engineering

Supervisor : Assist. Prof. Dr. Kıvanç Azgın

Co-Supervisor : Prof. Dr. Tayfun Akın

January 2016, 137 pages

This thesis presents the design, fabrication and characterization of a high performance, integrated, resonant MEMS temperature sensor, and temperature compensation of a capacitive MEMS accelerometer. Two different double-ended-tuning-fork (DETF) type resonator designs are developed and characterized for temperature sensing. The strain-amplifying beam structure is added to the DETF resonators in order to enhance thermal strain induced on the DETF tines due to the different thermal expansion coefficients of the substrate and the sensor structure. Two different supplementary temperature sensor designs have been demonstrated in order to compare the effectiveness of the strain-amplifying beam, i.e., the doubly-clamped DETF resonators, and one-end-free DETF resonators. Two DETF resonators with different geometric properties have been used in the temperature sensor designs in order to verify analytical equations representing the

operation of DETF resonators as temperature sensors. Finite Element Analysis simulations (modal and thermo-mechanical) have been conducted for each of the temperature sensor designs. To realize real-time data acquisition from the temperature sensors, a read-out circuit which sustains self-resonance of the DETF resonators has been designed and demonstrated with the circuit simulations. The co-fabrication of the MEMS temperature sensors and MEMS accelerometer have been demonstrated by on-chip integration of the devices. This integration enables precise temperature measurements by removing the thermal lag between the temperature sensor and the MEMS accelerometer to be temperature-compensated. After fabrication, characterization tests have pointed out a good vacuum environment (pressure inside the sensor dies in range of 10-100 mTorr) which corresponds to quality factors in the order of 10000. The system-level temperature tests (from -20 °C to 60 °C) are done while the accelerometer and two temperature sensors were simultaneously operated in closed-loop. Temperature coefficient of frequency values (TCf) of 730 ppm/K and 636 ppm/K have been achieved with the proposed temperature design, which reveals an improvement in sensitivity (TCf) up to 2.4 times when compared to doubly-clamped DETF resonators, and an improvement up to 35 times improvement when compared to the one-end-free DETF resonators. Minimum detectable temperature attained with the proposed temperature sensor designs has been reported as 1.1 mK. The temperature compensation of MEMS accelerometer has resulted in an improvement up to 830 times by reducing the temperature dependence of the accelerometer output from 1164 $\mu\text{g}/^\circ\text{C}$ to 1.4 $\mu\text{g}/^\circ\text{C}$. The noise performances of the MEMS accelerometers used in this study points out bias instability of 10 μg up to integration time of 100 seconds, and the velocity random walk of 13 $\mu\text{g}/\sqrt{\text{Hz}}$.

Keywords: MEMS DETF resonator, double-ended-tuning-fork, capacitive MEMS accelerometer, temperature compensation, MEMS resonant temperature sensor, temperature sensing

ÖZ

ENTEGRE REZONANT MEMS SICAKLIK DUYARGASI GELİŞTİRİLMESİ

Köse, Talha

Yüksek Lisans, Makina Mühendisliği
Tez Yöneticisi : Yar. Doç. Dr. Kıvanç Azgın
Ortak Tez Yöneticisi : Prof. Dr. Tayfun Akın

Ocak 2016, 137 pages

Bu tez yüksek performanslı entegre bir rezonant MEMS sıcaklık sensörünün tasarım, üretim ve karakterizasyonunu ve önerilen MEMS sıcaklık sensörlerinin bir uygulamasını göstermek için sığasal bir MEMS ivmeölçerin sıcaklık telafisini sunmaktadır. MEMS sıcaklık sensörü tasarımlarında, isimleri Dizayn #1 ve Dizayn #2 olarak belirlenen iki farklı yapıdaki çift-sonlu-ayar-çatalı (DETF) tipi rezonatörler kullanılmıştır. Farklı termal genleşme katsayıları olan taban ve sensör yapıları sebebiyle çatal dişlerinin üzerinde oluşan termal uzamayı artırmak için uzama-artırıcı giriş yapısı DETF rezonatörlerine eklenmiştir. Uzama-artırıcı giriş yapısının etkinliğini karşılaştırabilmek için, çift- taraflı sıkıştırılmalı DETF rezonatörleri ve bir ucu serbest DETF rezonatörleri kullanılarak, iki farklı tamamlayıcı sıcaklık sensörü tasarımı sunulmuştur. DETF rezonatörlerinin sıcaklık sensörü olarak çalışmasını modelleyen analitik denklemlerin

doğrulanması için, farklı geometrik özelliklere sahip iki DETF rezonatörü sıcaklık sensörü tasarımlarında kullanılmıştır. Her bir sıcaklık sensörü tasarımı için sonlu-eleman simülasyonları (modal ve termo-mekanik) yürütülmüştür. Sıcaklık sensörlerinden gerçek zamanlı veri toplamayı gerçekleştirmek için, DETF rezonatörlerin kendi kendine rezonans titreşimini sürdürebilecek bir okuma devresi tasarlanmış ve devre simülasyonları ile gösterilmiştir. Benzer şekilde, MEMS ivmeölçerlerin mekanik tasarımı ve okuma devresi ile ilgili kısa açıklamalar sunulmuştur. Sıcaklık telafisi yapılacak olan MEMS ivmeölçer ile sıcaklık sensörü arasındaki termal gecikmeyi ortadan kaldırarak doğru sıcaklık ölçümlerini mümkün kılan, sensörlerin çip-üzeri entegrasyonu ile MEMS sıcaklık sensörlerinin ve ivmeölçerlerin ortak üretimi yürütülmüştür. Üretimden sonra, karakterizasyon testleri sensör çipi içinde 10000 seviyesinde kalite faktörüne denk gelen vakum ortamı olduğunu göstermiştir (Sensör çipi içerisindeki basınç 10-100 mTorr arasındadır). İvmeölçer ve sıcaklık sensörlerinin eşzamanlı kapalı devrede çalıştırıldığı sistem-seviyesi sıcaklık testleri, 20 °C ve 60 °C arasında yürütülmüştür. Önerilen sıcaklık sensörü tasarımıyla, 730 ppm/K ve 636 ppm/K frekansın sıcaklık katsayısı (TCf) değerlerine ulaşılmıştır. Bu değerler, çift- taraflı sıkıştırılmalı rezonatörler ile karşılaştırıldığında hassasiyette (TCf değerlerinde) 2.4 kata kadar, tek-ucu-serbest DETF rezonatörler ile karşılaştırıldığında 35 kata kadar iyileştirmeyi göstermektedir. Önerilen sıcaklık sensörü tasarımlarıyla saptanabilen en az sıcaklık 1.1 mK olarak raporlanmıştır. MEMS ivmeölçerlerin sıcaklık telafisi, ivmeölçerlerin çıkışının sıcaklık bağılılığı 1,164 $\mu\text{g}/^\circ\text{C}$ 'den 1.4 $\mu\text{g}/^\circ\text{C}$ 'ye düşürülerek 830 kat iyileştirmeyle sonuçlandırılmıştır. Bu tezde kullanılan MEMS ivmeölçerlerin gürültü değerleri 100 saniye entegrasyon zamanına kadar 10 μg offset kararsızlığı ve 13 $\mu\text{g}/\sqrt{\text{Hz}}$ rastgele kaymayı göstermektedir.

Anahtar Kelimeler: MEMS DETF rezonatör, çift-sonlu-ayar-çatalı, sığasal MEMS ivmeölçer, sıcaklık telafisi, rezonans tabanlı MEMS sıcaklık duyargası, sıcaklık ölçümü.

To the Cirkin Palace.

ACKNOWLEDGEMENTS

First and foremost, I would like to express my deep and sincere thanks to my thesis advisor, Assist. Prof. Kivanc Azgin, and my thesis co-advisor, Prof. Dr. Tayfun Akin, for their support, guidance and encouragement during my graduate studies.

I would like to express my deep gratitude to Dr. Said Emre Alper for sharing his knowledge and always-friendly attitude during my M.Sc. study. I have learned a lot from Dr. Alper about how to be a professional.

I would like to thank to my colleagues, Yunus Terzioglu, Ulaş Aykutlu and Ferhat Yeşil for sharing their knowledge on read-out electronics. I would have been in trouble without their help and support. Special thanks to Dr. M. Mert Torunbalci, for sharing his talents in clean-room as well as Hasan Dogan Gavcar and Gulsah Demirhan during the fabrication process. I also thank to Ozan Ertürk and Ramazan Çetin for their supports throughout this thesis study.

I would like to thank to my special friends, Utku Göreke, Fatih Küçüksubaşı, Serkan Ülgen, Berkman Kantar, Ahmet Ademoğlu, Batu Aksu, Özenç Güngör, Family Vural, Family Çelik, Family Bayram, Tolga Kurşun, Arda Akay, Anil Alan, Can Baloglu, Hüseyin Akartuna, Özkan İçigen, Taner Çiçek, Hüseyin Ince and Sinan Ilgat, although I know that there is no way to express my gratitude to have you around me.

Last but not least, I would like to thank to my family, Ömer Köse, Gülsüm Köse, my elder brother Mustafa Köse and my little brother Ahmet Turan Köse for their endless support, love and encouragement throughout my entire life.

TABLE OF CONTENTS

ABSTRACT	v
ÖZ	vii
ACKNOWLEDGEMENTS	x
TABLE OF CONTENTS	xi
LIST OF FIGURES	xiv
LIST OF TABLES	xxii
CHAPTERS	
1. INTRODUCTION	1
1.1 Overview of MEMS Resonators	2
1.2 Overview of Temperature Compensation Techniques in MEMS Sensors.....	3
1.3 Objectives and Organization of Thesis Study	5
2. DESIGN AND MODELLING OF MEMS DETF RESONATORS AND ACCELEROMETERS	9
2.1 Design of Resonant MEMS Temperature Sensors.....	10
2.1.1 Operation Principles of MEMS DETF Resonators Used in This Study	10
2.1.1.1 Capacitive Actuation.....	14
2.1.1.2 Capacitive Detection	19
2.1.2. Mechanical Design of MEMS DETF Resonators Used in This Study	22
2.1.2.1. Operation Principles of MEMS DETF Resonators as MEMS Temperature Sensor	22

2.1.2.2	Determination of Geometric Properties of DETF Parameters	35
2.1.3.	Finite Element Modeling (FEM) Simulations of Temperature Sensors	40
2.1.3.1.	Modal Simulations of the Resonator Systems.....	40
2.1.3.2	Thermo-mechanical Simulations of the Temperature Sensors	49
2.2	Design of Read-out Electronics of Resonant MEMS Temperature Sensors	56
2.2.1	Overview of Read-out Electronics Designed for MEMS Temperature Sensors	56
2.2.2	LT Spice Simulations of Read-out Electronics of MEMS Temperature Sensors	58
2.3	Design of Capacitive MEMS Accelerometers.....	64
2.3.1	Operation Principle of Capacitive MEMS Accelerometers	65
2.3.2	Mechanical Design of the Sensing Element of MEMS Accelerometer	66
2.3.3	FEM Simulations of MEMS Accelerometer	70
2.3.3.1	Modal Simulations of the Sensing Element of MEMS Accelerometer ...	71
2.4	Analog Force Feedback Read-out Circuit for the Sensing Element of MEMS Accelerometer	72
2.5	Temperature Effects on the Accelerometer Output	74
2.6	Summary.....	74
3.	FABRICATION OF MEMS DETF RESONATORS AND ACCELEROMETERS	77
3.1	Fabrication of Sensor Structures.....	78
3.2	Fabrication of Cap Wafer for Hermetic Encapsulation	80
3.3	Fabrication Results	82
3.4	Summary.....	84
4.	TESTS AND MEASUREMENT RESULTS.....	85

4.1	Characterization Tests	85
4.1.1	Characterization Test Results of MEMS Resonators.....	86
4.1.2	Characterization Test Results of MEMS Accelerometers	90
4.2	Test Setup Preparation for the System-Level Temperature Tests	91
4.2.1	Preparation of Sensor Package.....	92
4.2.2	Preparation of Analog Force-Feedback Read-Out Package for Accelerometer	93
4.2.3	Preparation of Test PCB.....	94
4.2.4	Implementation of Test Setup for the System-Level Tests	96
4.3	Measurement Results of System-Level Temperature Tests	98
4.3.1.1	System-Level Test Results of MEMS Resonators	98
4.3.1.2	System-Level Test Results of MEMS Resonators in Design 1A	100
4.3.1.2	System-Level Test Results of MEMS Resonators in Design 1C.....	102
4.3.1.3	System-Level Test Results of MEMS Resonators in Design 2A.....	105
4.3.1.4	System-Level Test Results of MEMS Resonators in Design 2B.....	107
4.3.2	System-Level Test Results of MEMS Accelerometers.....	113
4.3.3	Temperature Compensation of Accelerometer Output by Using Resonator Data	117
4.4	Summary and Conclusion	122
5.	CONCLUSION AND FUTURE WORK	125
	REFERENCES.....	129

LIST OF FIGURES

FIGURES

Figure 2.1: a) Schematic of the DETF resonator structures denoted by Design #1, b) Schematic of the DETF resonator structures denoted by Design #2.....	11
Figure 2.2: Schematic of the tines of DETF structure while deflected in out-of-phase operation mode and the associated second order mass-spring-damper system are presented.....	12
Figure 2.3: Half-power bandwidth illustration on a typical frequency-response plot. ...	13
Figure 2.4: The capacitance formed between the proof mass of the resonators and the fixed drive electrodes can be seen above. DETF resonator structure used in Design #1 can be seen on the left while the DETF structure of Design #2 is presented on the right.	15
Figure 2.5: Schematic of the capacitive sensing mechanism.	20
Figure 2.6: a) Resonator layout of Design 1A, b) Resonator layout of Design 1C, c) Resonator layout of Design 2A, and d) Resonator layout of Design 2B.	24
Figure 2.7: Simplified schematic of the cross-sectional view of a sensor die showing 1-D thermal deflections under temperature change.....	25
Figure 2.8: Simplified schematic of the resonator system offered in Design 1A. To avoid any confusion and for the sake of simplicity of the governing equations, only one tine of the resonators are shown in this figure. Note that the hatched areas represent the anchor regions while others show the suspended sensor structures in top view.	26
Figure 2.9: Simplified schematic of the resonator system offered in Design 1C. To avoid any confusion and for the sake of simplicity of the governing equations, only one tine of the resonators are shown in this figure. Note that the hatched areas represent the anchor regions while others show the suspended sensor structures in top view.	32

Figure 2.10: Simplified schematic of the resonator system offered in Design 2B. To avoid any confusion and for the sake of simplicity of the governing equations, only one tine of the resonators are shown in this figure. Note that the hatched areas represent the anchor regions while others show the suspended sensor structures in top view.....34

Figure 2.11: Overview of the GUI created to determine the geometric parameters of the DETF resonators. **a)** The tab utilized to maximize TCf of the resonators by using the ratios of the key tine parameters. **b)** The tab utilized to see the frequency change of the long resonator with changing temperature for the entered geometric properties.....36

Figure 2.12: Modal simulation results obtained via CoventorWare for the resonators in Design 1A. Each resonator has two operation modes, called sibling modes, as presented in **a)** in-phase operation mode for the long resonator, **b)** out-of-phase operation mode for the long resonator, **c)** in-phase operation mode for the short resonator, and **d)** out-of-phase operation mode for the short resonator.43

Figure 2.13: Modal simulation results obtained via CoventorWare for the resonators in Design 1C. Each resonator has two operation modes, called sibling modes, as presented in **a)** out-of-phase operation mode for the long resonator, **b)** in-phase operation mode for the long resonator, **c)** in-phase operation mode for the short resonator, and **d)** out-of-phase operation mode for the short resonator.45

Figure 2.14: Modal simulation results obtained via CoventorWare for the resonators in Design 2A. Each resonator has two operation modes, called sibling modes, as presented in **a)** out-of-phase operation mode for the long resonator, **b)** in-phase operation mode for the long resonator, **c)** in-phase operation mode for the short resonator, and **d)** out-of-phase operation mode for the short resonator.47

Figure 2.15: Modal simulation results obtained via CoventorWare for the resonators in Design 2B. Each resonator has two operation modes, called sibling modes, as presented in **a)** in-phase operation mode for the long resonator, **b)** out-of-phase operation mode for the long resonator, **c)** in-phase operation mode for the short resonator and **d)** out-of-phase operation mode for the short resonator.49

Figure 2.16: Thermal simulation results of Design 1A. The simulation was held for the range in between -20 °C and 60 °C by collecting data for each 10 °C increment. The

resonance frequency shift of long resonator and the resonance frequency shift of long resonator for both operation modes can be seen in **a)** and **b)**, respectively. The resulting TCf for the long resonator is calculated as 638 ppm/K, whereas it is found as 172 ppm/K for the short resonator in Design 1A. The axial stress induced along the tines of DETF resonators at 60 °C is presented in **c)**. The axial stress induced on the tines of the long and short resonators is around 5-6 MPa, respectively. Note that the cap of the die is hidden in **c)** for the clear visualization.....51

Figure 2.17: Thermal simulation results of Design 1C. The simulation was held for the range in between -20 °C and 60 °C by collecting data for each 10 °C increment. The resonance frequency shift of long resonator and the resonance frequency shift of long resonator for both operation modes can be seen in **a)** and **b)**, respectively. The resulting TCf for the long resonator is calculated as 323 ppm/K and 351 ppm/K for the in-phase and out-of-phase operation modes, respectively, whereas it is found as 104 ppm/K and 127 ppm/K for the short resonator in Design 1C. The axial stress induced along the tines of DETF resonators at 60 °C is presented in **c)**. The axial stress induced on the tines of short and long DETF resonators is around 2-3 MPa. Note that the cap of the die is hidden in **c)** for the clear visualization.....52

Figure 2.18: Thermal simulation results of Design 2A. The simulation was held for the range in between -20 °C and 60 °C by collecting data for each 10 °C increment. The resonance frequency shift of long resonator and the resonance frequency shift of long resonator for both operation modes can be seen in **a)** and **b)**, respectively. The resulting TCf for the long resonator is calculated as 697 ppm/K, whereas it is found as 180 ppm/K for the short resonator in Design 2A. The axial stress induced along the tines of DETF resonators at 60 °C is presented in **c)**. The axial stress induced on the tines of the long resonator is around 5 MPa while it is around 4 MPa for the short resonator. Note that the cap of the die is hidden in **c)** for the clear visualization.....54

Figure 2.19: Thermal simulation results of Design 2B. The simulation was held for the range in between -20 °C and 60 °C by collecting data for each 10 °C increment. The resonance frequency shift of long resonator and the resonance frequency shift of long resonator for both operation modes can be seen in **a)** and **b)**, respectively. The resulting

TCf for the long resonator is calculated as -30 ppm/K, whereas it is found as -31 ppm/K for the short resonator in Design 2B. The axial stress induced along the tines of DETF resonators at 60 °C is presented in c). The axial stress induced on the tines of the both resonators is below 1 MPa. Note that the cap of the die is hidden in c) for the clear visualization.55

Figure 2.20: Schematic of the read-out circuit utilized to sustain self-resonance of the resonators in each design.58

Figure 2.21: a) Schematic of the read-out circuit presented with the components used in frequency response and transient response analyses. b) The result of frequency response analyses of the read-out circuit belonging to long DETF resonators in Design 2A and 2B.59

Figure 2.22: a) Schematic of the read-out circuit presented with the components used in frequency response and transient response analyses. b) The result of frequency response analyses of the read-out circuit belonging to long DETF resonators in Design 1A and 1C.60

Figure 2.23: a) Schematic of the read-out circuit presented with the components used in frequency response and transient response analyses. b) The result of frequency response analyses of the read-out circuit belonging to short DETF resonators in Design 2A and 2B.61

Figure 2.24: a) Schematic of the read-out circuit presented with the components used in frequency response and transient response analyses. b) The result of frequency response analyses of the read-out circuit belonging to short DETF resonators in Design 1A and 1C.62

Figure 2.25: Transient analyses results of the read-out circuit belonging to long DETF resonator utilized in Design #2. The frequency oscillating in the loop is at 47 kHz.63

Figure 2.26: Transient analyses results of the read-out circuit belonging to long DETF resonator utilized in Design #1. The frequency oscillating in the loop is at 86 kHz.63

Figure 2.27: Transient analyses results of the read-out circuit belonging to long DETF resonator utilized in Design #1. The frequency oscillating in the loop is at 186 kHz.64

Figure 2.28: Transient analyses results of the read-out circuit belonging to short DETF resonator utilized in Design #1. The frequency oscillating in the loop is at 343 kHz.64

Figure 2.29: Schematic of the sensing element of the capacitive MEMS accelerometer used in this thesis study. The components of the sensing element are labeled on the figure for illustrative purposes.66

Figure 2.30: Layout of the sensing element of MEMS accelerometer with the zoomed-view of the folded-beam spring structures and the proof mass branches.....68

Figure 2.31: Modal simulation results obtained via CoventorWare for the sensing elements accelerometers.....71

Figure 2.32: Schematic of the analog force-feedback read out circuit implemented to the MEMS accelerometer [51].....72

Figure 3.1: Process flow of the sensor wafer fabrication in aMEMS1 process over the cross-sectional views of the wafers.79

Figure 3.2: (a-d) Process flow of the cap wafer fabrication in aMEMS1 process over the cross-sectional views of the wafers. **e)** Cross-sectional view of the sensor die after anodic bonding of the sensor and cap wafers.....81

Figure 3.3: 3D model of the fabricated sensor chip used in this study.81

Figure 3.4: a) SEM images of the fabricated long and short DETF resonators in Design 1A. SEM images of the on-chip integrated DETF resonators (on the right) and a part of the capacitive accelerometer to be temperature-compensated (on the left). **b)** SEM images of the fabricated DETF resonators belonging to Design 1C. SEM images of the on-chip integrated DETF resonators (on the left) and a part of the capacitive accelerometer to be temperature-compensated (on the right). **c)** SEM images of the fabricated long and short DETF resonators in Design 2A. **d)** SEM images of the fabricated DETF resonators belonging to Design 2B. **e)** SEM images of the fabricated MEMS accelerometer together with the zoomed-view showing $\sim 1 \mu\text{m}$ undercut is observed on the width of the folded-beam springs. **f)** SEM images of the fabricated DETF resonator together with the zoomed-view showing $\sim 1 \mu\text{m}$ undercut is observed on the width of the tine, and $\sim 0.5 \mu\text{m}$ undercut for the capacitive gaps is observed.83

Figure 4.1: Photo of the characterization test setup prepared for the functionality tests of fabricated MEMS DETF resonators.....	86
Figure 4.2: Characterization test results of the fabricated DETF resonators belonging to a) Long DETF resonator present in Design 1A, b) Short DETF resonator present in Design 1A, c) Long DETF resonator present in Design 1C, d) Short DETF resonator present in Design 1C, e) Long DETF resonator present in Design 2A, f) Short DETF resonator present in Design 2A, g) Long DETF resonator present in Design 2B and h) Short DETF resonator present in Design 2B.....	88
Figure 4.3: CV test results of the MEMS accelerometer in Design 1C.....	90
Figure 4.4: Overview of the sensor package employed throughout the system-level tests.	92
Figure 4.5: Overview of the readout package [48] for the system-level tests of MEMS accelerometers. Note that there are only the readout components in this package while the sensor chip is placed inside the sensor package presented in Figure 4.4.	94
Figure 4.6: Layout of the test PCB prepared via Eagle software. Note that the test PCB is designed as one-sided PCB, and the connections showed in this figure processed the bottom side of fabricated test PCB.	95
Figure 4.7: Overview of the fabricated prototype test PCB.....	96
Figure 4.8: Photo of the test setup used in the system-level temperature tests.....	97
Figure 4.9: a) System-level test result of the long DETF resonator in Design 1A. The resulting TCf of the long DETF resonator is calculated as 730 ppm/K. b) System-level test result of the short DETF resonator in Design 1A. The resulting TCf of the short DETF resonator is calculated as 248 ppm/K.	100
Figure 4.10: Temperature look-up graph a) for the long DETF resonator, and b) for the short DETF resonator in Design 1A.	101
Figure 4.11: a) System-level test result of the long DETF resonator in Design 1C. The resulting TCf of the long DETF resonator is calculated as 497 ppm/K. b) System-level test result of the short DETF resonator in Design 1C. The resulting TCf of the short DETF resonator is calculated as 102 ppm/K.	103

Figure 4.12: Temperature look-up graph **a)** for the long DETF resonator, and **b)** for the short DETF resonator in Design 1C.....104

Figure 4.13: **a)** System-level test result of the long DETF resonator in Design 2A. The resulting TCf of the long DETF resonator is calculated as 636 ppm/K. **b)** System-level test result of the short DETF resonator in Design 2A. The resulting TCf of the short DETF resonator is calculated as 215 ppm/K.....105

Figure 4.14: Temperature look-up graph **a)** for the long DETF resonator, and **b)** for the short DETF resonator in Design 2A.....106

Figure 4.15: **a)** System-level test result of the long DETF resonator in Design 2B. The resulting TCf of the long DETF resonator is calculated as -18 ppm/K. **b)** System-level test result of the short DETF resonator in Design 2B. The resulting TCf of the long DETF resonator is calculated as -17 ppm/K.108

Figure 4.16: Temperature look-up graph **a)** for the long DETF resonator, and **b)** for the short DETF resonator in Design 2B.....109

Figure 4.17: Allan-deviation plots **a)** for the frequency output of long DETF resonator in Design 2A, **b)** for the frequency output of short DETF resonator in Design 2A. Minimum detectable temperature values are determined by using the bias instability values which are 0.0123 °C for 4 seconds integration time and 0.0011 °C for 4 seconds integration time for the long and short DETF resonators respectively.112

Figure 4.18: **a)** System-level temperature test result of the MEMS accelerometer in Design 1A. The result shows the temperature dependence of 133 $\mu\text{g}/^\circ\text{C}$ for this accelerometer. **b)** System-level temperature test result of the MEMS accelerometer in Design 1C. The results show that the temperature dependence of this accelerometer is 1,164 $\mu\text{g}/^\circ\text{C}$. **c)** System-level temperature test result of the MEMS accelerometer in Design 1A. The result shows the temperature dependence of 417 $\mu\text{g}/^\circ\text{C}$ for this accelerometer. **d)** System-level temperature test result of the MEMS accelerometer in Design 1A. The results show that the temperature dependence of this accelerometer is - 72 $\mu\text{g}/^\circ\text{C}$115

Figure 4.19: Allan deviation plots for the accelerometers used in this thesis study.116

Figure 4.20: **a)** Temperature compensation plots of the MEMS accelerometer in Design 1A presenting both compensated and uncompensated accelerometer outputs. The temperature dependence is reduced to $-0.7 \mu\text{g}/^\circ\text{C}$ from $133 \mu\text{g}/^\circ\text{C}$, which indicates 190 times improvement for this accelerometer. **b)** Temperature compensation plots of the MEMS accelerometer in Design 1A presenting both compensated and uncompensated accelerometer outputs. The temperature dependence is reduced to $1.4 \mu\text{g}/^\circ\text{C}$ from $1,164 \mu\text{g}/^\circ\text{C}$, which indicates 831 times improvement for this accelerometer. **c)** Temperature compensation plots of the MEMS accelerometer in Design 1A presenting both compensated and uncompensated accelerometer outputs. The temperature dependence is reduced to $3.1 \mu\text{g}/^\circ\text{C}$ from $417\mu\text{g}/^\circ\text{C}$, which indicates 135 times improvement for this accelerometer. **d)** Temperature compensation plots of the MEMS accelerometer in Design 1A presenting both compensated and uncompensated accelerometer outputs. The temperature dependence is reduced to $2.8 \mu\text{g}/^\circ\text{C}$ from $-72 \mu\text{g}/^\circ\text{C}$, which indicates 190 times improvement for this accelerometer. 120

Figure 4.21: Allan deviation plot of the compensated and uncompensated noise data belonging to an accelerometer with the same sensing element structure of those presented in this thesis study [60]. 122

LIST OF TABLES

TABLES

Table 2.1: Geometric properties of the DETF resonators offered in this thesis study. ...	38
Table 2.2: Analytical model results of the DETF resonators in the designs offered in this thesis study while the parameters presented in Table 2.1 are used in the governing equations.....	39
Table 2.3: Modal simulation results of the resonator structures in Design 1A. First 11 modes of the resonator system presented as Design 1A can be examined in the table....	42
Table 2.4: Modal simulation results of the resonator structures in Design 1C. The desired operation modes can be seen in the first 10 modes of the resonator system as labeled below.....	44
Table 2.5: Modal analysis results of the resonators in Design 2A showing the first 10 modes of the resonator system. Additionally, the modes of the short DETF resonator are presented below the first 10 modes.	46
Table 2.6: Modal simulation results of the resonators in Design 2B showing the first 10 modes of the resonator system. The operation modes of the short DETF resonator are added below the first 10 modes.....	48
Table 2.7: Comparison of the mathematical model results and thermo-mechanical simulation results showing the TCf of the counterpart designs *Average TCf calculated for the in-phase and out-phase operation mode.....	56
Table 2.8: Geometric properties of the MEMS accelerometer used in this study.....	69
Table 2.9: Sensor characteristics of the capacitive MEMS accelerometer used in this study.	70
Table 2.10: Modal simulation results of the sensing element of the accelerometer in all designs. The desired operation modes can be seen in the first 5 modes of the resonator system as labeled below.	71

Table 4.1: Results of the characterization tests of MEMS DETF resonators.89

Table 4.2: Summary of the CV test results of the MEMS accelerometers used in this thesis study.91

Table 4.3: Summary of all results including mathematical model results, thermo-mechanical simulation results and measurement results of MEMS DETF results utilized in this thesis study. 110

Table 4.4: Summary of the sensor characteristics of the MEMS accelerometers used in this thesis study.117

Table 4.5: Results of the temperature compensation of the MEMS accelerometers utilized in this study. 121

CHAPTER 1

INTRODUCTION

The consumer electronics have become an essential part of life in the last decade due to their “smart” properties, ease of use, and ability to provide instant services. The rapid increase of consumer products is the outcome of researches conducted for years on the miniaturization of electronic components and improvements in integrated-circuit (IC) fabrication techniques. The advancements in integrated-circuit fabrication techniques have made it possible to manufacture electronic components in small sizes with low cost, which directly reflects on the final product: smart phones in the hands of millions, tablets in front of many children etc. By leaving the discussion of the harmful effects of the daily-use electronic components on the social behavior of human beings to the experts, the researchers have kept concentrating on the developments of their products. The parts giving the title of “smart” to some daily-use electronic products are the physical sensors able to sense the targeted physical quantity, and use this information to provide services to the users. The sensors of these final products are mostly from the Micro-Electro-Mechanical-Systems (MEMS) family, which utilizes the micro-sized mechanical devices combined with micro-electronics. The improvements in IC fabrication techniques directly reflects on surface and bulk micro-machining techniques used in the fabrication of MEMS sensors, hence the use of MEMS devices spreads to many different application areas inevitably [1-3]. Accordingly, the MEMS market is in increasing trend, and its revenue is expected to exceed \$20B by 2020 [4].

MEMS resonators are the type of physical sensors which can be utilized in combination with many other MEMS sensors. The wide-variety of use of MEMS resonators has made these devices an attraction point to the researchers to focus on. Similarly, MEMS accelerometers are in great demand since they are employed in inertial navigation systems. The studies have been focused on the improvements of such MEMS sensors, i.e., MEMS accelerometers, MEMS resonators and so on. in order to fulfill the requirements of the high market demands [4]. One of the most well-known drawbacks of MEMS sensors is the temperature dependent performance degradations. While the researchers have been working on compensating the performance deteriorations related to temperature changes, sensing the temperature changes affecting the MEMS sensor precisely have appeared as another issue, which brings up the main goals in this thesis study, i.e., the temperature compensation of capacitive MEMS accelerometers by using sensitive resonant-based MEMS temperature sensors co-fabricated with MEMS accelerometers.

In Section 1.1, the overview of MEMS resonators studied in the literature will be presented. Immediately after, the temperature compensation techniques utilized in MEMS physical sensors are examined with the examples from literature together with some high performance temperature sensors published in the literature.

1.1 Overview of MEMS Resonators

MEMS resonators have been employed in a wide range of applications due to their relatively simple principles of operation [5]. The utilities of MEMS resonators both in industrial and research-focused applications are resulted with different types of MEMS resonators such as ring resonators, contour/lame mode plate resonators, bulk acoustic wave resonators in different applications including the optical, photonic, and acoustic systems [6-10]. Apart from these MEMS resonators, double-ended-tuning-fork (DETF) resonators are quite popular among MEMS physical sensors due to the strain-sensitive tines. Many studies have taken advantage of the strain effects on the DETF tines which cause the frequency shift of the lateral vibration mode of the DETF tines which was first reported in [11]. By expressing the targeted measurand in terms of frequency shift of

DETF resonators, the DETF resonators can be utilized as physical sensors. By using this property of the DETF resonators, MEMS accelerometers with differential sensing [12, 13], MEMS strain sensors [14], MEMS force sensors [15], and MEMS pressure sensors [16] have been studied.

Another common use of MEMS resonant-based sensors is the timing and frequency reference applications instead of quartz crystals [17]. The removal of the inherent temperature dependence of silicon-based MEMS resonators is a hot topic for the reference application purposes. While many studies have focused on this issue [18-21], temperature dependency of the MEMS resonators brings up the temperature sensor adoption of MEMS resonators. The use of DETF resonators as temperature sensors can be seen in [22, 23]. In this study [22], two DETF resonators are employed to create a beat frequency by using different modes of these two DETF resonators operating in closed-loop. The temperature dependency of beat frequency is boosted due to the close resonance frequencies of DETF resonators. This study has reported -570 ppm/K as the highest TCf sensitivity and 0.008 °C resolution for the offered temperature sensor design. The drawback of this study is the complicated electronic circuit which may also show temperature dependency. In [23], the resonant DETF temperature sensor with the TCf of -31 ppm/K, and resolution of 10 mK has been reported. Although the integration of the DETF resonator with a pressure sensor for the temperature compensation purpose is novel, the reported sensitivity is usual for a DETF resonator.

1.2 Overview of Temperature Compensation Techniques in MEMS Sensors

The remarkable development in the MEMS industry pushes the researchers to focus on more reliable and robust sensor designs which can withstand different environmental effects. The most significant environmental factor that affects the performance of a MEMS sensor, and hence its reliability, is the ambient temperature. Since the MEMS devices are small in dimensions, small short-term temperature changes during the operation of the device is an important issue to work on in addition to the major changes in temperature, i.e., the temperature difference between the day and night. Each temperature change affects the sensor structure directly and quickly due to the micro-

sized sensing elements, indicating very low thermal time constants of MEMS devices. In order to eliminate the performance degradation of a MEMS device due to temperature fluctuations, keeping the sensor at a fixed temperature have been used as a solution in some studies. Micro-ovens utilizing dedicated heaters are employed for this purpose in [24-27]. With this method, temperature changes have not been an issue affecting the performance of the sensor since the micro-ovens are aimed to keep the ambient temperature of the sensor at a fixed level. The major drawback of creating a fixed temperature environment for the MEMS sensor is the power consumption.

Another solution for the temperature compensation of MEMS sensors is the utilization of electronic circuits that find a linear relation between the temperature and the current or voltage present in the circuit to compensate the temperature dependent drifts [28, 29]. This method lacks in compensation of the instant temperature fluctuations since the thermal lag exists between the MEMS sensor and the compensation circuit.

The temperature of the MEMS sensor should be monitored with high precision, so that temperature sensitivity of the MEMS sensor can be controlled or properly compensated. This option requires a highly-sensitive temperature sensor to be placed to the MEMS device as close as possible, so that the precise and instant temperature-sensing can be achieved. The standard commercial temperature sensors lack at this point, since they can't be mounted just aside the MEMS sensor. Even though the temperature sensor chip is placed as close as possible to the MEMS chip, the measured temperature will not be the exact temperature of the MEMS device, where some sort of thermal model is needed for further corrections as stated in [30, 31]. The same problem occurs when the high sensitivity temperature sensors fabricated with CMOS technology presented in [32] are preferred for the temperature compensation applications. The proposed CMOS temperature sensor [33] has the resolution of 100 μK which is the state-of-the-art reported performance level while indicating relatively high power consumption than its counterpart [34]. The integration of CMOS temperature chip with the MEMS sensors monolithically is not the exact solution to prevent thermal lag since there still exist extra layers between the MEMS sensor and CMOS temperature sensor. To avoid thermal lag,

the on-chip integration of the MEMS sensor to be temperature-compensated and the MEMS temperature sensor is essential.

Some examples of MEMS temperature sensors utilizing the resonant based detection reported in literature can be found in [18, 22, 23, 35]. However, current approaches use complicated test setup, and do not facilitate the integration with the other MEMS sensor to be temperature-compensated [18, 22, 35]. Only [23] proposed the integration of MEMS resonator used to compensate the temperature dependence of a pressure sensor has reported a very low sensitivity of temperature sensor such as -31 ppm/K, which may need a high precision frequency counter.

1.3 Objectives and Organization of Thesis Study

The main motivation of this study is to propose a solution for the temperature compensation issue of MEMS devices mentioned in the previous section. Therefore, the objectives of this thesis study are focused primarily on the design, analysis, fabrication and implementation of a high performance resonant-based MEMS temperature sensor, which can be employed in the temperature compensation of other MEMS sensors by on-chip integration as well as in applications where sensitive temperature detection is essential. To be able to exemplify an application of the proposed MEMS temperature sensors, the temperature compensation of a capacitive MEMS accelerometer integrated with the MEMS temperature sensor offered in this study is selected as the other objective. The specific objectives are introduced in the list below:

- The detailed design procedures of resonance-based MEMS temperature sensors are to be presented with the analytical models giving the insights of the operation principles of the MEMS resonators as MEMS temperature sensors. The sensitivity of the MEMS temperature sensors will be maximized.
- The functionality of the MEMS temperature sensors is to be analyzed with the FEM simulations, i.e., modal simulations and thermo-mechanical simulations.
- A read-out circuit is to be designed for the MEMS DETF resonators to sustain the desired resonance in a closed-loop configuration, i.e., the real-time data acquisition from the MEMS resonators is to be enabled. The functionality of

the read-out circuit to be implemented for the MEMS resonators is to be verified by the electronic circuit simulations.

- A single-axis capacitive MEMS accelerometer is to be used to compensate its temperature dependence by using the proposed MEMS temperature sensor. Therefore, the mechanical design of the sensing element of the MEMS accelerometer and the closed-loop analog readout circuit of the MEMS accelerometer is to be introduced briefly.
- The MEMS accelerometer and MEMS temperature sensors will be integrated on the same chip to minimize the thermal lag between the MEMS temperature sensor and the MEMS accelerometer whose temperature dependence to be compensated. The fabrication of on-chip-integrated sensors is to be handled in the in-house clean room facilities.
- The characterization tests of MEMS accelerometer and temperature sensors where the sensor properties are detected, and the system-level temperature tests where the MEMS accelerometer and the DETF resonators are operated simultaneously are to be explained. Simultaneous operation of MEMS temperature sensor and MEMS accelerometer is essential for the temperature compensation process whose results are to be demonstrated separately. The measurement results are to be compared with the analytical model results and FEM simulation results.

The organization of the thesis is presented in the following paragraphs each of which summarizes the content of the related chapter.

Chapter 2 presents the operation principles of the MEMS resonators, accelerometers and proposed temperature sensors. The operation principles of MEMS temperature sensors are given together with the FEM simulation results whereas the operation principle of MEMS accelerometer is introduced briefly. The comparison of FEM simulation results and analytical model results is also presented. Read-out circuits utilized for the closed-loop operation of MEMS resonators are demonstrated and supported with the circuit simulations. The closed-loop analog read-out circuit implemented to the MEMS accelerometer is also mentioned briefly in this chapter.

In Chapter 3, the fabrication process of the MEMS resonators and accelerometers is presented with the details of the fabrication process flow. The fabrication results are also presented in this image by means of SEM images of the fabricated sensors.

Chapter 4 introduces the test procedures, preparation of the test setup, and measurement results of the fabricated sensors. The characterization tests of MEMS resonators and accelerometers and system-level tests are discussed in different sections to improve clarity. Overview of the system-level test results and temperature compensation results are presented in tables to show the achievements of the thesis.

Chapter 5 summarizes the achievements of this thesis study, and presents the suggested future works of the author about this research study.

CHAPTER 2

DESIGN AND MODELLING OF MEMS DETF RESONATORS AND ACCELEROMETERS

In this chapter, design and modeling of resonant MEMS temperature sensors and capacitive MEMS accelerometers used in this thesis study will be introduced one-by-one. Starting from the theory behind, design steps are examined separately and meticulously for temperature sensors and accelerometers. This chapter starts with Section 2.1 where the design of MEMS resonators used as temperature sensors is introduced in details. The theoretical background about MEMS resonators with brief explanations, mechanical design steps including the operation of MEMS resonators as temperature sensing elements and parameter optimizations, and finite element analyses of the proposed MEMS temperature sensor designs will also be examined in sub-sections of Section 2.1, successively. The read-out electronics of the thermometers are introduced in Section 2.2. Afterwards, design of capacitive MEMS accelerometer will be detailed in sub-sections of Section 2.3 where operation principles of capacitive MEMS accelerometer, mechanical design, and finite element modeling (FEM) simulations are described shortly. Then, Section 2.4 will present the analog read-out circuit of MEMS accelerometer used in this study. Section 2.5 introduces the temperature effects on the accelerometer performance with brief explanations and relevant references. At the end of this chapter, Section 2.6 will sum up the content presented in this chapter.

2.1 Design of Resonant MEMS Temperature Sensors

MEMS resonators have a common use in many different sensing applications as stated in Chapter 1 [1]. In this study, temperature sensing is procured by means of MEMS resonators. To explain the working principles of this resonant based temperature sensor, first, operation principles of MEMS resonators should be explained. Hence, in Section 2.1.1, the detailed analysis of working principles of MEMS resonators used in this study will be presented. After getting to know how the resonators work, secondly, we will examine the mechanical design of temperature sensor systems, which will be introduced in Section 2.1.2. Then, by giving the FEM analyses results in Section 2.1.3 and by describing the electronic read-out circuit of the resonators in Section 2.1.4, whole design cycle of resonant based MEMS temperature sensor would be presented.

2.1.1 Operation Principles of MEMS DETF Resonators Used in This Study

MEMS resonators used in this thesis study are in the form the double-ended-tuning-fork (DETF) type resonators. Resonators are comprised of two tines in DETF structures, which are able to move mechanically under the effect of electrostatic force. The electrostatic force applied to the tines of DETF structures is provided via two electrode sets. These two electrode sets, namely drive electrode and sense electrode, are placed around the tines of DETF structures so that the signals passing through the electrodes cause the tines to vibrate in its desired operation mode with respect to the capacitive actuation and capacitive sensing principles. In this section, the mechanical motion of the tines of the DETF resonators is examined while the capacitive actuation and sensing mechanisms will be described in the following sections, Section 2.1.2 and Section 2.1.3, respectively.

Before proceeding to the operation principles of the MEMS resonators, the resonator structures utilized in this study should be explained. The resonators used in this work are the DETF type resonators. Two different tine types are used in the DETF structures. Figure 2.1 illustrates two different DETF structures designed for this study.

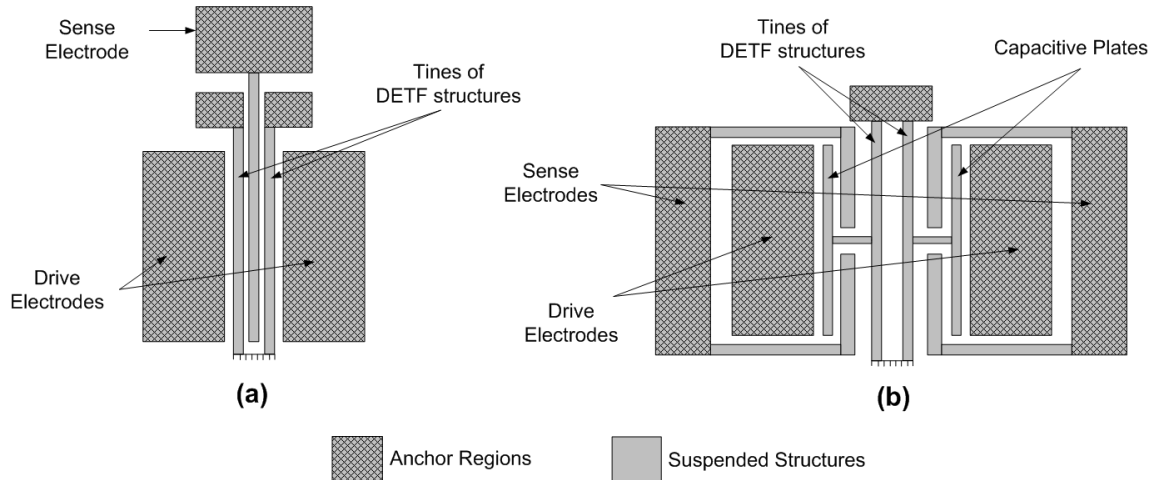


Figure 2.1: *a) Schematic of the DETF resonator structures denoted by Design #1, b) Schematic of the DETF resonator structures denoted by Design #2.*

In Design #1, the tines of the DETF structure comprised of two single suspended column placed side-by-side while the drive electrodes are placed to two sides of the tines, and sense electrode lies between the tines of the resonators. The capacitance change due to the motion of the tines in resonance will be non-linear since both ends of the tines are assumed to be fixed. To eliminate this non-linearity, another resonator design is used, namely Design #2. In Design #2, the tines of the resonators have the additional capacitive plates connected to the tines at the middle region in order to provide stable displacements while the tines are resonating. The drawback of the Design #2 is the area covered by a DETF structure. Design #1 covers almost half of the area which is covered by DETF structure in Design #2. The covered area by the DETF resonators is quite important since the targeted resonator structures are aimed to utilize in temperature compensation of other MEMS devices by on-chip integration. Hence, it can be said that the smaller the covered area, the easier the integration of MEMS resonator.

The movable parts of the resonator structures, i.e. tines of DETF structures in our case, can be modeled as second order mass-spring-damper system. Figure 2.2 shows the schematic of the model of the resonator tines.

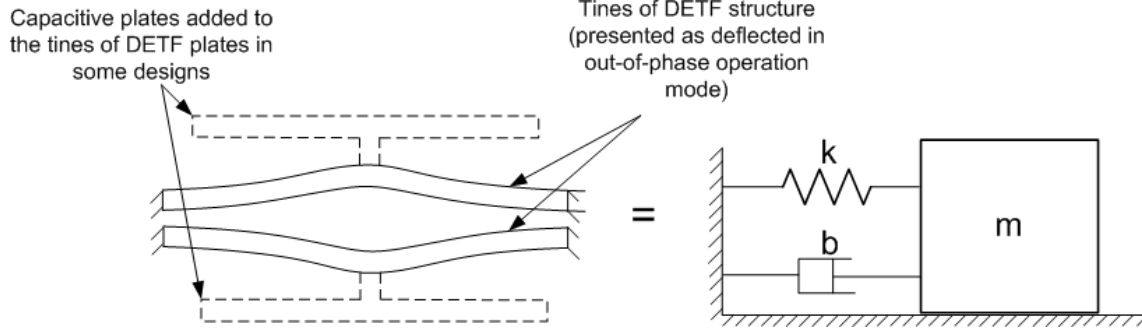


Figure 2.2: Schematic of the tines of DETF structure while deflected in out-of-phase operation mode and the associated second order mass-spring-damper system are presented.

Equation of motion of the tines of DETF structures modeled as shown in Figure 2.2 can be written as:

$$m\ddot{x} + b\dot{x} + k_m x = F \quad (2.1)$$

Where m denotes the mass resonating, x represents the displacement of the mass, b shows the damping coefficient, k_m stands for the mechanical spring constant calculated for the relevant motion direction, and F indicates the applied force to the mass. By taking the Laplace transform of the equation of motion (2.1), the transfer function between the displacement and the force can be found as follows:

$$\frac{X(s)}{F(s)} = \frac{1}{ms^2 + bs + k_m} \quad (2.2)$$

In order to define the motion of the resonating structures, the undamped and damped natural frequencies and the damping ratio of the system, denoted by ω_n , ω_d and ξ , respectively, should be introduced.

$$\omega_n = \sqrt{\frac{k_m}{m}} \quad (2.3)$$

$$\xi = \frac{b}{2\sqrt{k_m m}} \quad (2.4)$$

$$\omega_d = \omega_n \sqrt{1 - \xi^2} \quad (2.5)$$

Among the terms presented above, damping ratio has an important role in describing the motion of the resonating structures. If the damping ratio is greater than 1 or equals to 1, the system becomes over-damped and critically damped, respectively, and no oscillation would be allowed in the system, which is not desired for our resonator logic. The damping ratio must be less than 1 for a resonator to sustain the resonance. Actually, the damping ratio should be as small as possible for the ease of resonance, which means less dissipated energy while the mass is in resonance. Since the damping is mostly dominated by the air molecules for the structures in micro-scale, a vacuum environment suits better for the resonators. That is why a fabrication process including the wafer-level-vacuum-packaging, which will be introduced in Chapter 3, is preferred in this thesis study. The term quality factor, Q , indicates how under-damped the system is. Although the quality factor refers to the dimensionless term obtained by dividing the resonance frequency by half-power bandwidth, where the resonance amplitude degrades 3 dB from the peak amplitude, as shown in Figure 2.3, it can also be calculated as follows for a mechanical system:

$$Q = \frac{\sqrt{k_m m}}{b} \quad (2.6)$$

where the damping ratio is assumed to be small ($\xi < 0.1$).

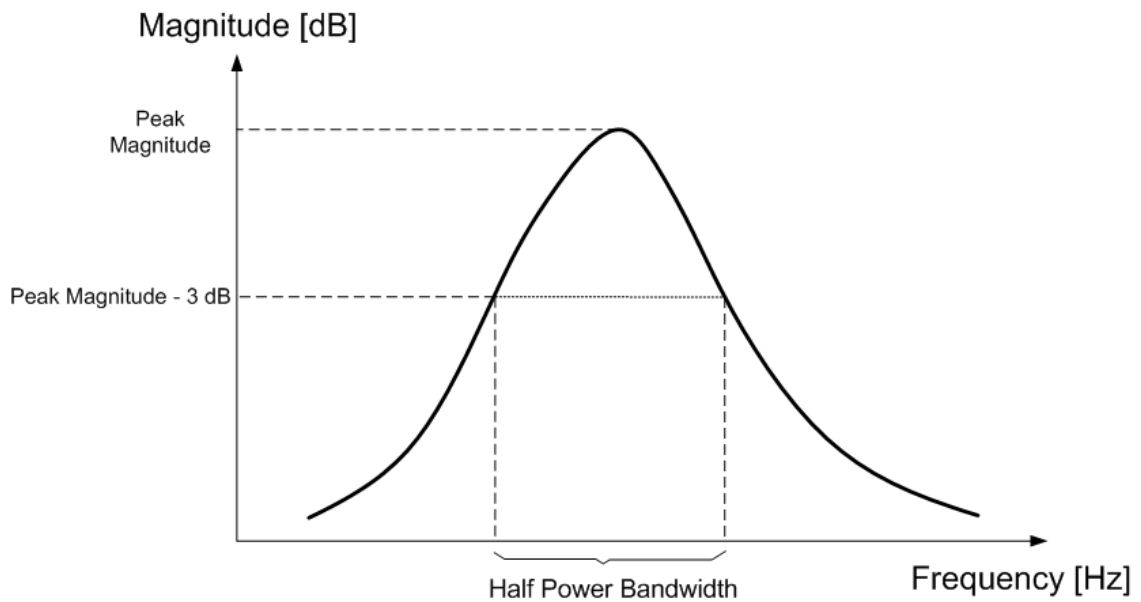


Figure 2.3: Half-power bandwidth illustration on a typical frequency-response plot.

The effect of damping on natural frequency of the system should be considered in the systems where the damping has importance. However, the damped and undamped natural frequencies have almost same value in this case since the damping ratio is so small as in most practical cases. Hence, the undamped natural frequency formula will be utilized in further calculations. In the next section, the trigger mechanism of the resonators for the resonance will be described.

2.1.1.1 Capacitive Actuation

Trigger mechanism for the desired motion of the resonator structures is provided by capacitive actuation. This actuation method benefits from the electrostatic forces applied to the resonator structure by means of the drive electrodes placed around the resonating mass. Due to micro-sized resonator structures, the electrostatic forces can induce necessary forces to move the tines of the resonator.

Electrostatic forces occur where electrostatic energy has a gradient, and can be stated as follows:

$$F_e = \nabla E \quad (2.7)$$

Where F_e is the electrostatic force and E is the electrostatic energy. The electrostatic energy is simply equals to:

$$E = \frac{1}{2} CV^2 \quad (2.8)$$

Where C denotes the capacitance formed between the drive electrode and the tines of the resonator, and V is the applied electrical potential between the drive electrodes and the tines of the resonator in our case. Figure 2.4 illustrates the capacitance formed between the proof mass of the resonator and the drive electrodes.

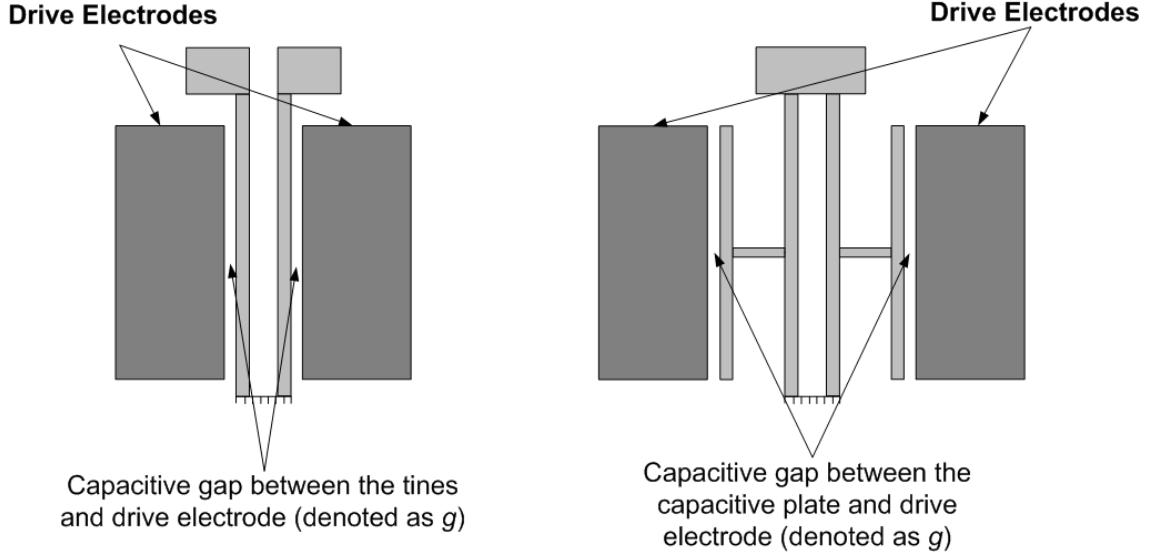


Figure 2.4: The capacitance formed between the proof mass of the resonators and the fixed drive electrodes can be seen above. DETF resonator structure used in Design #1 can be seen on the left while the DETF structure of Design #2 is presented on the right.

The capacitance between the proof mass of the resonators and the drive electrode can be found as follows:

$$C = \frac{\varepsilon A_c}{g} \quad (2.9)$$

Where ε represents the permittivity of the medium in the capacitive gap, A_c is the capacitive area where the capacitance formed in between the proof mass of the resonator and the drive electrodes, and g is the capacitive gap between the proof mass of the resonator and the drive electrodes. The desired operation mode of the tines of the DETF structures is an in-plane motion of the tines along only one axis, called x-axis, from now on as shown in Figure 2.2. Then, the electrostatic force can be expressed by using (2.8):

$$F_e = \frac{1}{2} \frac{\partial C}{\partial x} V^2 \quad (2.10)$$

In order to further express the electrostatic force formula explicitly, partial derivative of the capacitance between the drive electrodes and the proof mass can be extracted. Hence, the capacitance change with respect to the deflection of tines can be extracted,

and the generated electrostatic force by means of drive electrodes on the tines can be expressed as follows:

$$F_{e,d} = \frac{1}{2} \frac{\partial}{\partial x} \left[\frac{\varepsilon A_c}{(g-x)} \right] V^2 \quad (2.11)$$

$$F_{e,d} = -\frac{1}{2} \frac{\varepsilon L_0 h}{(g-x)^2} V^2 \quad (2.12)$$

Where L_0 is the overlap area between the capacitive plate of the tines of DETF structure and the drive electrode, and h is the structural thickness of the whole resonator system. It should be noted at this point that the capacitance change with respect to the motion of the tines in resonance, i.e., displacement of the tines, should be different for the resonators in Design #1 and Design #2. The non-linear deflection of the tine of DETF resonator in Design #1 is expected to lead to a non-linear capacitance change for the resonators in this design. This non-linear effect will be discussed in this section hereinafter.

Now, by assuming that both AC and DC components are supplied as the potential to the proof mass and the drive electrode, equation (2.12) yields:

$$F_{e,d} = -\frac{1}{2} \frac{\varepsilon L_0 h}{(g-x)^2} (V_{DC} + V_{AC} \sin(\omega t))^2 \quad (2.13)$$

By extracting the square term and simplifying the equation by using double angle formula:

$$F_{e,d} = -\frac{1}{2} \frac{\varepsilon L_0 h}{(g-x)^2} \left[\left(V_{DC}^2 + \frac{V_{AC}^2}{2} \right) + 2V_{DC}V_{AC} \sin(\omega t) - \frac{V_{AC}^2}{2} \cos(2\omega t) \right] \quad (2.14)$$

It should be noted that by adding the AC term into the potential causes two frequency-related terms in the electrostatic force formula. By using the term containing the ωt , the tines of the resonators can be excited by setting the frequency of AC signal to the frequency of the desired operation mode. In this case, the $2\omega t$ term would be trying to excite the mechanical structure at the double frequency of the desired operation mode. To suppress this effect, the applied DC voltage should be much higher in amplitude than

the amplitude of the AC signal. If the voltages are selected in that way, $2\omega t$ term can be neglected, and (2.14) simplifies to the following:

$$F_{e,d} = -\frac{1}{2} \frac{\varepsilon L_0 h}{(g-x)^2} [V_{DC}^2 + 2V_{DC}V_{AC} \sin(\omega t)] \quad (2.15)$$

In equation (2.15) above, the applied electrostatic force on the tine of the resonator by drive electrode is presented. However, this does not represent the net force on the tine of the resonator since there is another electrode, called sense electrode, placed on the other side of the tine. The capacitance between the sense electrode and the proof mass cause balancing force acting on the opposite direction of the force created by drive electrode. The only component of the force created by the sense electrode is coming from the DC voltage applied to the proof mass of the resonator, and can be expressed as follows:

$$F_{e,s} = \frac{1}{2} \frac{\varepsilon L_0 h}{(g+x)^2} (V_{DC}^2) \quad (2.16)$$

The net force on the tine of the DETF structure can be expressed as in the below formula by assuming the displacement is much smaller than the capacitive gap ($x \ll g$):

$$F_{e,net} \cong \frac{1}{2} \frac{\varepsilon L_0 h}{g^2} [2V_{DC}V_{AC} \sin(\omega t)] \quad (2.17)$$

The Laplace transform of the net force equation can be written as below:

$$F(s) \cong \frac{\partial C}{\partial x} V_{DC} V(s) \quad (2.17)$$

where $V(s)$ denotes the input drive signal.

In the resonator structure, there is equilibrium between the electrostatic force and the stiffness of the tines of DETF structure. However, these two forces change with the displacement in different orders which may break the equilibrium at some point, in other words, pull-in takes place. While utilizing the capacitive actuation, one should consider the pull-in conditions in design stage. To express pull-in phenomena in our case, first the force equilibrium should be written in between the electrostatic force created by the drive electrode and the mechanical spring force of the tines of the DETF structure:

$$F_{e,d} + F_m = 0 \quad (2.18)$$

$$-\frac{1}{2} \frac{\varepsilon L_0 h}{(g-x)^2} [V_{DC}^2 + 2V_{DC}V_{AC} \sin(\omega t)] - k_m x = 0 \quad (2.19)$$

At this point, the AC voltage terms can be neglected as it will be chosen much smaller compared to DC voltage applied. Hence (2.19) can be reduced to:

$$-\frac{1}{2} \frac{\varepsilon L_0 h}{g^2} V_{DC}^2 - k_m x = 0 \quad (2.20)$$

In (2.19), electrostatic force term can be expressed as a force term obtained from a virtual spring, and by taking the partial derivative of this term with respect to displacement yields to the spring constant of this force, namely, electrostatic spring constant, as stated in the following with the assumption of that the displacement is much smaller than the capacitive gap ($x \ll g$):

$$k_e = \frac{\varepsilon L_0 h}{g^3} V_{DC}^2 \quad (2.21)$$

In Design #1, non-linear terms are supposed to be added to equation (2.21), due to the non-linear deflection of the tine as mentioned previously. If the electrostatic spring constant is expressed with the non-linear terms:

$$k_e = k_{e0}(1 + k_{e1}x + k_{e2}x^2 + \dots) \quad (2.22)$$

The non-linear electrostatic spring constant terms can be found by using Taylor Series expansion for the force equation (2.12).

$$F_{e,d} = -\frac{1}{2} \frac{\varepsilon L_0 h}{g^2} V^2 \left(1 + \frac{2}{g}x + \frac{3}{g^2}x^2 + \dots\right) \quad (2.23)$$

Using the same procedure while deriving the linear electrostatic spring constant (2.21) as stated above, the nonlinear terms can be found as follows:

$$k_{e0} = \frac{\varepsilon L_0 h}{g^3} V_{DC}^2 \quad (2.24)$$

$$k_{e1} = \frac{3}{2g} k_{e0} \quad (2.25)$$

$$k_{e2} = \frac{2}{g^2} k_{e0} \quad (2.26)$$

It should be noted that the k_{e1} terms should be neglected for the symmetric electrostatic actuation [36]. Note that for the small displacements, x , the non-linear effects will not be effective and the linear electrostatic spring constant (2.21) dominates as it will be the case in the operation of DETF resonators as described in Chapter 4.

Pull-in condition occurs where the electrostatic spring constant value overcomes the mechanical spring constant value. This condition may come true when the displacement of the movable part reaches to one-third of the nominal capacitive gap [37]. The voltage that cause pull-in is called, pull-in voltage and can be expressed as follows:

$$V_p = \sqrt{\frac{8k_m g^3}{27\epsilon L_0 h}} \quad (2.27)$$

Pull-in voltage limits the use of supplied DC voltage during the capacitive actuation operations, and it should be taken into considerations where the capacitive actuation is utilized.

2.1.1.2 Capacitive Detection

Capacitive sensing takes place when the tines of the DETF structures move under the effect of electrostatic forces mentioned in the previous section. The movement of the tines of DETF resonators causes the capacitance change in between the proof mass of the resonators and the sense electrode which is placed on the other side of the tine similar to drive electrodes. The capacitance change results with the change in the stored charge in the capacitances formed in between the proof mass and the sense electrode. The change of the stored charge is observed as a flowing current through the sense electrode. The current flowing through the sense electrode is then converted to a voltage by means of a trans-impedance-amplifier (TIA) and fed to the read-out circuit of the resonator. Figure 2.5 illustrates the positions of the sense electrodes and the capacitive sensing mechanism on the schematic of the resonator.

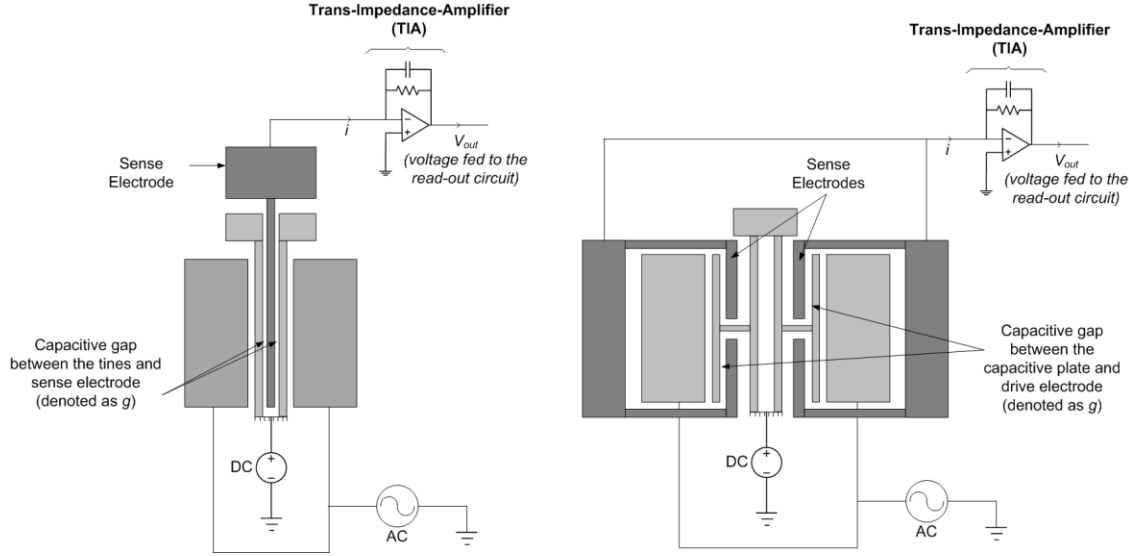


Figure 2.5: Schematic of the capacitive sensing mechanism.

The flowing current through the sense electrode can be formulated as follows:

$$Q = C V \quad (2.28)$$

$$i = \frac{\partial Q}{\partial t} = \frac{\partial C}{\partial t} V + C \frac{\partial V}{\partial t} \quad (2.29)$$

Where i stands for the current, Q is the accumulated charge between the capacitive plates of sense electrode and the tine of the resonator, and V is the applied voltage in between the capacitive plates. The time rate of the capacitance can be extracted by using chain rule, and the second term appeared on the right side in (2.29) can be neglected due to small amplitude of AC signal:

$$i = \frac{\partial C}{\partial x} \frac{\partial x}{\partial t} V \quad (2.30)$$

It should be noted that, as seen in (2.30), the current flowing through the sense electrode is directly proportional to the velocity of the tine of the resonator in addition to the applied DC voltage and the capacitance change. Since the displacement of the tine is a function of frequency as stated in the previous section, the time derivative of the displacement yields a frequency term appearing in the current formula. That means the current flowing through the sense electrode depends on the frequency of the resonator. Additionally, it can be inferred that there is supposed to be 90 phase difference coming

from this differentiation between the applied AC signal and current flowing through the sense electrode.

The Laplace transform of Equation (2.30) can be expressed to obtain the transfer function between the current and displacement as follows:

$$I(s) = \frac{\partial C}{\partial x} s X(s) V \quad (2.31)$$

where proof mass voltage V_{DC} can be used in equation (2.31) as V if drive signal is assumed to have negligible amplitude when compared to the proof mass voltage. To transform the current to the voltage, an op-amp is utilized as TIA as shown in Figure 2.5. This conversion enables controlling/manipulating the product of capacitive sensing in the read-out circuit of the resonators which will be explained in Section 2.2. The output voltage, V_{out} , and the current flowing through the sense electrode can be related as follows:

$$V_{out} = -i Z \quad (2.32)$$

Where Z denotes the impedance created by the resistor and capacitor on the TIA. More explicitly, the relation between the output voltage of TIA and the current can be written by using Laplace transform as the following:

$$V_{out}(s) = -I(s) \frac{R}{sRC + 1} \quad (2.33)$$

Now, it is possible to write down the overall transfer function of the resonator as follows:

$$H(s) = \frac{V_{out}(s)}{V(s)} = \frac{X(s) F(s) I(s) V_{out}(s)}{F(s) V(s) X(s) I(s)} = \frac{\left(\frac{\partial C}{\partial x} V_{DC}\right)^2 s}{ms^2 + bs + k} \frac{-R}{sRC + 1} \quad (2.34)$$

This transfer function can be utilized in the modeling of the resonators for the simulation purposes.

2.1.2. Mechanical Design of MEMS DETF Resonators Used in This Study

In mechanical design of MEMS resonators, the motivation of this thesis study presented in Chapter 1 was the primary concern. It was aimed to achieve a resonator design which operates as a sensitive temperature sensor. The offered temperature sensor design will be verified by the mathematical model and the finite element modeling (FEM) simulations. Additionally, to show the effectiveness of the offered temperature sensor designs, complementary resonator designs are created. The offered temperature sensor designs are introduced in the following section together with the operation principles.

2.1.2.1. Operation Principles of MEMS DETF Resonators as MEMS Temperature Sensor

MEMS resonators were quite handful to utilize in many different applications by simply monitoring the resonance frequency which is affected by the environmental inputs depending on the design of the resonator. One of the well-known utilization of the MEMS resonators arises from the axial load sensitivity of the tines of the DETF resonator [15], which leads to change in the axial stiffness of the resonator, and that affects the resonance frequency of the related modes. This phenomenon is the starting point of the temperature sensor design which will be presented here as Design A. The resonators utilized in Design A are designed such that the axial load on the tines of the resonator increased to boost the resonance frequency change of the resonators i.e. the strain amplifying beam structure is added to the resonator systems. To create an axial force on the tines of the resonators, materials with different thermal expansion coefficients of the substrate (glass, where $\alpha_g = 3.25 \times 10^{-6}$ 1/K) and the device layer (silicon, where $\alpha_{si} = 2.59 \times 10^{-6}$ 1/K), are required in the fabrication of the sensor structure [38]. In order to compare the effectiveness of the proposed temperature sensor in Design A, other resonator systems, called Design B and Design C, from now on, containing the same resonator structures is designed by changing only the connection style of the resonators to the anchors at one end. Instead of strain amplifying beam utilized in Design A, a small suspended beam is attached to one end of DETF resonators in Design B. The small suspended beam serves as the connector of resonators to the

anchor at the related end. In Design C, the strain-amplifying beam is removed, and instead, resonator tines are anchored at both ends. In all designs, there exist two DETF resonators named as long and short DETF resonators depending on the tine lengths of the resonators, to be able to obtain two temperature sensors with different sensitivities. Additionally, by changing the resonator tine structures as stated in the previous section by using Design #1 and Design #2 DETF resonators, different sensor designs are aimed. The different designs enable the verification of the mathematical model of the temperature sensors which will be presented in the next section. On the other hand, in order to avoid confusions resulting due to too many different designs, selected versions of Design A, B and C are integrated with Design #1 and Design #2. Figure 2.6 below illustrates the layouts of the resonator systems used in this study with electrical connections. Since Design A is the main temperature sensor design offered in this study, it will be implemented into both Design #1 and Design #2, and these versions are called Design 1A and Design 2A, respectively, from this point on. To compare the effectiveness of these designs, Design B is implemented into Design 2, and denoted as Design 2B while Design C is applied to Design #1 and called Design 1C, from this point on.

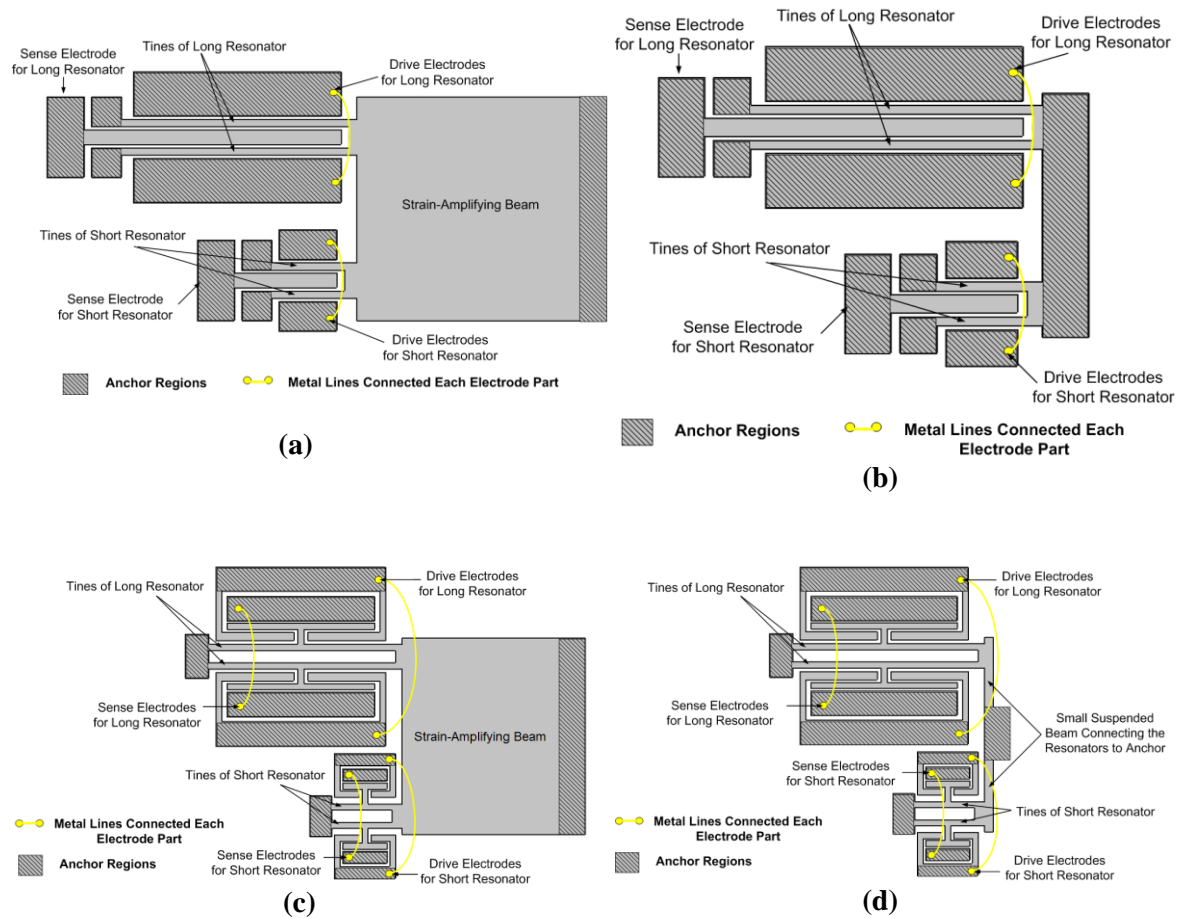


Figure 2.6: *a) Resonator layout of Design 1A, b) Resonator layout of Design 1C, c) Resonator layout of Design 2A, and d) Resonator layout of Design 2B.*

In the next sections, the mathematical model of the offered designs and supplementary designs are introduced.

2.1.2.1.1 Analytical Model of Design 1A and Design 2A

Thermal stress and strain relations obtained via strength of materials assumptions are employed while extracting the relation between the frequency change and the temperature. The cap and substrate interaction should be examined to include the effects of this interaction to the frequency shift calculations in Design 1A and Design 2A, before dealing with the sensor structure. Thermal strains of the cap and substrate are expressed along the axial direction of the tines of the resonators only in calculations as the main contribution to the frequency shifts come from the axial load on the tines of resonators. Since the cap and substrate have different thermal expansion coefficients, and they are bonded to each other, it is expected that the expansions/contractions due to

temperature changes will be restrained. Figure 2.7 illustrates the restrained thermal deflections of both cap and the substrate under certain temperature change.

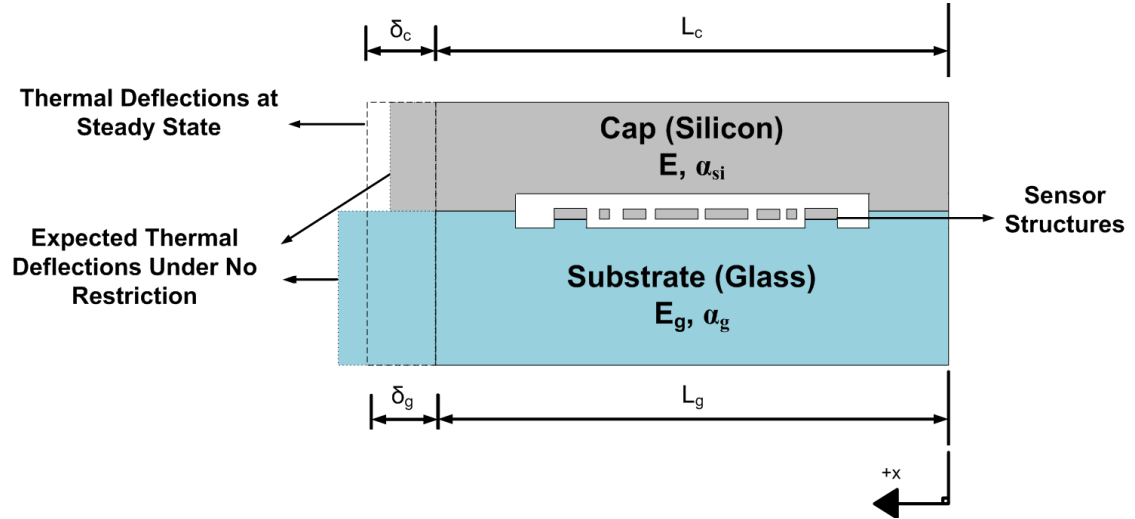


Figure 2.7: Simplified schematic of the cross-sectional view of a sensor die showing 1-D thermal deflections under temperature change.

As seen in Figure 2.7, different thermal expansion coefficients lead to a residual stress on each part when the system reaches to the steady state. This residual stress can be formulated by writing the thermal strain relations for both cap and the substrate. To begin with, the thermal strain relations for cap and the substrate yield to:

$$\delta_c = L_c \alpha_{si} \Delta T + \frac{P L_c}{E A_c} \quad (2.35)$$

$$\delta_g = L_g \alpha_g \Delta T - \frac{P L_g}{E_g A_g} \quad (2.36)$$

Where δ_c and δ_g show the thermal strain of the cap and the substrate, L_c and L_g designate the length of die along the axial direction of the tines of the resonators ($L_c=L_g=L$, in our case), α_{si} and α_g stand for the thermal expansion coefficients of the silicon, taken as 2.59×10^{-6} 1/K, (cap material) and thermal expansion coefficient of glass, taken as 3.25×10^{-6} 1/K, (substrate material), A_c and A_g designate the cross-sectional area of the cap and the substrate along the axial direction of the tines of the resonators, E and E_g show the elastic modulus of the silicon and the glass, respectively. P stands for the residual force on each member in the above formulae while ΔT shows the temperature change. These two thermal strain relations should be equal to each other since the cap

and the substrate stay on the same plane after bonding. When these relations are equated to obtain P:

$$L \alpha_{si} \Delta T + \frac{P L}{E A_c} = L \alpha_g \Delta T - \frac{P L}{E_g A_g} \quad (2.37)$$

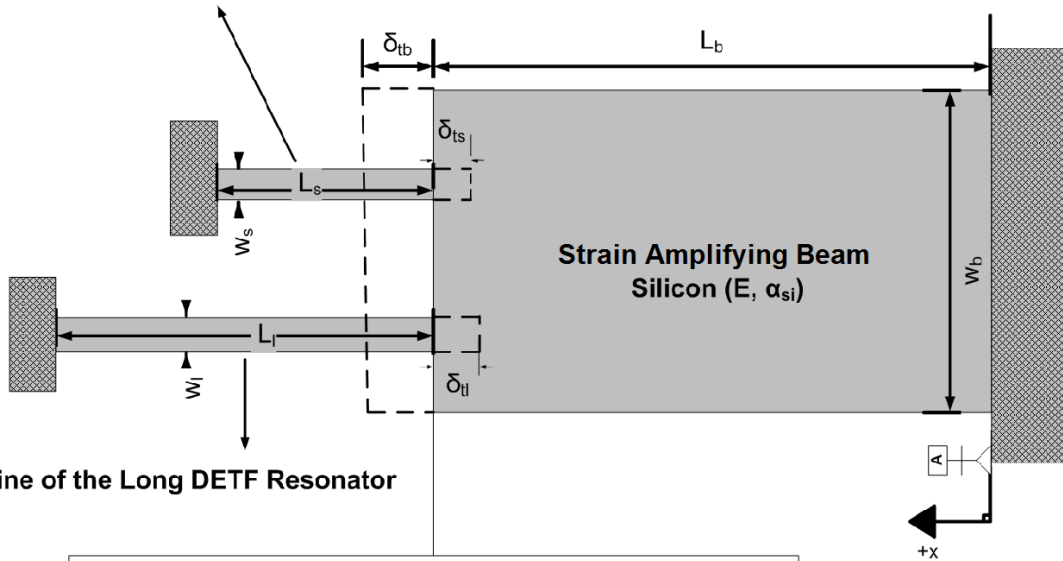
$$P = \frac{(\alpha_g - \alpha_{si}) \Delta T E E_g A_g A_c}{E A_c + E_g A_g} \quad (2.38)$$

The thermal strain on the substrate, ε_{Tg} , as a result of the residual force coming from the cap and the substrate interaction under temperature change can be obtained by using the Hooke's law as follows:

$$\varepsilon_{Tg} = \frac{(\alpha_g - \alpha_{si}) E A_c \Delta T}{E A_c + E_g A_g} \quad (2.39)$$

Now, the sensor structure effects can be examined in Design 1A and Design 2A. When the temperature changes, the tines of the DETF structures and strain amplifying beam have a tendency to push each other, and they will settle at some point which causes a deflection for all members in the resonator system. Figure 2.8 illustrates how the members in Design 1A and Design 2A are assumed to deflect under temperature change.

A Tine of the Short DETF Resonator



Section of interest where the thermal strains of each member with respect to datum A are written.

Figure 2.8: Simplified schematic of the resonator system offered in Design 1A. To avoid any confusion and for the sake of simplicity of the governing equations, only one tine of

the resonators are shown in this figure. Note that the hatched areas represent the anchor regions while others show the suspended sensor structures in top view.

The resonator system in Design 1A and Design 2A includes four components: a tine of the short DETF structure, a tine of the long DETF structure, a strain amplifying beam and the glass substrate where the dimensions and material properties of the related member are denoted as subscript “s”, “l”, “b” and “g”, respectively. To begin with, the strain equations of the joining regions of the tines of the resonators and the strain amplifying beam are derived for short resonator, long resonator, and the strain amplifying beam separately. Hence, strain of the joining surface of these 3 members can be written as:

$$\delta_s = (L_b + L_s)\alpha_g \Delta T + \varepsilon_{Tg}(L_b + L_s) - L_s\alpha_{si} \Delta T - \frac{F_s L_s}{E A_s} \quad (2.40)$$

$$\delta_l = (L_b + L_l)\alpha_g \Delta T + \varepsilon_{Tg}(L_b + L_l) - L_l\alpha_{si} \Delta T - \frac{F_l L_l}{E A_l} \quad (2.41)$$

$$\delta_b = L_b\alpha_{si} \Delta T + \frac{F_b L_b}{E A_b} \quad (2.42)$$

Where length and width of the tine of the long resonator, are denoted as L_l , and w_l , length and width of the tine of the short resonator are denoted as L_s , and w_s , the length and the width of the compressive beam are denoted as L_b and w_b , the axial forces created on the surface of short DETF tine and long DETF tine are referred as F_s and F_l , the total force exerted by the compressive beam is denoted by F_b , and the cross sectional area of the long DETF tine, short DETF tine and the compressive member are denoted by A_l , A_s and A_b , respectively. While obtaining these strain equations, the thermal deflection of the substrate including the thermal strain resulting from the cap and glass wafer interaction under temperature change effects, ε_{Tg} , the thermal deflection of the member and the steady state deflection point after temperature settles are taken into consideration respectively in each equation. As the meeting regions of these 3 members are on the same plane, the strain equations should be equal to each other if we assume that the joining surface stay in the same plane ($\delta_s = \delta_l = \delta_b$). In order to obtain the axial forces on the resonator tines in terms of each other, first $\delta_s = \delta_l$ condition is analyzed. By utilizing (2.40) and (2.41), and simplifying the equations:

$$(L_b + L_s)\alpha_g \Delta T + \varepsilon_{Tg}(L_b + L_s) - L_s\alpha_{si} \Delta T - \frac{F_s L_s}{E A_s} \quad (2.43)$$

$$= (L_b + L_l)\alpha_g \Delta T + \varepsilon_{Tg}(L_b + L_l) - L_l\alpha_{si} \Delta T - \frac{F_l L_l}{E A_l}$$

$$F_l = (\alpha_g \Delta T - \alpha_{si} \Delta T + \varepsilon_{Tg})w_l h E \left(\frac{L_l - L_s}{L_l} \right) + \left(\frac{L_s w_l}{w_s L_l} \right) F_s = C_1 + C_2 F_s \quad (2.44)$$

Where $C_1 = (\alpha_g \Delta T - \alpha_{si} \Delta T + \varepsilon_{Tg})w_l h E \left(\frac{L_l - L_s}{L_l} \right)$ and $C_2 = \frac{L_s w_l}{w_s L_l}$ when $A_s = w_s h$, $A_l = w_l h$ $A_b = w_b h$ are implemented in which h designates the structural thickness. To find F_s , the force equilibrium can be used along axial direction of the tines which is:

$$F_b = F_s + F_l = F_s + (C_1 + C_2 F_s) \quad (2.45)$$

Note that, since there are two tines for each resonator, the forces will be doubled while writing the force equilibrium in (2.45). Now, by using the second strain condition, ($\delta_s = \delta_b$) and using substitutions in (2.44), it is possible to get F_s in terms of temperature change:

$$(L_b + L_s)\alpha_g \Delta T + \varepsilon_{Tg}(L_b + L_s) - L_s\alpha_{si} \Delta T - \frac{F_s L_s}{E A_s} = L_b\alpha_{si} \Delta T + \frac{F_b L_b}{E A_b} \quad (2.46)$$

$$(L_b + L_s)\alpha_g \Delta T + \varepsilon_{Tg}(L_b + L_s) - L_s\alpha_{si} \Delta T - \frac{F_s L_s}{E A_s} \quad (2.47)$$

$$= L_b\alpha_{si} \Delta T + \frac{[F_s + (C_1 + C_2 F_s)]L_b}{E A_b}$$

$$F_s = \frac{(L_b + L_s)(\alpha_g \Delta T - \alpha_{si} \Delta T + \varepsilon_{Tg}) E A_s A_b - C_1 L_b A_s}{L_s A_b + L_b A_s + C_2 L_b A_s} \quad (2.48)$$

Or more explicitly F_s can be stated by using $A_s = w_s h$, $A_l = w_l h$, $A_b = w_b h$ where h is the structural thickness,

$$F_s = \frac{(L_b + L_s)(\alpha_g \Delta T - \alpha_{si} \Delta T + \varepsilon_{Tg}) E w_s w_b h - (\alpha_g \Delta T - \alpha_{si} \Delta T + \varepsilon_{Tg}) w_l h E \left(\frac{L_l - L_s}{L_l} \right) L_b w_s}{L_s w_b + L_b w_s + \frac{L_s w_l}{L_l} L_b} \quad (2.49)$$

Similarly, F_l , the axial force on the tines of the long resonator can be stated in terms of F_s by using (2.44).

$$F_l = (\alpha_g \Delta T - \alpha_{si} \Delta T + \varepsilon_{Tg}) w_l h E \left(\frac{L_l - L_s}{L_l} \right) + \left(\frac{(L_b + L_s)(\alpha_g \Delta T - \alpha_{si} \Delta T + \varepsilon_{Tg}) E A_s A_b - 2 C_1 L_b A_s}{L_s A_b + 2 L_b A_s + 2 C_2 L_b A_s} \right) \left(\frac{L_s w_l}{w_s L_l} \right) \quad (2.50)$$

After deriving the axial forces on each tine, F_l and F_s , in terms of temperature change, it is possible to relate the temperature change of a DETF tine with frequency change. First, the resonance frequency of the desired operation mode for a DETF can be found by using the equation (2.51) [39]:

$$f_n = \sqrt{\frac{k_{eff}}{m_{eff}}} = \sqrt{\frac{k_m - k_e}{\frac{13}{35} \rho h w L + \rho h (w_p L_p + w_c L_c)}} \quad (2.51)$$

Where f_n is the natural frequency of the DETF structure counterpart to the out-of-phase mode shape, m_{eff} and k_{eff} stands for the effective mass and effective stiffness values for this mode shape, L , L_p and L_c denote the length of the DETF tine, length of the capacitive plate and the length of the connector beam between the capacitive plate and the tine, w , w_p and w_c shows the width of the DETF tine, width of the capacitive plate and the width of the connector beam, respectively, and EI is the flexural stiffness of each tine. Note that while calculating the mass of the tines in Design 1A to be used in equation (2.51), w_p and w_c terms are taken as 0 since there is no capacitive plate or the connector beam added to the tines of DETF structures in Design 1A. Additionally, the electrostatic spring softening effect is added into effective spring constant calculation by subtracting the electrostatic spring constant, k_e , from the mechanical spring constant, k_m . The nonlinear mechanical spring constant effects on resonators can be added due to the nonlinear displacement of the tines as follows:

$$k_m = k_{m0}(1 + k_{m1}x + k_{m2}x^2 + \dots) \quad (2.52)$$

By assuming the triangle-shaped-deflection of the tines, k_{m0} , k_{m1} and k_{m2} can be found as the following [40]:

$$k_{m0} = \frac{192 E I}{L^3} \quad (2.53)$$

$$k_{m1} = 0 \quad (2.54)$$

$$k_{m2} = \frac{x^2}{2w^2} k_{m0} \quad (2.55)$$

Note that although the nonlinear electrostatic spring constant terms are only valid for the DETF resonators in Design #1, the nonlinear mechanical spring constant terms can be applied to all resonator designs. However, while calculating the effective spring constant, the linear coefficients, k_{m0} , k_{e0} , are utilized since the displacement of the tines are much smaller than the capacitive gaps and the resonators will be operated in the linear limits as it will be explained in the characterization test results of the resonators.

Now, the relation between the axial force and the resonance frequency can be found with the following equation [15]:

$$f = \sqrt{f_n^2 + \frac{2.4 F}{m_{eff} L}} = (A + B F)^{0.5} \quad (2.56)$$

in which F indicates the total axial force on the tines.

Since the sensitivities of the proposed temperature sensors depend on how frequency changes with the temperature, temperature coefficient of frequency (TCf) is the figure of merit for both designs. TCf caused by axial force of a resonator, TCf_F , can be found by using the following equation:

$$TCf_F = \frac{df}{dT} \frac{1}{f_n} = \left(\frac{df}{dF} \frac{dF}{dT} \right) \frac{1}{f} \quad (2.57)$$

When (2.57) is implemented for the short DETF structure, the TCf for the short DETF structure, denoted by $TCf_{F,s}$, can be found as:

$$TCf_{F,s} = (0.5B_s) \frac{1}{f_s f_{ns}} \frac{F_s}{\Delta T} \quad (2.58)$$

When the same procedure is followed for the long DETF resonator, TCf of the long resonator, $TCf_{F,l}$, can be obtained as:

$$TCf_{F,l} = (0.5B_l) \frac{1}{f_l f_{nl}} \left(\frac{F_l}{\Delta T} \right) \quad (2.59)$$

Where B_s and B_l are the coefficient B appeared in (2.56), calculated for the short and the long DETF resonator, respectively.

Apart from the TCf coming from the axial force, TCf_F , there exists a material dependent TCf component as a result of change in elastic modulus of the material, called $TCf_{F,E}$. This effect can be found as follows [41]:

$$TCf_E = TCE_{si}/2 \quad (2.60)$$

Note that in (2.60), temperature coefficient of elasticity for silicon, TCE_{si} , is employed due to the fact that the resonator structures are made of silicon. By including this material property effect, the overall TCf of the resonators used in Design 1A and Design 2A can be found as follows:

$$TCf = TCf_F + TCf_E \quad (2.61)$$

2.1.2.1.3 Analytical Model of Design 1C

Design 1C includes two DETF resonators directly anchored at both ends by removing the strain-amplifying beam present in Design 1A. The main factors affecting the TCf of the resonators in Design 1C is the axial force created on the tines of the DETF resonators. This axial force formula can be extracted by utilizing the thermal strain formula which was employed in the previous sections. Figure 2.9 illustrates the deflections of the tines of the resonators in Design 1C on the layout schematic of Design 1C.

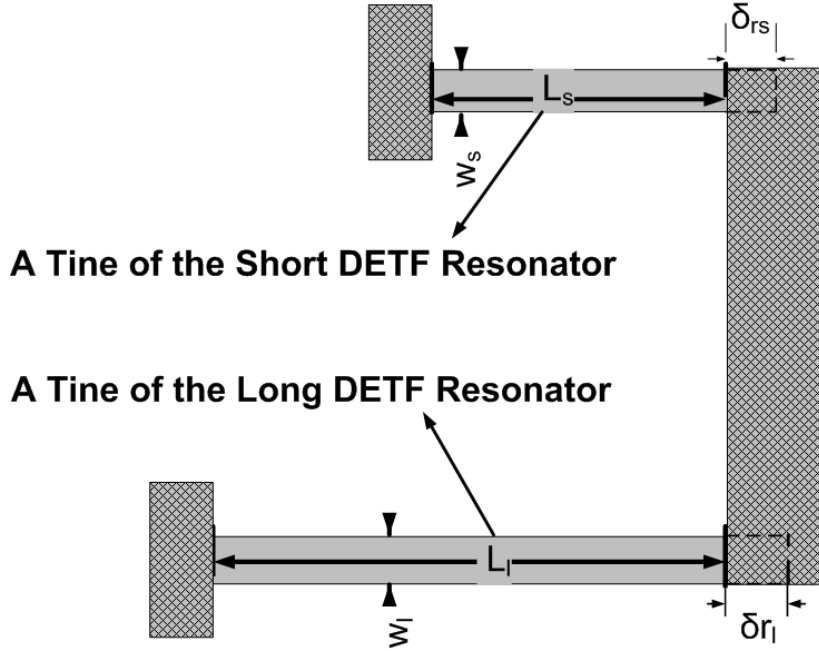


Figure 2.9: Simplified schematic of the resonator system offered in Design 1C. To avoid any confusion and for the sake of simplicity of the governing equations, only one tine of the resonators are shown in this figure. Note that the cross-hatched areas represent the anchor regions while others show the suspended sensor structures in top view.

The thermal strain of the tines of the resonators in Design 1C can be expressed as follows:

$$\delta_r = (\alpha_g - \alpha_{si}) L \Delta T + \varepsilon_{Tg} L \quad (2.62)$$

The axial force created on the tines of the resonators can be obtained by equating (2.62) to the deflection formula obtained via Hooke's law since thermal strain of the tines of the resonators is restrained by anchors at both ends as follows:

$$(\alpha_g - \alpha_{si}) L \Delta T + \varepsilon_{Tg} L = \frac{F_r L}{EA_b} \quad (2.63)$$

Where L denotes the length of the tine of the DETF resonator, F_r shows the axial load induced due to temperature change and A_b indicates the cross-sectional area of the tine. Note that, the cap-substrate interaction effect on thermal strains of substrate is added to the thermal deflection formula here in (2.63). The reason is that the TCf of the resonators in Design 1C is expected to be dominated by the axial force on the tines of the resonators.

The axial force created on the tines of resonators in Design 1C can be extracted from (2.63) as follows:

$$F_r = [(\alpha_g - \alpha_{si}) \Delta T + \varepsilon_{Tg}] EA_b \quad (2.64)$$

By using equation (2.57) and (2.64), the TCf_F caused by the axial force on the tines can be found as follows:

$$TCf_F = 0.5 B \frac{1}{f_n^2} \frac{[(\alpha_g - \alpha_{si}) \Delta T + \varepsilon_{Tg}] EA_b}{\Delta T} \quad (2.65)$$

When the changing material property effects on TCf, TCE , is added to TCf_F by using (2.61), the overall TCf can be found as follows:

$$TCf = 0.5 B \frac{1}{f_n^2} \frac{[(\alpha_g - \alpha_{si}) L \Delta T + \varepsilon_{Tg} L] EA_b}{\Delta T} + \frac{TCE_{si}}{2} \quad (2.66)$$

2.1.2.1.2 Analytical Model of Design 2B

The sensitivity of the resonators is expected to be dominated by the change in the material properties of the silicon under changing temperature in Design 2B due to the one-end free condition is tried on the resonator structure. This change is mainly due to the temperature coefficient of elastic modulus of silicon (TCE_{si}) which is mentioned in the end of the previous section. This effect can be formulated as stated in the previous section:

$$TCf_E = TCE_{si}/2 \quad (2.60)$$

Although the sensitivity of the resonators is dominated by TCE of silicon in Design #2B, a small amount of force is also created due to the stiffness of the small beam to which the resonators are attached. Figure 2.10 illustrates how the members deflect with temperature change and causes the residual force on the tines of the resonators in Design 2B.

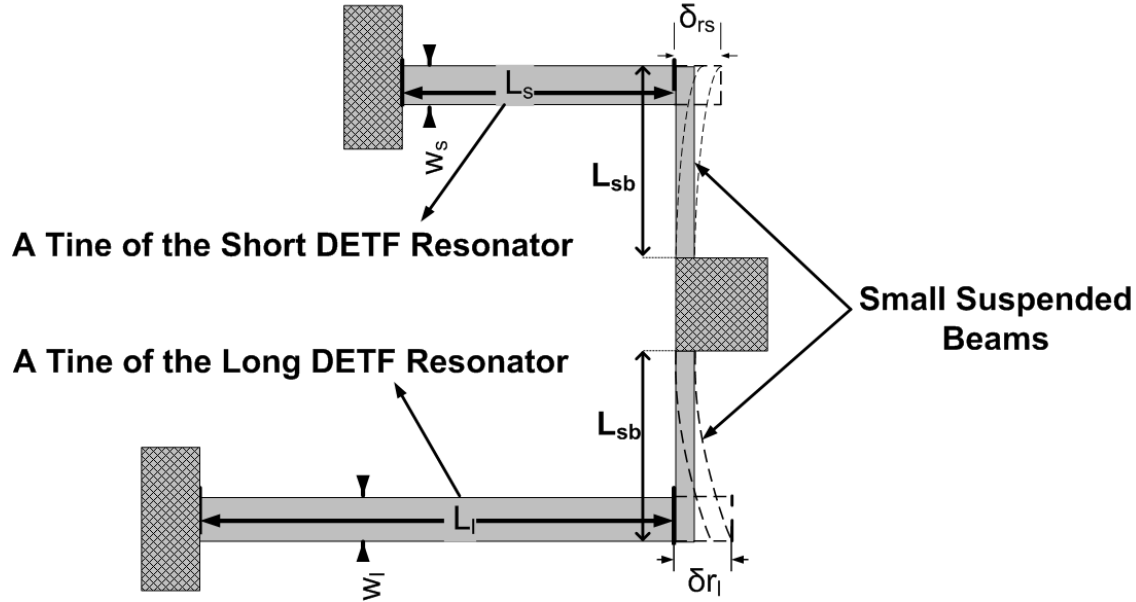


Figure 2.10: Simplified schematic of the resonator system offered in Design 2B. To avoid any confusion and for the sake of simplicity of the governing equations, only one tine of the resonators are shown in this figure. Note that the hatched areas represent the anchor regions while others show the suspended sensor structures in top view.

To include the axial force effect into the sensitivity equation of Design 2B, thermal strain equation of the tines of the resonators presented in (2.67), and deflection of the small beam (with the cantilever beam assumption) equation presented in (2.68) can be utilized as follows:

$$\delta_r = (\alpha_g - \alpha_{si}) L \Delta T + \varepsilon_{Tg} L \quad (2.67)$$

$$\delta_r = \frac{F_r L_{sb}^3}{3 E I_{sb}} \quad (2.68)$$

Where δ_r is the deflection at the end of the tine, which also indicates to the tip deflection of the small suspended beam, L stands for the length of the tine, F_r is the axial force created on the tine, L_{sb} is the length of the small suspended beam, and I_{sb} is the moment of inertia of the small suspended beam. Notice that the cap-substrate interaction is included to the deflection equation by adding the strain of the glass, ε_{Tg} , whose derivation is given in the previous section. When (2.67) and (2.68) are equalized and simplified to get F_r , the result occurs as follows:

$$F_r = \frac{[(\alpha_g - \alpha_{si}) L \Delta T + \varepsilon_{Tg} L] 3 E I_{sb}}{L_{sb}^3} \quad (2.69)$$

Then, by using (2.57) and (2.69) TCf can be found for the resonators in Design 2B:

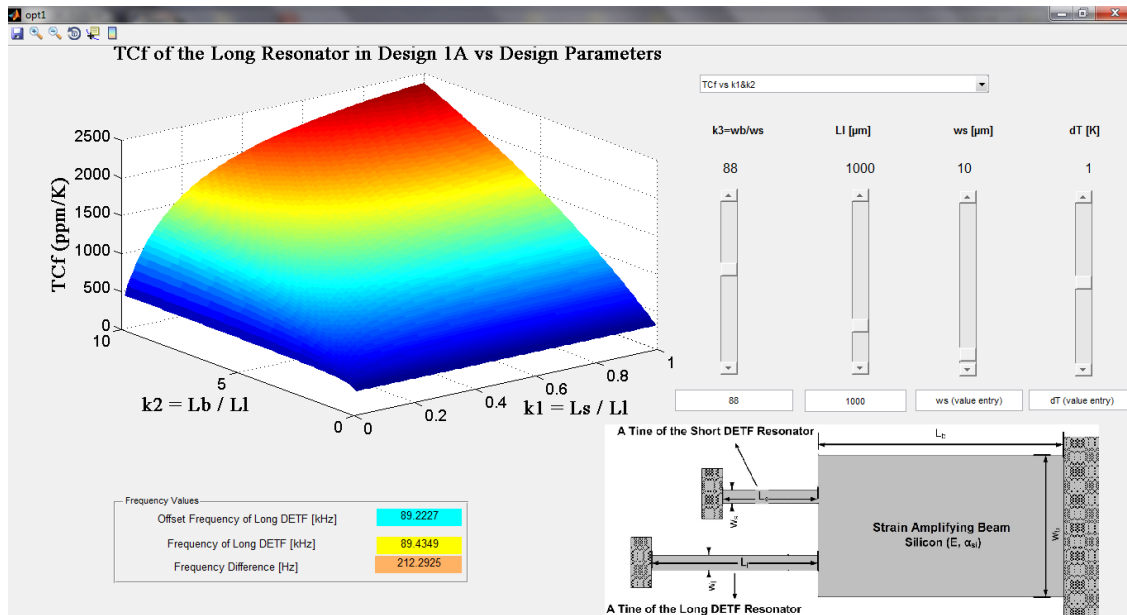
$$TCf_F = 0.5 B \frac{1}{f_n^2} \frac{[(\alpha_g - \alpha_{si}) L \Delta T + \varepsilon_{Tg} L] 3 E I_{sb}}{L_{sb}^3} \quad (2.70)$$

Where B is the coefficient appearing in (14) and supposed to be calculated for each resonator. Hence, the total TCf for both resonators used in Design 2B can be summed by utilizing equation (2.61):

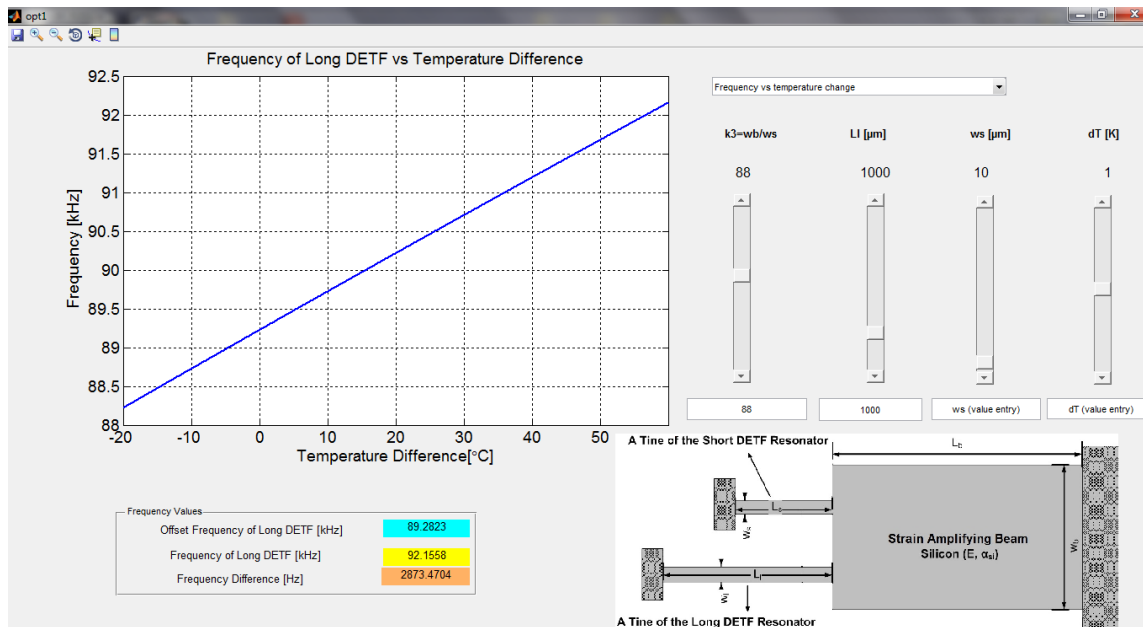
$$TCf = 0.5 B \frac{1}{f_n^2} \frac{[(\alpha_g - \alpha_{si}) L \Delta T + \varepsilon_{Tg} L] 3 E I_{sb}}{L_{sb}^3} + \frac{TCE_{si}}{2} \quad (2.71)$$

2.1.2.2 Determination of Geometric Properties of DETF Parameters

The determination of the critical parameters of the DETF resonators such as the width of the resonator tines, strain-amplifying beam or small suspended beam depending on the Design presented in the previous section is explained in this section. A Graphical User Interface (GUI) is created to perform this process of the resonator parameters by using Matlab. Figure 2.11 illustrates the overview of the GUI created for the optimization purposes.



(a)



(b)

Figure 2.11: Overview of the GUI created to determine the geometric parameters of the DETF resonators. **a)** The tab utilized to maximize TCF of the resonators by using the ratios of the key tine parameters. **b)** The tab utilized to see the frequency change of the long resonator with changing temperature for the entered geometric properties.

While creating the GUI, the temperature coefficient of frequency, TCF, is selected as the figure of merit to be maximized. TCF formulae introduced in the previous section are

employed and embedded into this GUI. TCf of the related design is calculated and plotted in 3D form in the created GUI while the parameters to be determined are matched with the sliders and value entry boxes below the sliders in order to easily see how the change of these parameters affect the TCf. The parameters that can be changed via the sliders or value entry boxes in GUI are the ratio of the certain resonator dimensions and key DETF resonator parameters such as the ratio of the width of the strain-amplifying beam to the width of the short DETF tine, the length of the long DETF tine, width of the short DETF tine and the amount of the temperature difference. Hence, the TCf expressions presented in the previous sections are modified with respect to these parameters before embedded into the code of the GUI. The parameters and their counterpart quantities are also shown on a figure placed at right bottom of the GUI in order to achieve a user-friendly interface.

The sensor parameters are selected by using this GUI and by considering the fabrication limitations. The fabrication know-how acquired in inertial-measurement-unit (IMU) sensors group in METU-MEMS Research and Applications Center is mostly what guides the determination of the critical sensor parameters. Table 2.1 presents the geometrical properties of the resonator systems employed in this thesis study after the optimization process by utilizing the GUI and considering the fabrication limitations and know-how gained in IMU group.

Table 2.1: Geometric properties of the DETF resonators offered in this thesis study.

Quantity	Design 1A		Design 1C		Design 2A		Design 2B	
	Short DETF	Long DETF	Short DETF	Long DETF	Short DETF	Long DETF	Short DETF	Long DETF
Length of the Tine (L)	500 μm	1000 μm	500 μm	1000 μm	500 μm	1000 μm	500 μm	1000 μm
Width of the Tine (w)	10 μm	10 μm	10 μm	10 μm	10 μm	10 μm	10 μm	10 μm
Length of The Capacitive Plate (L_p)	NA	NA	NA	NA	320 μm	770 μm	320 μm	770 μm
Width of The Capacitive Plate (w_p)	NA	NA	NA	NA	10 μm	10 μm	10 μm	10 μm
Length of The Connector (L_c)	NA	NA	NA	NA	120 μm	120 μm	120 μm	120 μm
Width of The Connector (w_c)	NA	NA	NA	NA	10 μm	10 μm	10 μm	10 μm
Length of The Strain-Amplifying Beam (L_b)	1000 μm		NA		1000 μm		NA	
Width of The Strain-Amplifying Beam (w_b)	880 μm		NA		1400 μm		NA	
Length of The Small Suspended Beam Connecting the Tines to the Anchor (L_{sb})	NA		NA		NA		340 μm	
Width of The Small Suspended Beam Connecting the Tines to the Anchor (w_{sb})	NA		NA		NA		20 μm	
Structural Thickness (h)	35 μm							

The critical parameters of the DETF resonators to be utilized as temperature sensors including the TCf values are obtained by using the mathematical models presented above and the geometric property values presented in Table 2.1. Table 2.2 presents the overview of the analytical model results.

Table 2.2: Analytical model results of the DETF resonators in the designs offered in this thesis study while the parameters presented in Table 2.1 are used in the governing equations.

Quantity	Design 1A		Design 1C		Design 2A		Design 2B	
	Short DETF	Long DETF	Short DETF	Long DETF	Short DETF	Long DETF	Short DETF	Long DETF
Mechanical Spring Constant (k_m) [N/m]	757.1	94.7	757.1	94.7	757.1	94.7	757.1	94.7
Electrostatic Spring Constant (k_e)* [N/m]	1.7	3.7	1.7	3.7	1.2	3.0	1.2	3.0
Effective Mass (m_{eff}) $\times 10^{-10}$ [kg]	1.5	3.0	1.5	3.0	5.1	10.3	5.1	10.3
Resonance Frequency (f) [Hz]	355,441	87,216	355,441	87,216	193,708	47,507	193,708	47,507
Calculated TCf_F [ppm/K]	233	652	81	335	236	653	~0	0.6
Overall TCf [ppm/K]	203	622	51	305	206	623	-30	-29

* Calculated for proof mass voltage of 10 V.

The calculated TCf values resulting from the axial force induced on the tines of DETF resonators are in good agreement with the objectives of each design. Design 2B resonators show no axial-force dependent TCf term (TCf_F) due to one-end free tine design while the DETF resonators in Design 1A and Design 2A indicate the highest TCf_F values. In Design 1C, the clamped-clamped DETF resonators have smaller TCf_F value according to the analytical model results, which indicates the effectiveness of the strain-amplifying beam utilized in Design 1A. The strain-amplifying beam is able to improve the TCf_F of the doubly-clamped DETF resonators up to 2-3 times depending on the geometric properties of the DETF structure according to the analytical model results presented in Table 2.2. The positive TCf values presented in Table 2.2 indicates the tensile stress on the axial direction of the tines which is a natural result of larger thermal

expansion coefficient of the glass ($\alpha_g=3.25 \times 10^{-6} \text{ 1/K}$) substrate than the sensor structure material, silicon ($\alpha_{si}=2.59 \times 10^{-6} \text{ 1/K}$).

2.1.3. Finite Element Modeling (FEM) Simulations of Temperature Sensors

Finite-element-modeling (FEM) simulations of the introduced resonant MEMS temperature systems are handled by using CoventorWare software. The main purpose of the FEM simulations is to verify the analytical model results presented in the previous sections and to be aware of the points that are missed in the design steps. The FEM simulations consist of two sub-sections: Modal Simulations and Thermal Simulations. Modal Simulations includes the frequency analysis of the resonator systems in order to observe the operation modes of the DETF resonators and other parasitic modes that may appear in the overall resonator system, whereas thermal simulations indicate how the proposed resonator systems operate under temperature change by observing the frequency of the desired operation modes with changing temperature.

2.1.3.1. Modal Simulations of the Resonator Systems

Modal simulations of the DETF resonators in the offered temperature sensor designs are achieved via CoventorWare, which is a MEMS-based FEM tool. 3D models of the resonators are obtained via Process Editor Tool of CoventorWare by utilizing the GDS files of the masks prepared by using L-Edit software. Only DETF structure parts are created in order to be utilized in the modal simulations since the modeling of other parts such as the substrate or cap leads to larger number of mesh elements, hence, increased simulation time.

The simulations are handled according to the number of modes, instead of defining frequency range. If the desired operation modes of both long and short resonators are observed in the simulations performed in the first 10 modes of the resonator system, no further modal simulations would be performed. If not, an extra modal simulation would be handled to be able to observe desired operation modes of both resonators. In addition to this simulation setting, the anchor surfaces of the resonator systems are fixed by using

the “*FixAll*” command as a surface boundary condition. Modal simulation results are presented in the following sub-sections. It should be noted that although there is one desired operation mode for the systems function properly by using capacitive actuation and detection principles presented previously, another “sibling” operation mode is also expected around the targeted resonance frequency, which is the in-phase mode of the tines. This phenomenon is explained in detail in [15], and will be presented in the figures in the following sections. Although the in-phase mode of the tines is supposed to have lower frequency response in magnitude, the fabrication imperfections may lead to a magnitude closer to the out-of-phase mode of the tines [42]. That makes the in-phase mode of the tines one of possible operation mode for the DETF resonators presented in this study. This phenomenon will also be mentioned in the test results chapter over the discussion on the characterization test results hereinafter.

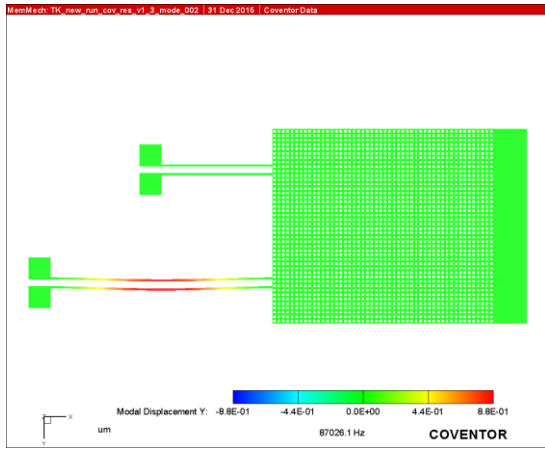
2.1.3.1.1. Modal Simulation Results of Design 1A

Modal simulation results of Design 1A introduced in the previous section is presented in Figure 2.12. The summary of all modes as the results of the performed modal analyses can be found in Table 2.1.

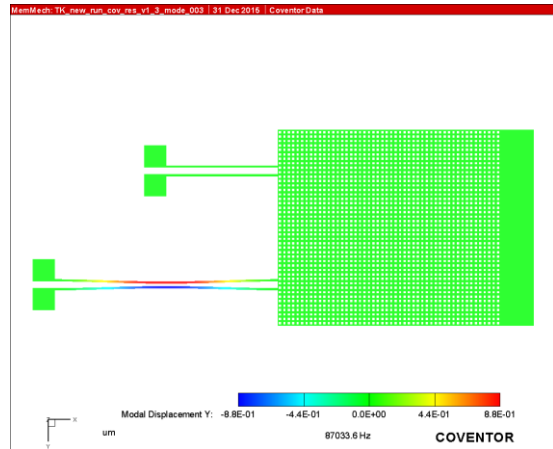
Table 2.3: Modal simulation results of the resonator structures in Design 1A. First 11 modes of the resonator system presented as Design 1A can be examined in the table.

Mode	Frequency (Hz)	Notes	Overview of Layout
1	66,638	Parasitic out-of-plane motion of the strain-amplifying beam	
2	87,026	In-phase operation mode of the long DETF resonator	
3	87,034	Out-of-phase operation mode of the DETF long resonator	
4	112,266		
5	239,536		
6	239,638		
7	245,731		
8	294,052		
9	319,428		
10	345,263	In-phase operation mode of the short DETF resonator	
11	345,723	Out-of-phase operation mode of the short DETF resonator	

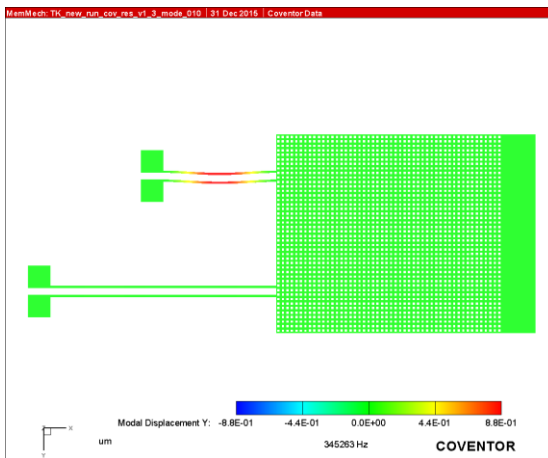
The frequencies of the aimed operation modes obtained from the modal simulations are in good agreement with the analytical solutions achieved by using equation (2.51). Although a parasitic mode caused by the twisting mode of the strain-amplifying beam is observed before the desired operation modes of the long resonator as seen in Table 2.3, that parasitic mode cannot lead to any considerable capacitance change necessary to appear as a peak when compared to the desired operation modes. Hence, no change is needed in the resonator system design.



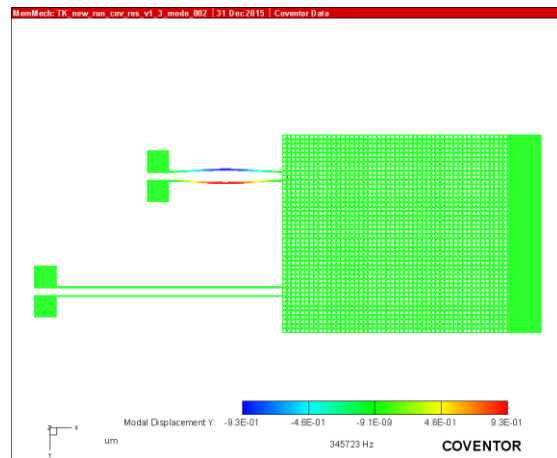
(a)



(b)



(c)



(d)

Figure 2.12: Modal simulation results obtained via CoventorWare for the resonators in Design 1A. Each resonator has two operation modes, called sibling modes, as presented in **a)** in-phase operation mode for the long resonator, **b)** out-of-phase operation mode for the long resonator, **c)** in-phase operation mode for the short resonator, and **d)** out-of-phase operation mode for the short resonator.

2.1.3.1.2. Modal Simulation Results of Design 1C

Modal simulation results of Design 1C are presented in Figure 2.13, which illustrates the desired operation modes of the resonators resulted from the modal simulations. The summary of all modes as the results of the performed modal analyses can be found in Table 2.4.

Table 2.4: Modal simulation results of the resonator structures in Design 1C. The desired operation modes can be seen in the first 10 modes of the resonator system as labeled below.

Mode	Frequency (Hz)	Notes	Overview of Layout
1	87,072	In-phase operation mode of the long resonator	
2	87,074	Out-of-phase operation mode of the long resonator	
3	239,760		
4	239,766		
5	304,736		
6	304,737		
7	345,649	In-phase operation mode of the short resonator	
8	345,668	Out-of-phase operation mode of the short resonator	
9	469,397		
10	469,410		

The desired operation modes of the long and short resonators are observed as 1st, 2nd and 7th, 8th modes in the modal simulations, as seen Table 2.4. The frequencies of the desired operation modes obtained from the modal simulations are in good agreement with the analytical solution results presented in Table 2.2.

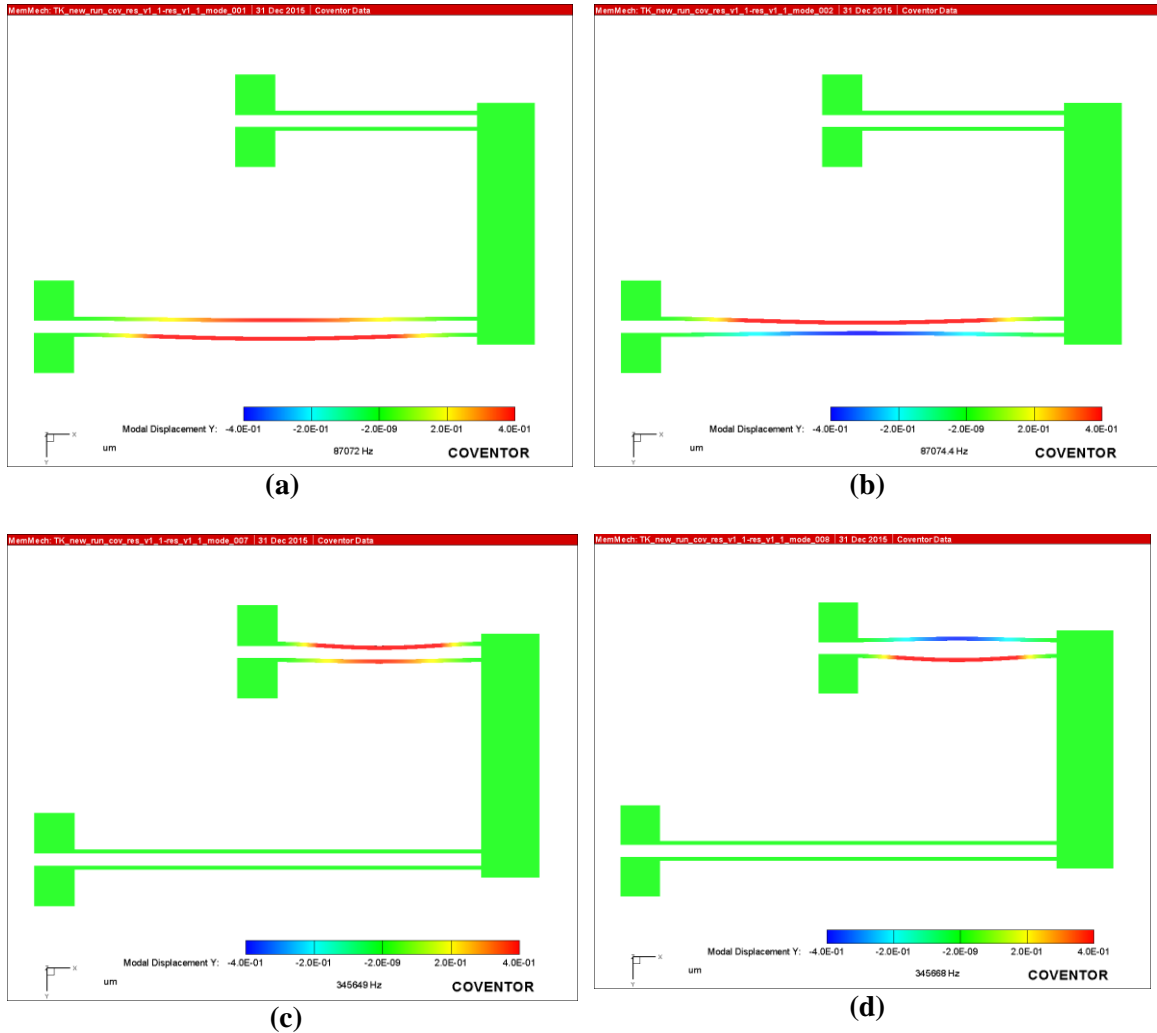
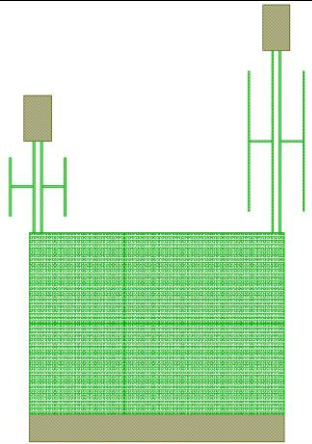


Figure 2.13: Modal simulation results obtained via CoventorWare for the resonators in Design 1C. Each resonator has two operation modes, called sibling modes, as presented in **a)** out-of-phase operation mode for the long resonator, **b)** in-phase operation mode for the long resonator, **c)** in-phase operation mode for the short resonator, and **d)** out-of-phase operation mode for the short resonator.

2.1.3.1.3. Modal Simulation Results of Design 2A

Modal simulation results of the resonators in Design 2A can be examined in Table 2.5 and Figure 2.14, where the desired operation modes of the long and short resonator in Design 2A are illustrated.

Table 2.5: Modal analysis results of the resonators in Design 2A showing the first 10 modes of the resonator system. Additionally, the modes of the short DETF resonator are presented below the first 10 modes.

Mode	Frequency (Hz)	Notes	Overview of Layout
1	39,375	Parasitic torsional modes of the additional plate	
2	39,376		
3	45,710	Out-of-phase operation mode of the long resonator	
4	45,719	In-phase operation mode of the long resonator	
5	53,117		
6	67,148		
7	67,628		
8	72,486		
9	73,748		
10	94,709		
19	189,245	In-phase operation mode of the long resonator	
20	189,360	Out-of-phase operation mode of the long resonator	

It should be noted that the desired operation modes of the short DETF resonator in Design 2A do not appear in the first 10 modes of the resonator system offered in Design 2A. Hence, another modal simulation is performed by starting the frequency range from 94 kHz then, the modal simulation results of the short DETF are added in Table 2.5. The desired operation modes of the resonators are in agreement with the analytical calculations presented in the previous section. The parasitic modes appearing before the desired operation modes of the long resonator are the torsional modes of the capacitive plates connected to the tines of the resonators. These modes are not expected to occur in the resonance tests since they did not cause an appreciable capacitance change that may lead to a peak when compared to the peaks of the operation modes. Hence, these parasitic modes are expected not to disturb the operation of the resonators.

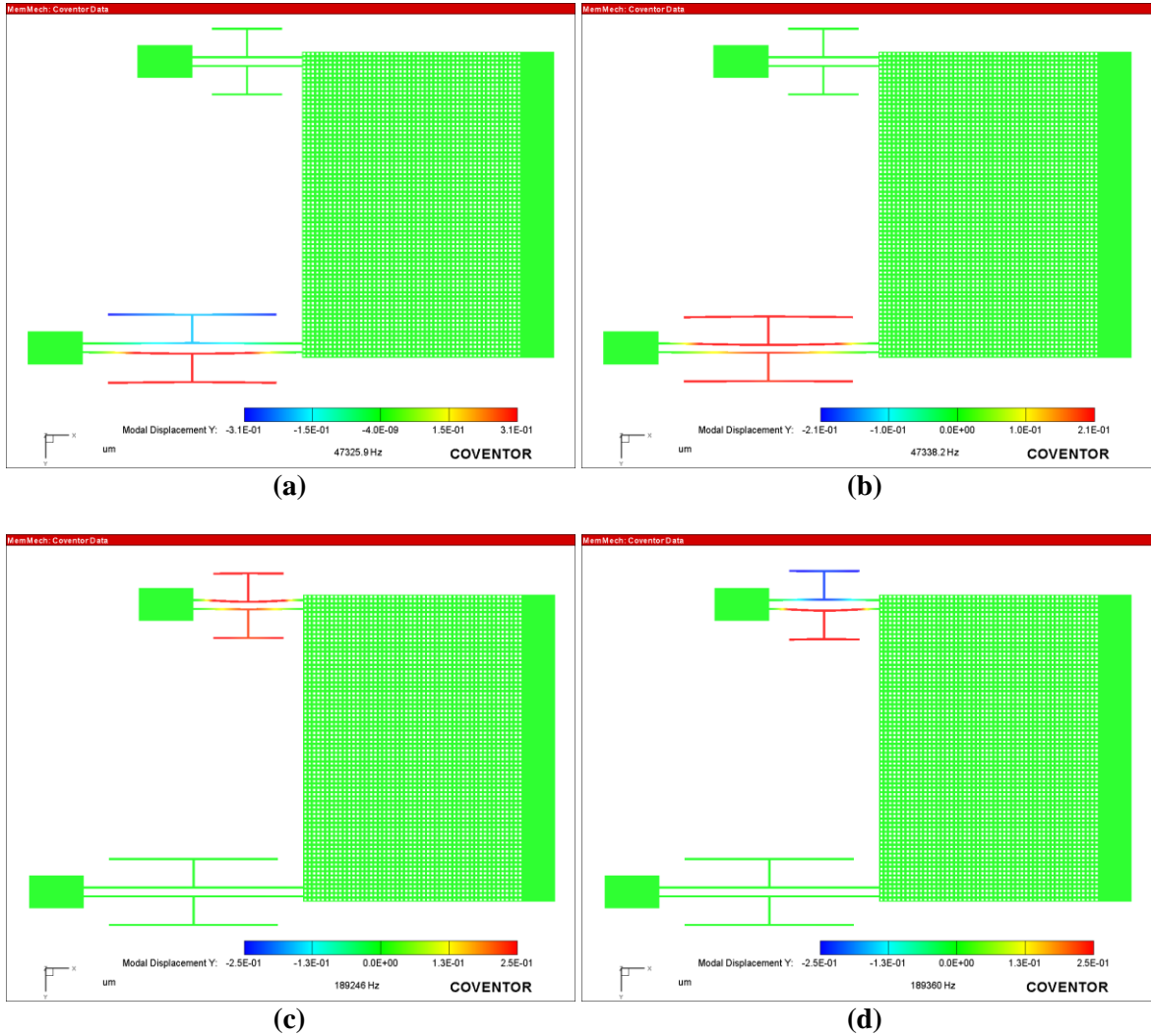
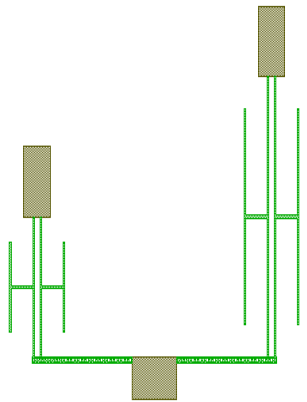


Figure 2.14: Modal simulation results obtained via CoventorWare for the resonators in Design 2A. Each resonator has two operation modes, called sibling modes, as presented in **a)** out-of-phase operation mode for the long resonator, **b)** in-phase operation mode for the long resonator, **c)** in-phase operation mode for the short resonator, and **d)** out-of-phase operation mode for the short resonator.

2.1.3.1.4 Modal Simulation Results of Design 2B

Modal simulation results of the resonators in Design 2B can be found in Table 2.6, and Figure 2.15, where the desired operation modes of the long and short resonator in Design 2B are illustrated.

Table 2.6: Modal simulation results of the resonators in Design 2B showing the first 10 modes of the resonator system. The operation modes of the short DETF resonator are added below the first 10 modes.

Mode	Frequency (Hz)	Notes	Overview of Layout
1	39,196	Parasitic buckling modes of the additional plate	
2	39,262		
3	44,319	In-phase operation mode of the long resonator	
4	44,774	Out-of-phase operation mode of the long resonator	
5	55,128		
6	67,052		
7	68,706		
8	71,387		
9	111,767		
10	122,759		
19	180,795	In-phase operation mode of the long resonator	
20	182,899	Out-of-phase operation mode of the long resonator	

The parasitic modes similar to the ones mentioned in the previous section can also be seen in this modal simulation, which is expected not to cause any problem with regard to the operations of the resonators.

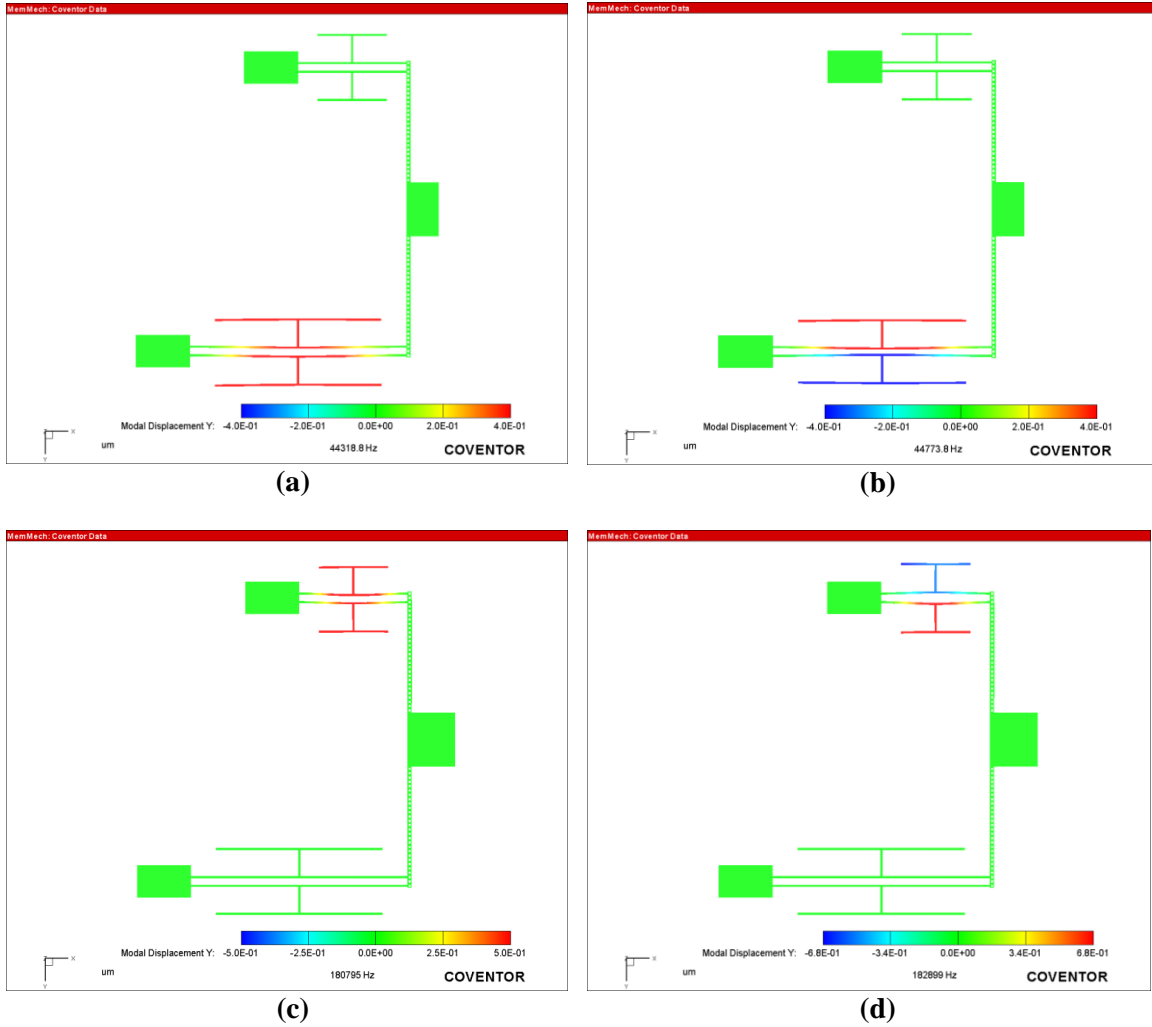


Figure 2.15: Modal simulation results obtained via CoventorWare for the resonators in Design 2B. Each resonator has two operation modes, called sibling modes, as presented in **a)** in-phase operation mode for the long resonator, **b)** out-of-phase operation mode for the long resonator, **c)** in-phase operation mode for the short resonator and **d)** out-of-phase operation mode for the short resonator.

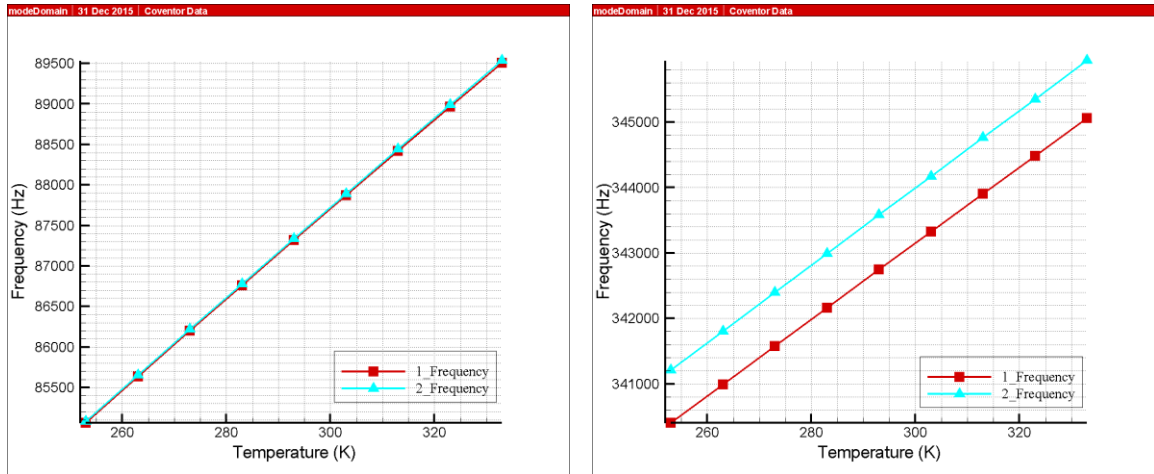
2.1.3.2 Thermo-mechanical Simulations of the Temperature Sensors

Thermo-mechanical analyses of the temperature sensors offered in this study are performed to simulate the operation of the resonators under temperature changes by using Thermo-mechanical Solver of CoventorWare. Simulations are held on the 3D models of the sensor die including the cap and substrate parts. 3D models are created via Process Editor of CoventorWare by using the GDS files obtained from L-Edit software. Changing temperature condition is provided by a transient analysis in which the

temperature of the overall system is changed in each step. “Tfixed” command is selected to implement the temperature change as a Volume Boundary Condition. The additional modal analysis is added to the simulations in order to monitor the frequency changes with respect to the changing temperature. Modal analyses are handled so that the frequency range includes only the desired operation modes of the resonators in order to shorten the long simulation times. Modal analyses are achieved by defining the stationary surfaces with “fixAll” command available under Surface Boundary Conditions section. The fixed surfaces are selected so that the expansions/contractions of the sensor structures are not limited by the “fixAll” command. In addition to the boundary conditions, the material properties changing with temperature are also added to the Material Property Editor by editing the material properties used in the simulations. At the end of the thermo-mechanical simulations, the stress occurred on the tines of the DETF resonators and the frequency changes of the operation modes of each resonator are extracted from the simulation results. These results are presented in the following sub-sections with the tables and visuals.

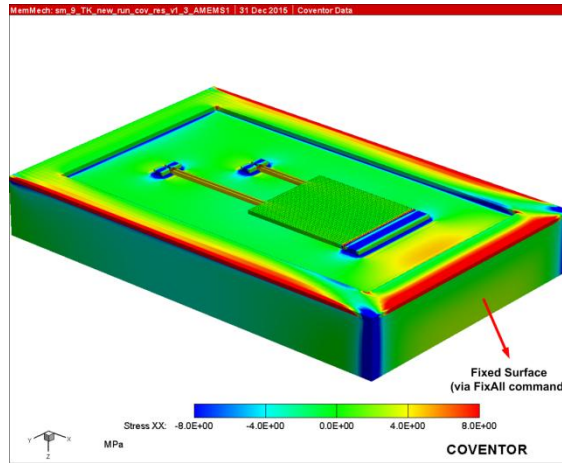
2.1.3.2.1 Thermo-mechanical Simulation Results of Design 1A

The thermo-mechanical simulations are performed in 9 steps starting from 253 K and increasing the temperature by 10 K increments in each step until it reaches 333 K. The results of the thermo-mechanical simulations of Design 1A are presented as “frequency versus temperature” plot for the temperature range in between 253 K and 333 K in Figure 2.16 (a-b). Figure 2.16 (c), on the other hand, illustrates the stress along the axial direction of the resonator tines.



(a)

(b)



(c)

Figure 2.16: Thermal simulation results of Design 1A. The simulation was held for the range in between $-20\text{ }^{\circ}\text{C}$ and $60\text{ }^{\circ}\text{C}$ by collecting data for each $10\text{ }^{\circ}\text{C}$ increment. The resonance frequency shift of long resonator and the resonance frequency shift of long resonator for both operation modes can be seen in **a)** and **b)**, respectively. The resulting TCf for the long resonator is calculated as 638 ppm/K , whereas it is found as 172 ppm/K for the short resonator in Design 1A. The axial stress induced along the tines of DETF resonators at $60\text{ }^{\circ}\text{C}$ is presented in **c)**. The axial stress induced on the tines of the long and short resonators is around $5\text{-}6\text{ MPa}$, respectively. Note that the cap of the die is hidden in **c)** for the clear visualization.

Temperature coefficient of frequency (TCf) value for each resonator is calculated by using the results of thermo-mechanical simulations as 638 ppm/K and 172 ppm/K for the long and short resonator, respectively, which are in agreement with the analytical model results.

2.1.3.2.2 Thermo-mechanical Simulation Results of Design 1C

The thermo-mechanical simulations are performed in 9 steps in the similar way stated in the previous section. Figure 2.17 (a-b) show the “frequency versus temperature” plots of the long and short resonator in Design 1C, while Figure 2.17 (c) illustrates the stress along the axial direction of the resonator tines.

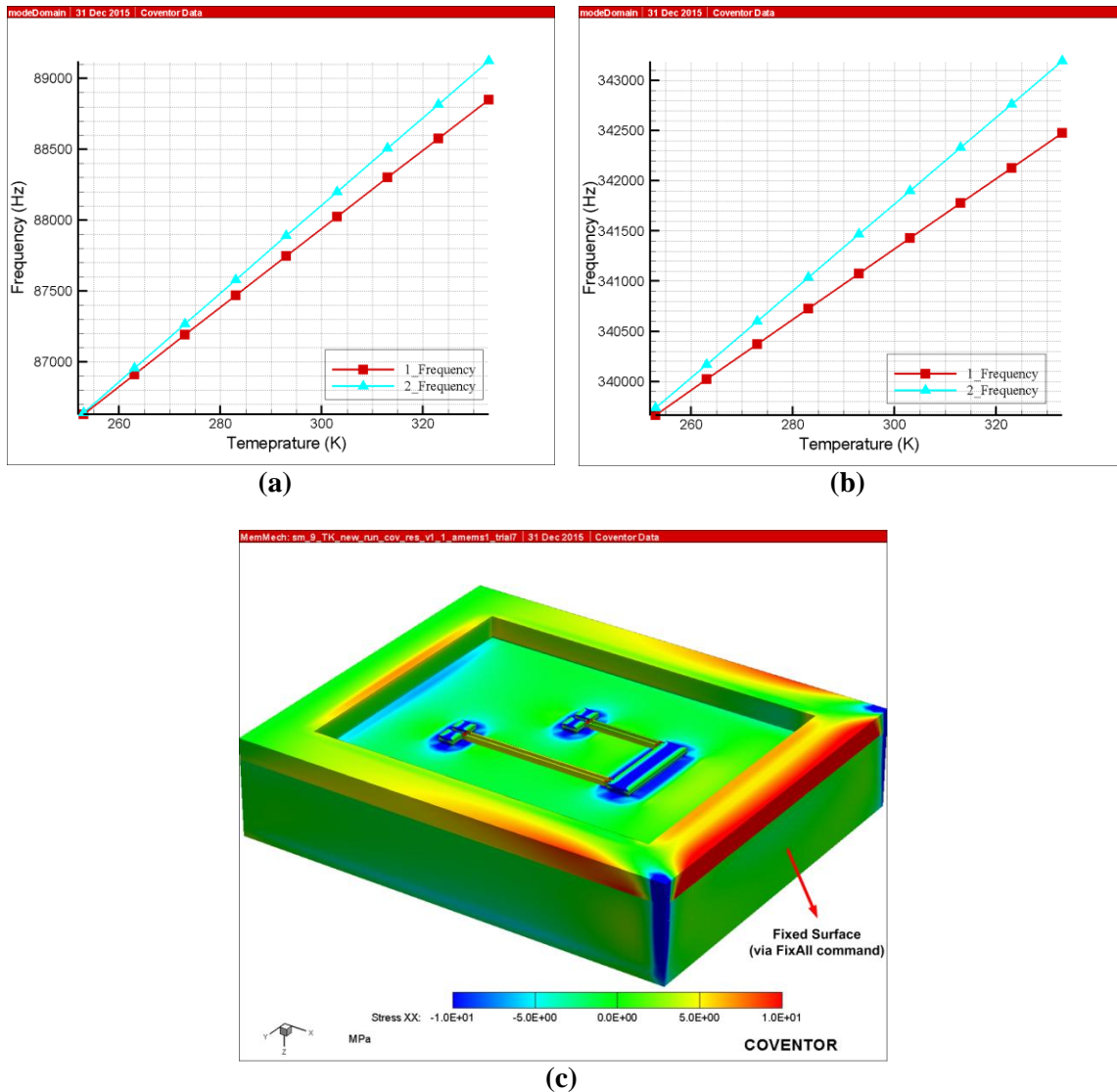


Figure 2.17: Thermal simulation results of Design 1C. The simulation was held for the range in between $-20\text{ }^{\circ}\text{C}$ and $60\text{ }^{\circ}\text{C}$ by collecting data for each $10\text{ }^{\circ}\text{C}$ increment. The resonance frequency shift of long resonator and the resonance frequency shift of long resonator for both operation modes can be seen in **a)** and **b)**, respectively. The resulting TCf for the long resonator is calculated as 323 ppm/K and 351 ppm/K for the in-phase and out-of-phase operation modes, respectively, whereas it is found as 104 ppm/K and 127 ppm/K for the short resonator in Design 1C. The axial stress induced along the tines of DETF resonators at $60\text{ }^{\circ}\text{C}$ is presented in **c)**. The axial stress induced on the tines of

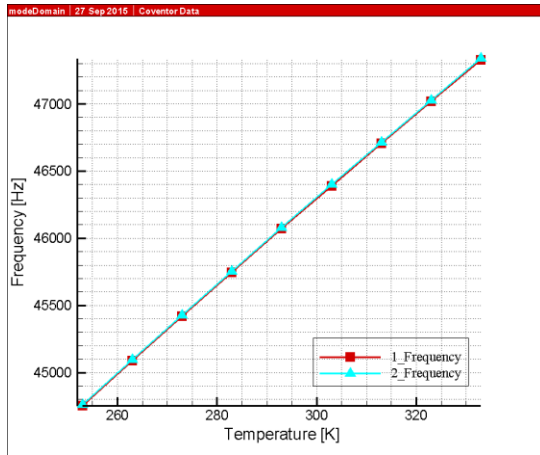
short and long DETF resonators is around 2-3 MPa. Note that the cap of the die is hidden in c) for the clear visualization.

Temperature coefficient of frequency (TCf) value for each resonator is calculated by using the results of thermo-mechanical simulations as presented in figure caption. There is a slight difference in TCf values of the in-phase and out-of-phase modes for each resonator which may be a result of improper meshing preventing the mechanical coupling of the tines. Despite that slight difference in TCf values of each resonator, the resulting TCfs are still in good agreement with the analytical model results.

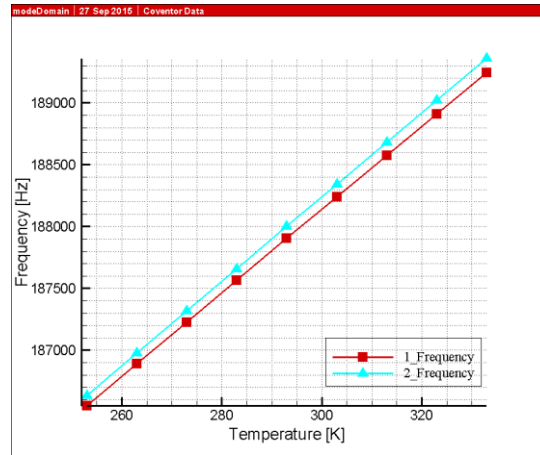
2.1.3.2.3 Thermo-mechanical Simulation Results of Design 2A

The results of thermo-mechanical simulations performed in between the temperature range of 253 K and 333 K in the similar are introduced in Figure 2.18 (a-b), showing the “frequency versus temperature” plots of the long and short resonator in Design 2A, while Figure 2.18 (c) illustrates the stress along the axial direction of the resonator tines.

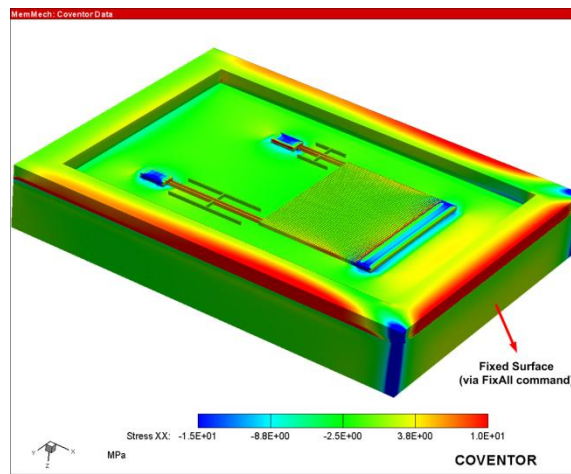
Temperature coefficient of frequency (TCf) value for each resonator is calculated by using the results of thermo-mechanical simulations as 697 ppm/K and 180 ppm/K for the long and short resonator, respectively, which are in agreement with the analytical model results.



(a)



(b)

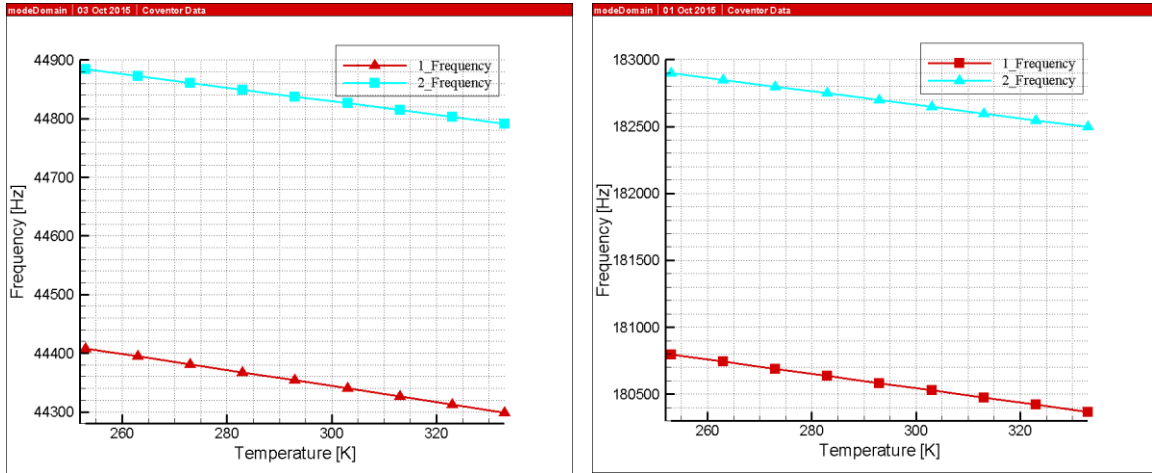


(c)

Figure 2.18: Thermal simulation results of Design 2A. The simulation was held for the range in between $-20\text{ }^{\circ}\text{C}$ and $60\text{ }^{\circ}\text{C}$ by collecting data for each $10\text{ }^{\circ}\text{C}$ increment. The resonance frequency shift of long resonator and the resonance frequency shift of long resonator for both operation modes can be seen in **a)** and **b)**, respectively. The resulting TCf for the long resonator is calculated as 697 ppm/K , whereas it is found as 180 ppm/K for the short resonator in Design 2A. The axial stress induced along the tines of DETF resonators at $60\text{ }^{\circ}\text{C}$ is presented in **c)**. The axial stress induced on the tines of the long resonator is around 5 MPa while it is around 4 MPa for the short resonator. Note that the cap of the die is hidden in **c)** for the clear visualization.

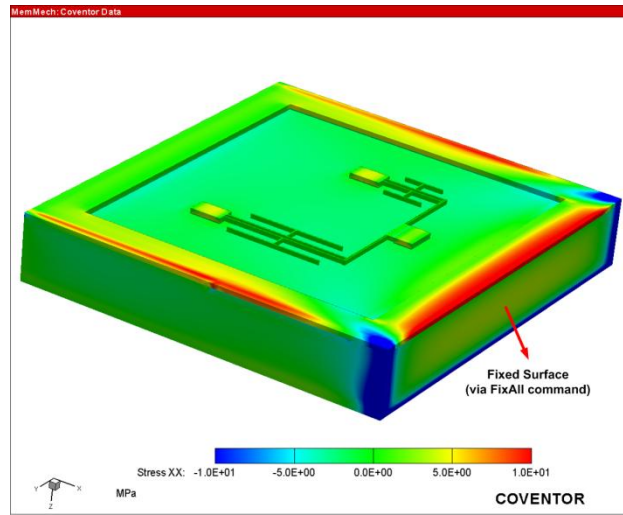
2.1.3.2.4 Thermo-mechanical Simulation Results of Design 2B

The results of thermo-mechanical simulations performed in between the temperature range of 253 K and 333 K in the similar are introduced in Figure 2.19 (a-b), showing the “frequency versus temperature” plots of the long and short resonator in Design 2B, while Figure 2.19 (c) illustrates the stress along the axial direction of the resonator tines.



(a)

(b)



(c)

Figure 2.19: Thermal simulation results of Design 2B. The simulation was held for the range in between $-20\text{ }^{\circ}\text{C}$ and $60\text{ }^{\circ}\text{C}$ by collecting data for each $10\text{ }^{\circ}\text{C}$ increment. The resonance frequency shift of long resonator and the resonance frequency shift of long resonator for both operation modes can be seen in **a)** and **b)**, respectively. The resulting TCf for the long resonator is calculated as -30 ppm/K , whereas it is found as -31 ppm/K for the short resonator in Design 2B. The axial stress induced along the tines of DETF resonators at $60\text{ }^{\circ}\text{C}$ is presented in **c)**. The axial stress induced on the tines of the both resonators is below 1 MPa . Note that the cap of the die is hidden in **c)** for the clear visualization.

Temperature coefficient of frequency (TCf) value for each resonator is calculated by using the results of thermo-mechanical simulations as -30 ppm/K and -31 ppm/K for the long and short resonator, respectively, which are in agreement with the analytical model results. Table 2.7 presents the comparison of the thermo-mechanical results and the analytical model results.

Table 2.7: Comparison of the mathematical model results and thermo-mechanical simulation results showing the TCF of the counterpart designs.

Quantity	Temperature Coefficient of Frequency [ppm/K]							
	Design 1A		Design 1C		Design 2A		Design 2B	
	Short DETF	Long DETF	Short DETF	Long DETF	Short DETF	Long DETF	Short DETF	Long DETF
Mathematical Model Results	203	622	51	305	206	623	-30	-29
Thermal Simulation Results	172	638	115*	337*	180	697	-30	-31

*Average TCF calculated for the in-phase and out-phase operation mode.

2.2 Design of Read-out Electronics of Resonant MEMS Temperature Sensors

MEMS temperature sensors used in this study are operated in the closed-loop configuration during the tests. The closed-loop operation of the resonators in temperature sensor design is achieved with the help of the analog read-out circuit designed for this purpose. The closed-loop operation of MEMS temperature sensors is essential to achieve real-time data acquisition from the resonators. The real-time data acquisition from the resonators will enable the use of MEMS resonators as sensitive temperature sensors to compensate the performance degradations of the sensors that are integrated with. The real-time data collection is important to detect the instant temperature fluctuations and resulted performance deteriorations, which is one of major motivations in this study. In the following sections, the overall read-out circuit together with its components in it is introduced in Section 2.2.1 and some circuit simulations are presented in Section 2.2.2.

2.2.1 Overview of Read-out Electronics Designed for MEMS Temperature Sensors

The closed-loop operation of the MEMS temperature sensors can be achieved with variety of ways. Among those ways, the proposed electronic circuit is designed so that it provides zero-phase difference for the signal circulating in the loop and the gain that is above unity to ensure the closed-loop operation for the resonators, i.e., self-resonance of

the resonators [43]. Figure 2.20 presents the schematic of the self-resonance loop used for the oscillations of the resonators. There are 4 main parts which provides the self-resonance of the resonators in the read-out circuit. First stage is the trans-impedance-amplifier (TIA) stage which is connected to the one electrode of the resonator. TIA includes a simple operational amplifier together with a resistor and capacitor, and it converts the current flowing through the electrode to the voltage when the capacitance between the tines and the electrode changes due to the resonance of tines in in-plane operation mode. Second part is the phase shifter stage used to remove phase lag or lead in the loop. The phase of the signal circulating in a loop should not be lagged or led in the loop in order to sustain the signal, i.e., the resonance signals in this case, circulating in the loop as mentioned before [43]. Hence the phase shifter stage is essential in the read-out circuit for the closed-loop operation of the resonators. A potentiometer is utilized in the phase shifter stage to arrange the amount of phase difference in the loop, which helps the user tuning the frequency of the signal in the self-resonance loop by means of that potentiometer. Third part is the inverting-amplifier stage to amplify the weak signal present in the loop due to small capacitances of DETF type resonators. This amplifier stage strengthens the signal in the loop each time in order to guarantee the necessary gain which is above unity to sustain the self-resonance operation of the resonators. Finally, the fourth stage belongs to the modulator which converts the DC input signal to the square wave by using the AC signal coming from the gain stage in front of it, and sends that square wave to the drive electrode of the resonator as the drive signal. A high pass filter is placed before the signal enters the modulator in order to remove offset from the signal for the effective modulation process. A buffer stage is also utilized in order to prevent any unintended current that may be pulled by the modulator.

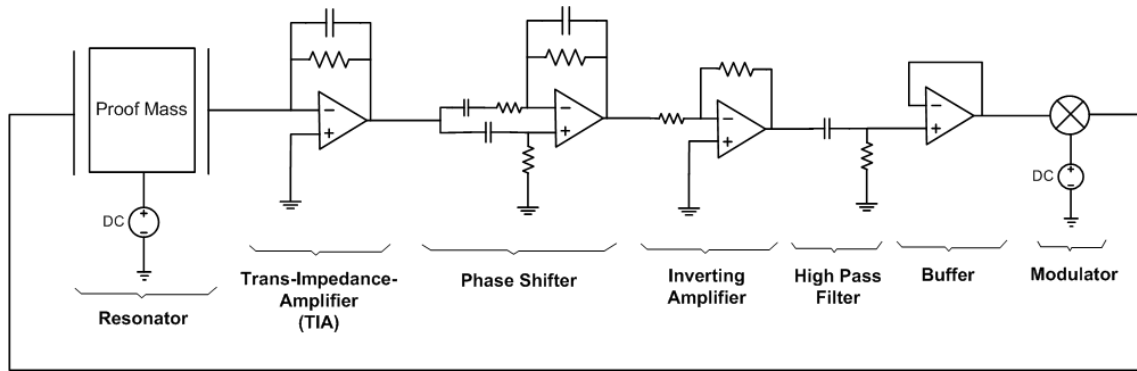


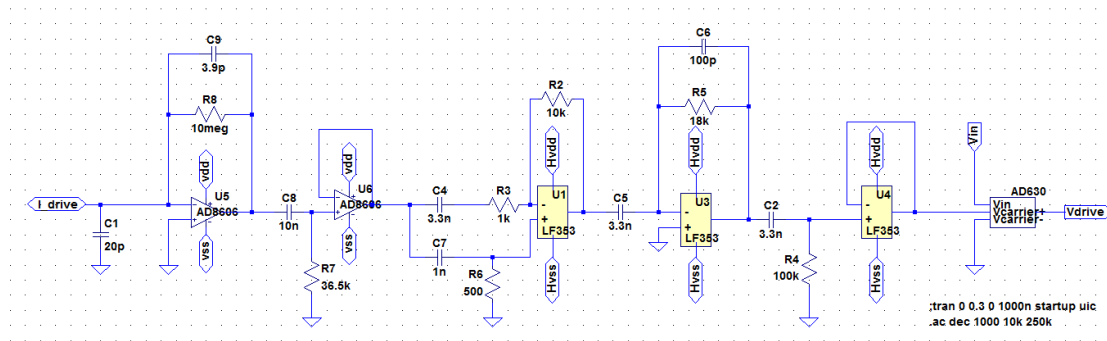
Figure 2.20: Schematic of the read-out circuit utilized to sustain self-resonance of the resonators in each design.

The values of the resistors and capacitors shown in Figure 2.20 are determined according to the LT Spice simulations. The LT Spice simulations are performed for each resonator design introduced as Design #1 and Design #2 since they have different resonance frequencies for each resonator. In the next section, LT Spice simulation results are presented.

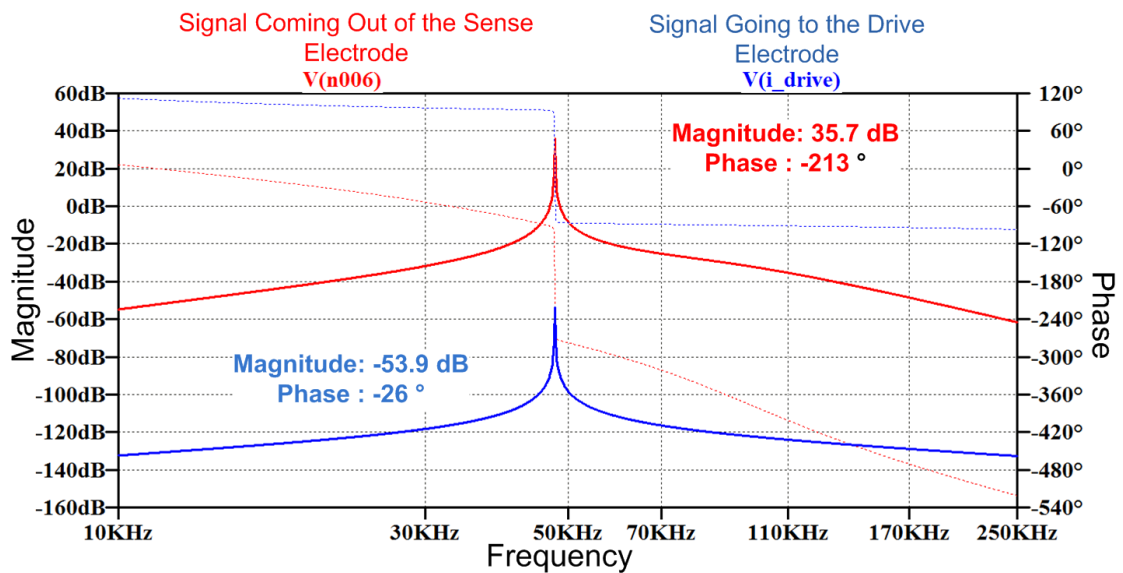
2.2.2 LT Spice Simulations of Read-out Electronics of MEMS Temperature Sensors

The self-resonance loop introduced in the previous section is aimed to function as a band-pass filter that puts forward the frequency bandwidth containing the desired operation frequency of the related resonator while suppressing the other frequency bandwidth of the parasitic modes of the resonator system. Hence, the read-out circuit of the resonators is modeled in LT Spice environment in order to define the operation bandwidth of the self-resonance loop. The values of the components used in the circuit are determined by the means of AC analyses, basically frequency response analyses, held in LT Spice environment. In AC analyses, the drive signal fed to the sensor model is supplied from an AC source while the frequency response of each node in the circuit can be monitored. The sensor model where the resonator properties such as spring constant, mass, sensitivity, quality factor etc. can be entered numerically contains the mathematical relations regarding to the operation of the resonator including the equation of motion relations, and capacitive actuation-detection relations presented previously, i.e., transfer function relations presented in (2.34). The bandwidth of the circuit is arranged to boost four different frequency ranges, including 47 kHz, 86 kHz, 186 kHz

and 343 kHz, belonging to the long and short DETF resonators in Design #2 and Design #1, respectively. Figure 2.21, Figure 2.22, Figure 2.23 and Figure 2.24 show the schematic of the created read-out circuit with the determined values of the components, and the AC analysis results of the drive and sense signals of the relevant DETF resonators.

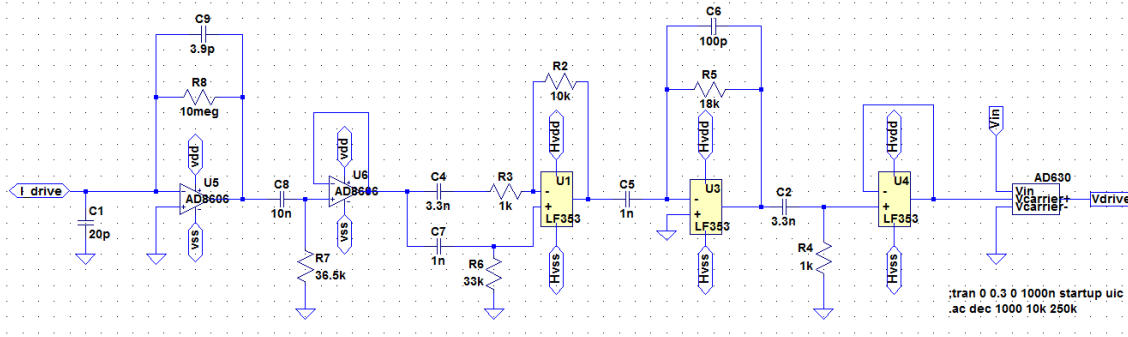


(a)

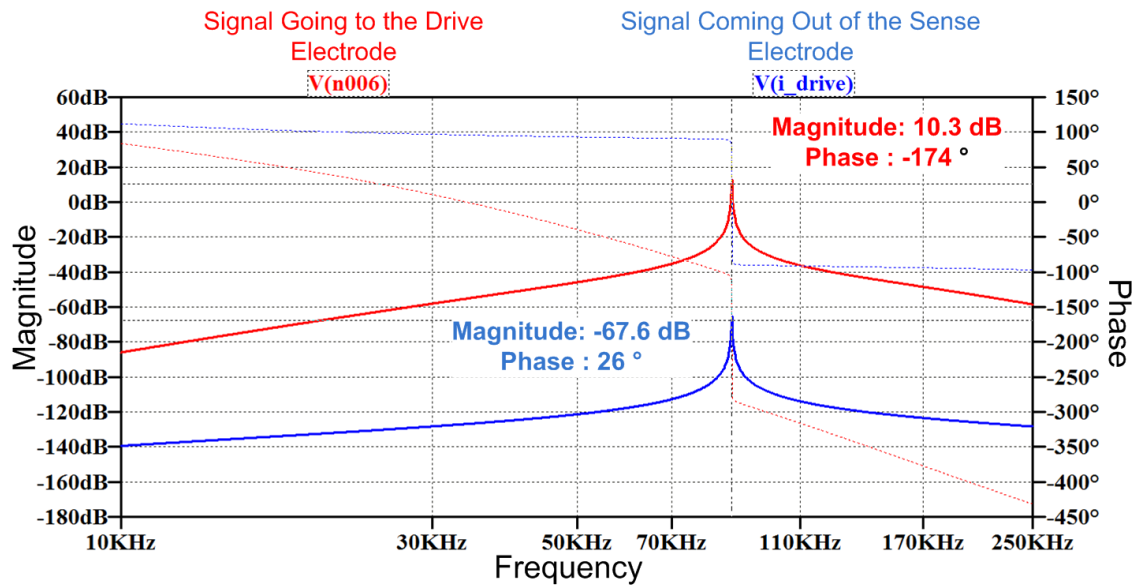


(b)

Figure 2.21: a) Schematic of the read-out circuit presented with the components used in frequency response and transient response analyses. b) The result of frequency response analyses of the read-out circuit belonging to long DETF resonators in Design 2A and 2B.

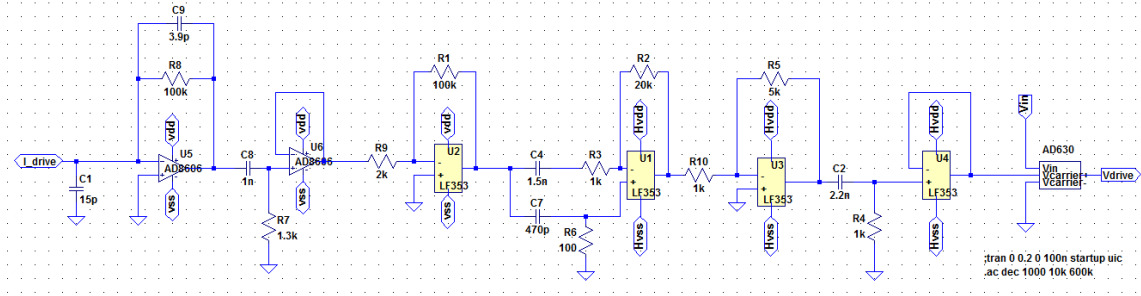


(a)

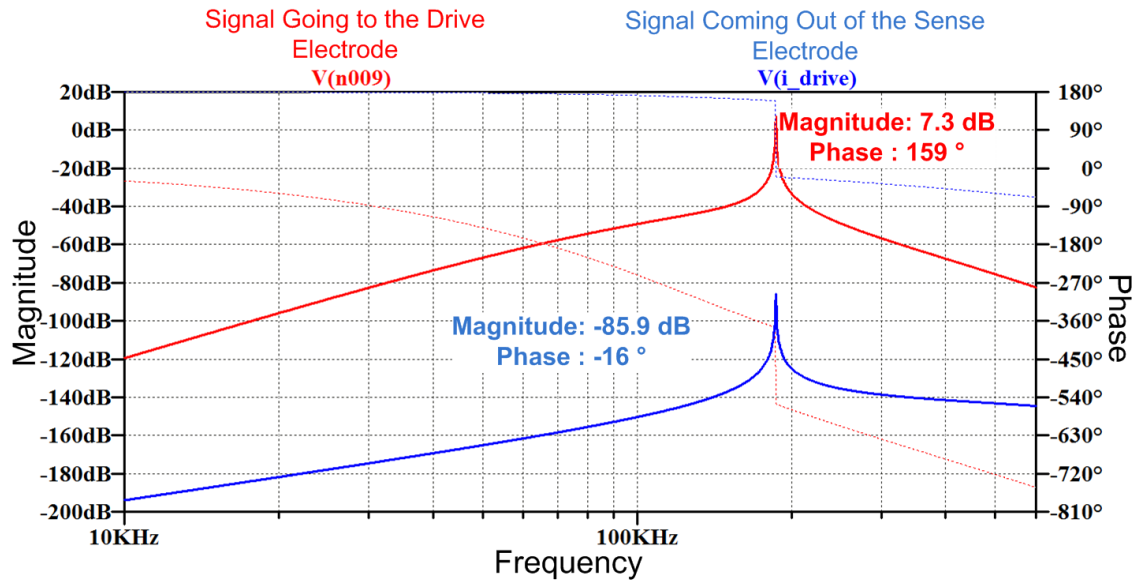


(b)

Figure 2.22: **a)** Schematic of the read-out circuit presented with the components used in frequency response and transient response analyses. **b)** The result of frequency response analyses of the read-out circuit belonging to long DETF resonators in Design 1A and 1C.



(a)



(b)

Figure 2.23: a) Schematic of the read-out circuit presented with the components used in frequency response and transient response analyses. b) The result of frequency response analyses of the read-out circuit belonging to short DETF resonators in Design 2A and 2B.

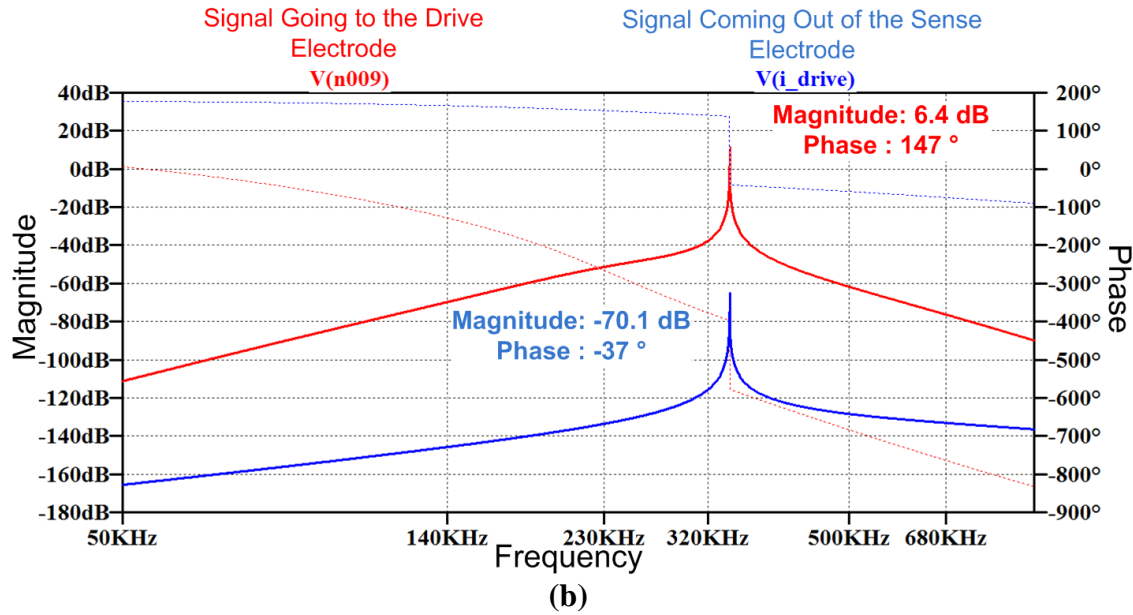
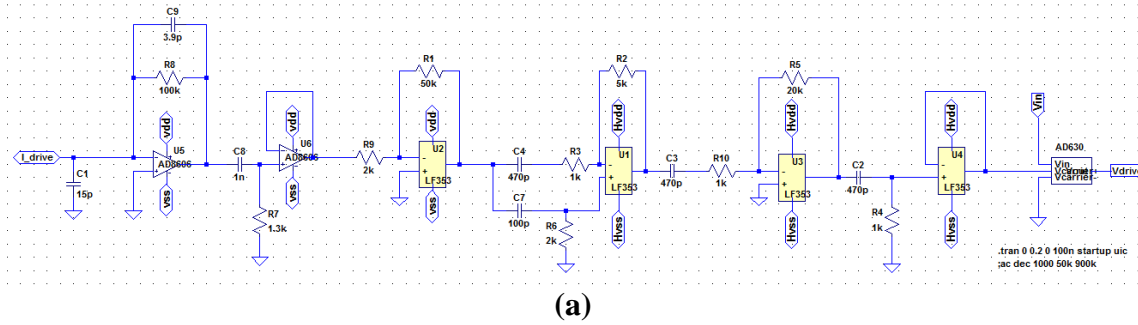


Figure 2.24: **a)** Schematic of the read-out circuit presented with the components used in frequency response and transient response analyses. **b)** The result of frequency response analyses of the read-out circuit belonging to short DETF resonators in Design 1A and 1C.

The AC analyses of the read-out circuits of the resonators are held by breaking the self-resonance loop, and supplying the drive signal with the help of an AC source. Therefore, the circuit still uses the sensor characteristics by passing through the sensor model created in LT Spice environment. The peak magnitude and phase results at the resonance of the resonators presented in the above figures show the signal at the input of the modulator and sense signals of the resonator. There is $\sim 180^\circ$ phase difference between those signals as shown in the figure. It should be noted that the phase difference will be overcome when the resonance takes place, which shifts the phase 180° . The values of the resistors and capacitors are picked and mounted on the test PCB according to the AC analysis results introduced. The potentiometers used in the phase shifter stage, R6 in the

schematics, are also selected so that they include the resistance shown in the circuit schematic in the figures.

The transient analyses of the read-out circuits are also performed via LT Spice. The whole circuit forms the self-resonance loop by connecting the output of the modulator to the drive signal of the sensor model while the current coming out of the sense electrode is fed to the circuit shown in Figure 2.20. The transient analyses are set to a time when the signal reaches the steady state. Figure 2.25, Figure 2.26, Figure 2.27 and Figure 2.28 presents the results of the transient analyses results of each read-out circuit.

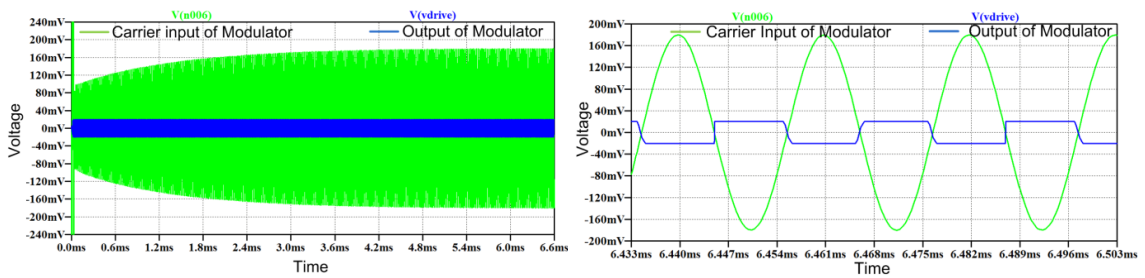


Figure 2.25: Transient analyses results of the read-out circuit belonging to long DETF resonator utilized in Design #2. The frequency oscillating in the loop is at 47 kHz.

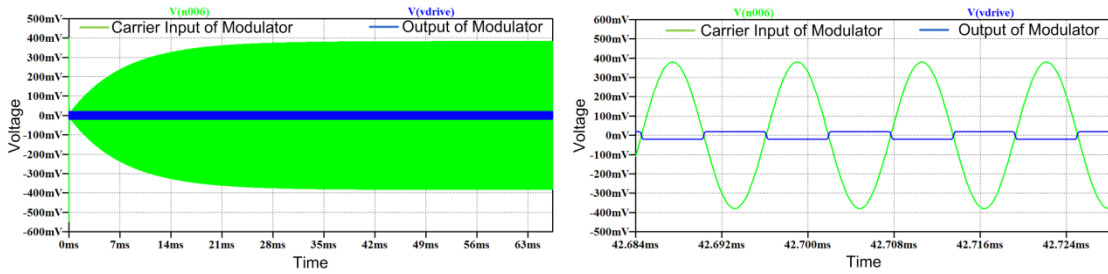


Figure 2.26: Transient analyses results of the read-out circuit belonging to long DETF resonator utilized in Design #1. The frequency oscillating in the loop is at 86 kHz.

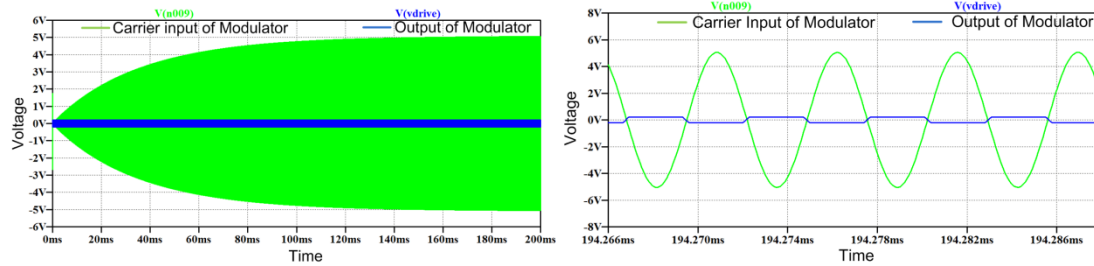


Figure 2.27: Transient analyses results of the read-out circuit belonging to long DETF resonator utilized in Design #1. The frequency oscillating in the loop is at 186 kHz.

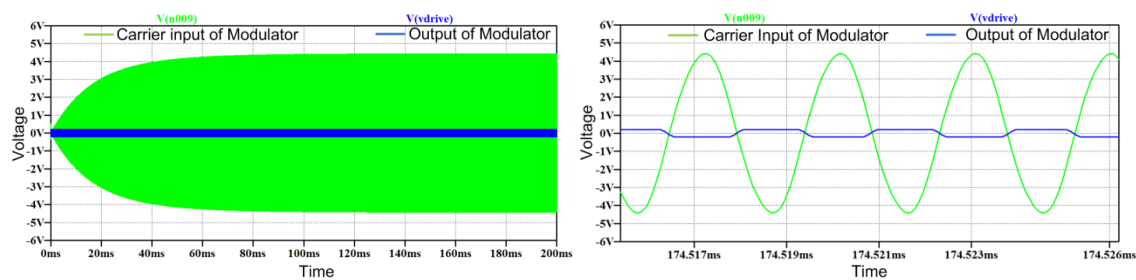


Figure 2.28: Transient analyses results of the read-out circuit belonging to short DETF resonator utilized in Design #1. The frequency oscillating in the loop is at 343 kHz.

The transient analyses indicate that the circuit formed with the components whose values are shown in the above figures will be able to sustain the desired resonance of the associated resonators. Hence, these read-out circuits will be utilized in the tests. The resonance frequencies of the DETF resonators probably will be reduced a few kHz due to inevitable undercuts and fabrication imperfections. However, these deviations seen in resonance frequencies will not cause a major problem for the operation of MEMS temperature sensors.

2.3 Design of Capacitive MEMS Accelerometers

Capacitive MEMS accelerometers are used in various applications including the industrial and research-based applications [44, 45]. This wide range of use of capacitive MEMS applications leads to capacitive MEMS accelerometers with multi-tasking capabilities such as multi-axis accelerometer designs [46, 47]. However, this brings extra issues due to complex structures and read-out circuit elements. Hence, capacitive

MEMS accelerometers used in this study are selected to be the single-axis type accelerometers in order to prevent the complex electronics. The single-axis accelerometers enable sensing the acceleration component belonging to a certain direction only. The design process of the single-axis accelerometer structures is introduced briefly in this section, since the main focus of this thesis study is MEMS temperature sensors offered in the previous section. The single-axis capacitive MEMS accelerometers are used only in exemplification of use of the MEMS temperature sensors. For further information about the capacitive MEMS accelerometers can be found in [48, 49]. In this section, first, operation principle basics of capacitive MEMS accelerometers are introduced in Section 2.3.1. Then, the mechanical design of the accelerometer components are presented in Section 2.3.2 while some FEM simulation results are exhibited in Section 2.3.3. Finally, the electronic read-out circuit of the capacitive MEMS accelerometer is presented in the next section, Section 2.4.

2.3.1 Operation Principle of Capacitive MEMS Accelerometers

Capacitive MEMS accelerometers perform acceleration sensing operation by means of its components: the sensing element, and the electronic read-out circuit. The sensing element is the physical structure of the sensor, while the electronic read-out circuit performs the acceleration-voltage conversion by using the capacitive actuation and sensing methods. The sensing element of the capacitive MEMS accelerometer is composed of 3 main components: the suspended proof mass structure, spring structures and electrode structures. Figure 2.29 illustrates the schematic of the single-axis accelerometer by labeling each component of the sensing element.

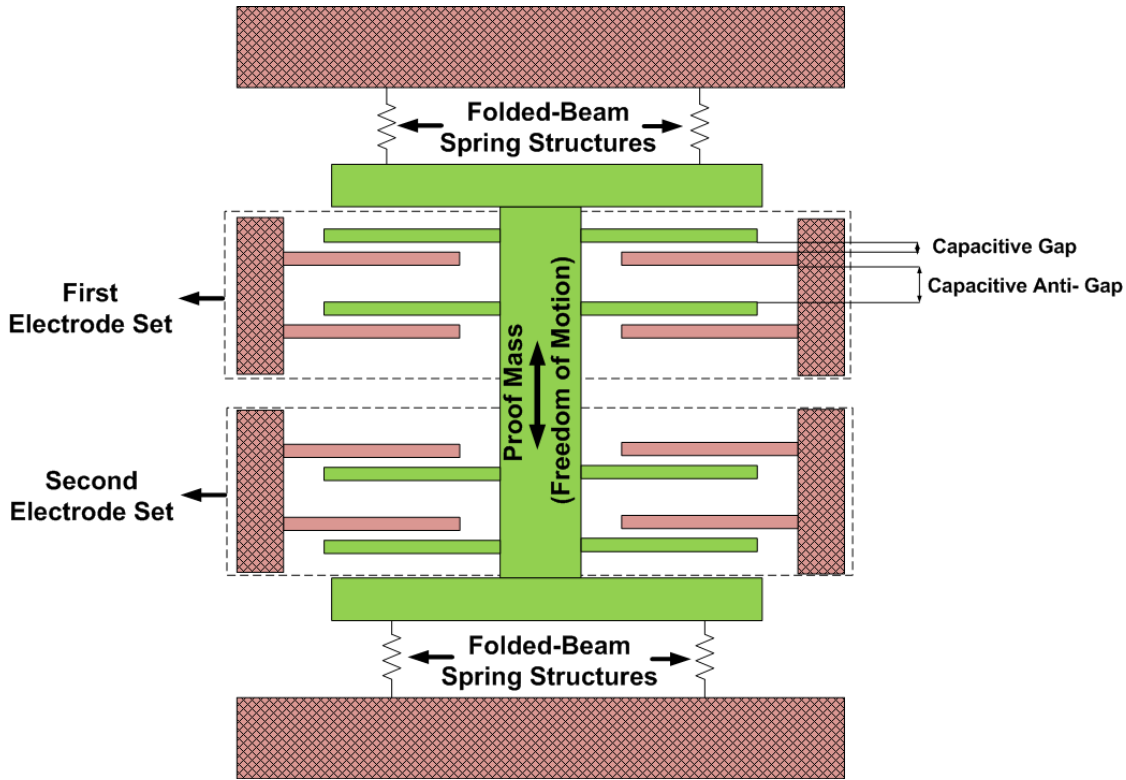


Figure 2.29: Schematic of the sensing element of the capacitive MEMS accelerometer used in this thesis study. The components of the sensing element are labeled on the figure for illustrative purposes.

The proof mass of the capacitive MEMS accelerometers are suspended by means of the spring structures, which means that the proof mass structure is able to move in a certain direction determined by the spring structures. The proof mass structures displace under the effect of acceleration which causes a capacitance change between the proof mass and the electrode sets. The capacitance change is then converted to the voltage by holding the principles of capacitive sensing methods in the read-out electronics. The converted-voltage is then utilized as the feedback voltage to recover the proof mass to its rest position by feeding it to the electrode sets in the closed-loop configuration. The closed-loop configuration of the read-out circuit will be explained briefly in Section 2.4.

2.3.2 Mechanical Design of the Sensing Element of MEMS Accelerometer

Mechanical design of the sensing element of MEMS accelerometer is based on the design of the proper spring and the proof mass structures. The spring structure is

designed such that it assures the single-axis acceleration sensing operation of the sensing element. The proof mass, on the other hand, is engineered such that the sensing element has high sensitivity in terms of the capacitance change under applied acceleration.

The proof mass of the sensing element consists of a few branches to which the finger structures are added. Figure 2.30 presents the schematic of the proof mass of the sensing element by showing the branches and the fingers on it. The branches are designed to prevent the buckling modes of the overall sensing element structure. The fingers are integrated to the branches of the proof mass to increase the capacitance between the proof mass and the electrodes. There are fingers also in the electrode sets, matching with the fingers on the proof mass to create capacitive gaps. The number of the fingers attached to the branches of the proof mass and the size of the proof mass branches are determined depending on the die area allocated for the sensing element of the accelerometer.

The calculation of the mass of the proof mass is held by considering the small holes on the branches of the proof mass. These holes decrease the mass of the proof mass structure and make it possible to use stiffer springs in the mechanical design of the sensing element of the accelerometer. The geometrical properties of the sensing element of the MEMS accelerometer used in this study can be found in Table 2.8.

The spring structure is selected to be the folded-beam spring structures. Four folded-beam spring structures are placed each corner of the proof mass such that the springs guarantee the single axis operation only, and avoid tilting of the proof mass under the effect of any acceleration. Figure 2.30 shows the schematic of the folded-beam spring structure on the layout of the designed MEMS accelerometer.

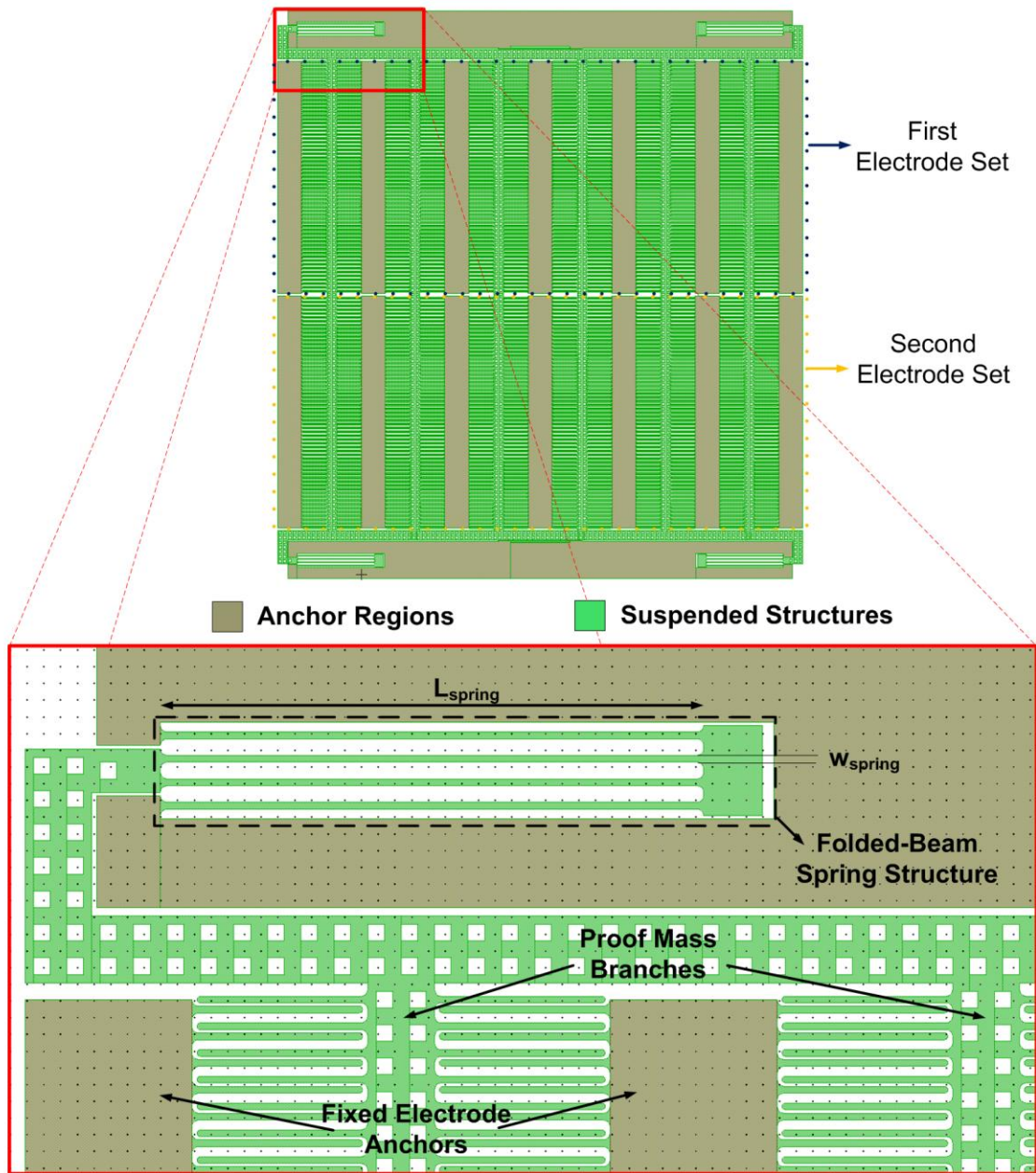


Figure 2.30: Layout of the sensing element of MEMS accelerometer with the zoomed-view of the folded-beam spring structures and the proof mass branches.

Table 2.8: Geometric properties of the MEMS accelerometer used in this study.

Quantity	Symbol	Value
Number of Fingers in one Electrode	n	732
Gap Between Two Consecutive Fingers	g	2 μm
Anti-Gap Between Two Consecutive Fingers	g_a	6 μm
Overlap Area of Two Consecutive Fingers	L	95 μm
Length of a Folded-Beam in Spring Structure	L_{spring}	325 μm
Width of a Folded-Beam in Spring Structure	w_{spring}	4 μm
Number of Springs	-	4
Structural Thickness	h	35 μm

The mechanical spring constant of a folded-leg spring structure can be calculated by using the formula below [37]:

$$k = \frac{2 E h w_{spring}^3}{L_{spring}^3} \quad (2.72)$$

The length of the beams in the spring structure is determined depending on the mass of the proof mass structure, since the resonance frequency of the fundamental modes of the sensing element structure is an important issue to be careful about in the use of the read-out electronic components. The mass of the proof mass structure and spring constant associated with the determined geometrical properties can be seen in Table 2.9.

The sensor characteristics such as rest capacitance and effective sensitivity of the sensing element can also be calculated by using the determined sensor dimensions. The rest capacitance is the capacitance formed between the proof mass structures and the electrode structures. The rest capacitance calculations as well as the sensitivity calculations should include the effect of both capacitive gap and anti-gap, which are illustrated in Figure 2.29. The rest capacitance can be calculated as follows:

$$C_r = \frac{\epsilon A_c}{g} + \frac{\epsilon A_c}{g_a} \quad (2.73)$$

Where the first term in the above equation belongs to the capacitance formed by the capacitive gap and the second term indicates the capacitance formed by the anti-gap side, while g denotes the capacitive gap and g_a denotes the anti-gap. A_c is the overlap

area covered by the fingers of the proof mass and the electrode set, ϵ denotes the permittivity of the filling material, vacuum in this case. The sensitivity of the sensing element can be calculated by taking the derivative of the rest capacitances of gap and anti-gap with respect to displacement, written as follows:

$$\frac{\partial C_r}{\partial x} = \frac{\epsilon A_c}{(g+x)^2} - \frac{\epsilon A_c}{(g_a-x)^2} \quad (2.74)$$

The equation (2.74) can be further simplified by neglecting the displacement since it is much smaller than the capacitive gap or anti-gap ($x \ll g$ and $x \ll g_a$) as follows:

$$\frac{\partial C_r}{\partial x} = \frac{\epsilon A_c}{g^2} - \frac{\epsilon A_c}{g_a^2} \quad (2.75)$$

Pull-in voltage for the sensing element of the MEMS accelerometer can also be calculated by using the formula presented in equation (2.27). All the sensor characteristic information can be found in Table 2.9.

Table 2.9: Sensor characteristics of the capacitive MEMS accelerometer used in this study.

Sensor Characteristics	Value
Mechanical Spring Constant (in total)	37.82 N/m
Electrostatic Spring Constant (for a single electrode)	2.23 N/m
Effective Spring Constant (in total)	33.36 N/m
Proof Mass	9.09×10^{-8} kg
Resonance Frequency of the Desired Operation Mode	3,049 Hz
Rest Capacitance (for a single electrode)	13.97 pF
Sensitivity ($\partial C/\partial x$) (for a single electrode)	4.09×10^{-6} F/m
Pull-in Voltage	2.95 V

2.3.3 FEM Simulations of MEMS Accelerometer

FEM simulations are held to create the 3d model of the sensing element and to examine some sensor characteristics. Modal simulations are performed to observe the first fundamental modes of the sensing element and to check the calculations presented in the previous section. The 3D model used in the simulations is again created by the process editor utilizing the mask layouts in GDS format. 3D model of the sensing element only

includes the proof mass, springs and the anchor regions. The fixed electrode sets were not included to the simulations.

2.3.3.1 Modal Simulations of the Sensing Element of MEMS Accelerometer

While performing the modal simulations, anchor regions are marked with the “fixall” command to define the boundary conditions of the sensing element. Modal simulation results can be found in Table 2.10 while the operation mode of the sensing element is presented in Figure 2.31.

Table 2.10: Modal simulation results of the sensing element of the accelerometer in all designs. The desired operation modes can be seen in the first 5 modes of the resonator system as labeled below.

Mode	Frequency (Hz)	Notes
1	3,518	Operation mode of the sensing element
2	9,703	
3	14,696	
4	19,131	
5	22,897	

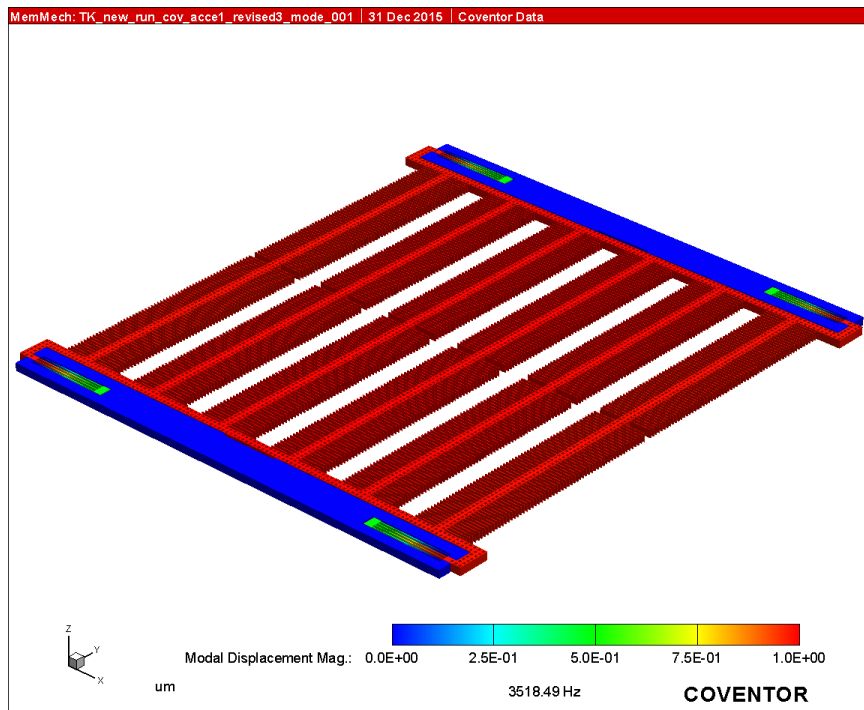


Figure 2.31: Modal simulation results obtained via CoventorWare for the sensing elements accelerometers.

The simulation results show that the desired operation mode for the single axis acceleration sensing is seen at 3.5 kHz which agrees with the calculations presented in Table 2.9. Although the other modes will not disturb the acceleration sensing operation unless a specific parasitic mode frequency is selected for the AC signal applied to the electrodes, these modes can be suppressed by means of the passive band-pass filters in analog read-out circuit.

2.4 Analog Force Feedback Read-out Circuit for the Sensing Element of MEMS Accelerometer

Analog read-out circuit used in this study as a part of MEMS accelerometer has been utilized in some applications [46, 50, 51], and explained in detail in [48]. The analog read-out circuit is mainly the part that makes the MEMS accelerometer operate in closed-loop configuration, and supplies acceleration-voltage conversion to be able to interpret the applied acceleration in terms of feedback voltage. The schematic of the read-out circuit can be seen in Figure 2.32.

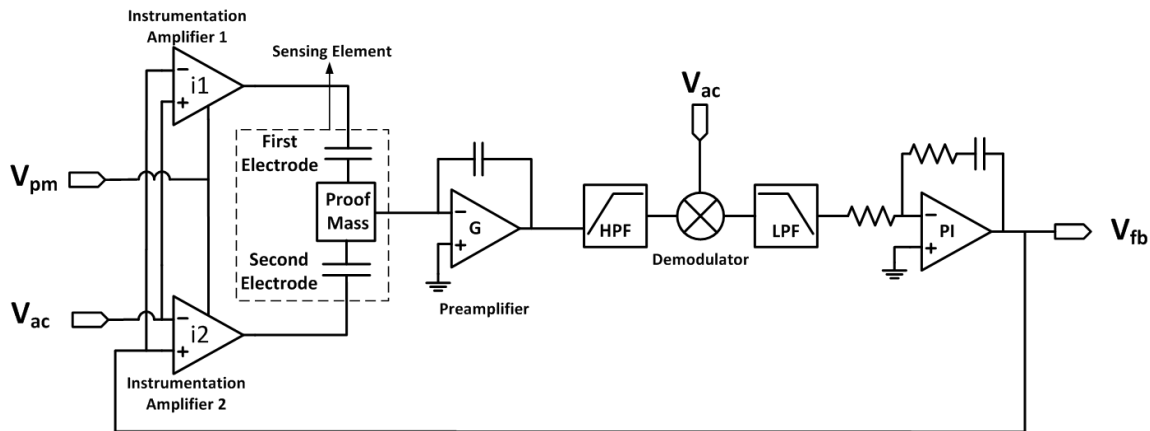


Figure 2.32: Schematic of the analog force-feedback read out circuit implemented to the MEMS accelerometer [51].

The proof mass of the sensing element is held in its rest position by applying the shown voltages, V_{pm} , V_{fb} and V_{ac} , to the electrode sets. V_{pm} is the DC voltage supplied to the both electrode sets by means of the instrumentation amplifiers in order to boost the electrostatic forces applied by the electrode sets. V_{fb} is the DC feedback voltage which is the final product of the read-out circuit to recover the proof mass to its original position

when the acceleration causes displacement to the proof mass of the sensing element. V_{ac} is the AC signal applied to both electrodes with different phases. The 180° phase difference between the V_{ac} voltages applied to the electrodes helps us distinguish the direction of the applied acceleration. When acceleration is exerted to the sensing element, the proof mass deflects under the control of the spring structures and the feedback voltages applied from the electrode sets. The deflection of the proof mass causes changes in the capacitance of two electrode sets inversely, i.e., if a capacitance of an electrode increases due to acceleration, the other has to decrease due to symmetrical placement of the electrode sets. These capacitance changes lead to a current flow through the proof mass structure as an AC signal. This AC signal enters the trans-impedance-amplifier (TIA) to be enhanced. Then, the output of the TIA is filtered through the high pass filter in order to remove the DC component of the AC signal. After that, the AC signal is modulated by the same carrier signal fed to the electrode sets, in order to get the rectified AC signal in the demodulator stage. This rectified AC signal is then converted to a DC signal by means of an active low pass filter. Then, this DC component is fed to the electrodes by the help of a PI controller, whose output is called as feedback voltage, V_{fb} . The necessary polarity of the feedback voltage fed to each electrode is provided by the instrumentation amplifier stages to be able recover the proof mass to its rest position. The relationship between the feedback voltage and the applied acceleration, called as scale factor of the accelerometer, can be found by writing the force equilibrium of the proof mass. While doing so, the electrostatic force applied to the proof mass by the electrodes should be considered:

$$m a = \frac{1}{2} \frac{\partial C}{\partial x} V^2 \quad (2.76)$$

Note that the spring restoration force is neglected since equilibrium condition is examined. By implementing the effective sensitivity and the voltage components to the equation:

$$m a = \frac{1}{2} \frac{\partial C_r}{\partial x} [(V_{PM} - V_{FB})^2 - (V_{PM} + V_{FB})^2] \quad (2.77)$$

$$m a = \frac{1}{2} \frac{\partial C_r}{\partial x} 2V_{PM} 2V_{FB} \quad (2.78)$$

$$SF = \frac{V_{FB}}{a} = \frac{m}{\frac{\partial C_r}{\partial x} 2V_{PM}} \quad (2.79)$$

The scale factor is estimated as 110 mV/g by using the sensor properties given in Table 2.9 and the above formula. Note that the proof mass voltage is taken as 1 Volt which will be the value used in the tests of the accelerometer. The theoretical calculation of the scale factor may deviate from the measurement results due to the undercut effects coming from the fabrication imperfections, which alters the sensitivity of the accelerometer significantly.

2.5 Temperature Effects on the Accelerometer Output

Temperature is a significant parameter affecting the operation of the accelerometer as a whole. The effects of temperature mainly are the result of change in material properties of the sensing element with altering temperature. The temperature change causes an alteration in the capacitive gaps between the fixed electrode structures and the proof mass structure due to expansion/contraction of the capacitive fingers and the proof mass structure itself. The mechanical spring structures, i.e., folded-beam spring structures for the accelerometer studied in this thesis, also show expansion/contraction with changing temperature, which also influence the dynamics of the proof mass structure as stated in [52]. Additionally, stress induced on the sensing element structure [53] due to different thermal expansion coefficients of the substrate and the sensor structure materials may disturb the balance of the proof mass, which is provided by the analog force-feedback read-out circuit. All the changes mentioned above lead to a drift in the feedback voltage of the read-out circuit, i.e., the output of the accelerometer. As a result, a phantom acceleration appears in the accelerometer output due to temperature change. The reasons of the drift in the accelerometer under changing temperature are not included to the scope of the thesis, therefore the one who wants further information can look-up the references given in this thesis [52, 54].

2.6 Summary

This chapter has introduced the design details of the MEMS resonators and MEMS accelerometers used in this thesis study. The operation principles of MEMS resonators

as temperature sensors and operation principles of MEMS accelerometers are explained in detail. The FEM simulation results are presented to verify the analytical models exhibited in separated sections. In addition to the operation principles and mechanical design procedures, the electronic read-out circuit of MEMS resonators is explained in detail while the electronic read-out circuit of MEMS accelerometer is mentioned briefly. The geometric properties of the sensors, FEM simulation results and sensor specifications are also presented in the related sections of this chapter.

CHAPTER 3

FABRICATION OF MEMS DETF RESONATORS AND ACCELEROMETERS

In this chapter, the fabrication processes of the MEMS resonators and MEMS accelerometers whose design procedures have been explained in Chapter 2 will be explained step-by-step. This chapter is divided into three sub-divisions. First, the formation of whole sensor structures will be presented with the supplementary figures for better visualization. Second, the cap wafer process which provides the vacuum environment for the sensor structures will be unveiled. Third, the fabrication results will be exhibited with the help of SEM images of the fabricated sensor dies. Finally, the chapter will be summed up in Summary section.

The fabrication steps are comprised of a modified silicon-on-glass (SOG) method for the formation of the sensor structures [55], and wafer-level hermetic encapsulation process provided by a silicon-on-insulator (SOI) cap wafer [56]. The wafer fabricated via SOG process and the SOI cap wafer are bonded to each other by means of anodic bonding so as to obtain the final sensor die. This whole process is called as advanced MEMS or most commonly aMEMS process in METU-MEMS Research and Application Center [38]. As the fabrication steps of aMEMS process are examined and presented in detail in [38, 57], the brief explanations will be used to explain the key points in the fabrication in this chapter.

3.1 Fabrication of Sensor Structures

Figure 3.1 illustrates the cross sectional view of the prepared sensor wafer after each step through (a)-(h). Fabrication of sensor structures is basically an SOG process achieved by anodic bonding of a glass substrate wafer and an SOI wafer whose device layer was patterned with respect to the sensor structure. Then, by removing the handle layer and buried oxide layers of the SOI wafer, the sensor structures are formed.

The fabrication of sensor structures start with the fabrication of the substrate wafer which is a plain glass wafer (Figure 3.1 (a)). On this plain glass wafer, the anchors are formed so that the suspended structures of the resonators and accelerometers can be connected to the substrate. The anchor formation is held by etching the glass wafer in hydrofluoric acid, HF, solution. A chromium (Cr) / gold (Au) mask is utilized in this step to cover the anchor regions. Hence, as a first step, the plain glass wafer is covered with Cr/Au layers to create the Cr/Au mask. Cr layer is used as a adhesion layer between the Au layer and the glass wafer. The patterning of these Cr/Au layers is achieved after successive wet etching processes of Au and Cr layers. When the Cr/Au mask becomes ready, the anchors are formed on the glass wafer in HF solution. After anchor formation process, the Cr/Au mask is stripped (Figure 3.1 (b)). As second step, the electrical connections of the sensor structures including the metallization lines from sensor parts to the pads are built on the glass wafer. The metal lines are again comprised of Cr/Au layers coated via thermal evaporation process. The coated Cr/Au layer is again patterned by lithography and wet etching processes. With this process, the glass wafer on which the anchors and the metal lines are formed becomes ready as a substrate to the sensor structures (Figure 3.1 (c)).

The sensor structures are built on the device layer of an SOI wafer as mentioned earlier (Figure 3.1 (d)). Before creating the sensor structures on the SOI wafer, a shallow etch process is needed in order to protect some regions such as pad regions, bond ring of the cap wafers etc. that are not supposed to bond to glass substrate in anodic bonding. The shallow etch process is performed by means of deep-reactive-ion-etching (DRIE) process by thinning the device layer of the SOI wafer (Figure 3.1 (e)). After the shallow etch process, the structures of the resonators and the accelerometers are formed on the

device layer of the SOI wafer via DRIE tool. Again, a lithography process is performed in order to create the structure mask on the device layer of the SOI wafer (Figure 3.1 (f)). When the sensor structures are formed on the SOI wafer, anodic bonding step is held to bond the glass substrate and the sensor structures formed on the SOI wafer (Figure 3.1 (g)). Before anodic bonding, both SOI wafer and the glass wafer are cleaned in piranha solution ($\text{H}_2\text{SO}_4\text{-H}_2\text{O}_2$, 1:1). After anodic bonding step, the handle layer of the SOI wafer is removed by DRIE. Then, as a final step, the buried oxide layer is removed in buffered HF (BHF (1:7)) solution in order to release the suspended sensor structures (Figure 3.1 (h)). With this process, the fabrication of the sensor structures is finalized. The sensor wafer where the sensor structures bonded to the glass substrate is then bonded to the cap wafer for the hermetic encapsulation process.

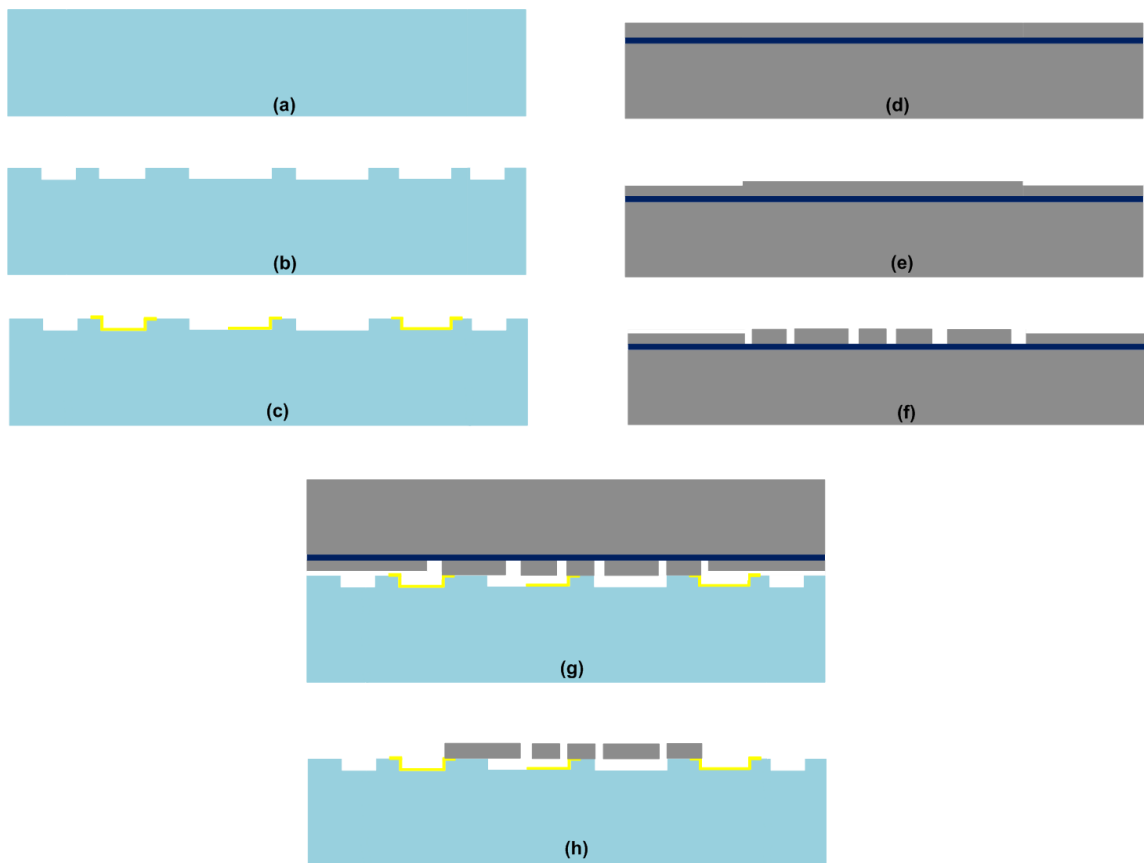


Figure 3.1: Process flow of the sensor wafer fabrication in aMEMS1 process over the cross-sectional views of the wafers.

3.2 Fabrication of Cap Wafer for Hermetic Encapsulation

The process flow of the cap wafer and the final bonding are illustrated in Figure 3.2 by means of the cross-sectional view of the wafers after each step. Wafer level vacuum packaging process in aMEMS process ensures the vacuum environment for the MEMS resonators and accelerometers that is needed for more robust operation of these sensors. The vacuum packaging is acquired with the bonding of an SOI cap wafer and the glass substrate on which the sensor structures are built. On the device layer side of the cap SOI, the wells for the vertical feedthroughs are created by using oxide mask as a protection layer in potassium hydroxide (KOH) solution (Figure 3.2 (a)). After the KOH etches the device layer till the buried oxide of the cap SOI, the buried oxide openings are etched in BHF solution, to supply contact with the vertical feedthroughs. The openings on the oxide layer are then filled with the Cr/Au layers by utilizing a lift-off process (Figure 3.2 (b)). The created Au pads are then facilitated by means of wire-bonds during testing of the sensors.

The electrical connections of the sensors are delivered outside of the sensor die by means of vertical feedthroughs via columns [58]. On handle layer side of the SOI wafer, the vertical feedthroughs are formed to transmit the electrical connections of the sensor structures aligned to the pads on the glass substrate. Additionally, the sensor cavity is opened on the handle layer side of the SOI via DRIE process (Figure 3.2 (c)). Inside this sensor cavity, getter material is deposited by using sputtering tools in order to absorb the remaining gas molecules inside the die after bonding (Figure 3.2 (d)). Further details related with the cap wafer process can found in [38].

The prepared cap wafer and the glass substrate on which the sensor structures are formed earlier are bonded to each other by using anodic bonding. This anodic bonding process is the last step of the fabrication of wafer-level-vacuum-packaged MEMS resonators and accelerometers. The process flow of the cap wafer and the final bonding are illustrated in Figure 3.2 by means of the cross-sectional view of the wafers after each step. Figure 3.3 presents the 3D model of a sensor die for better visualization of how the signal is transmitted inside the sensor die.

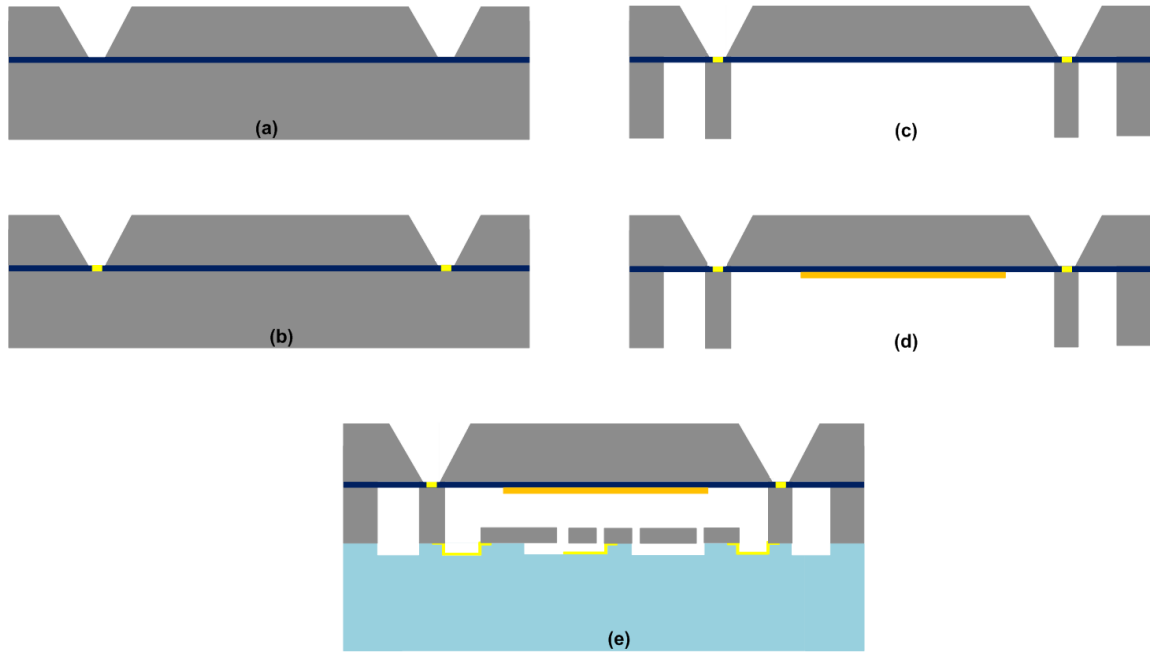


Figure 3.2: (a-d) Process flow of the cap wafer fabrication in a MEMS1 process over the cross-sectional views of the wafers. e) Cross-sectional view of the sensor die after anodic bonding of the sensor and cap wafers.

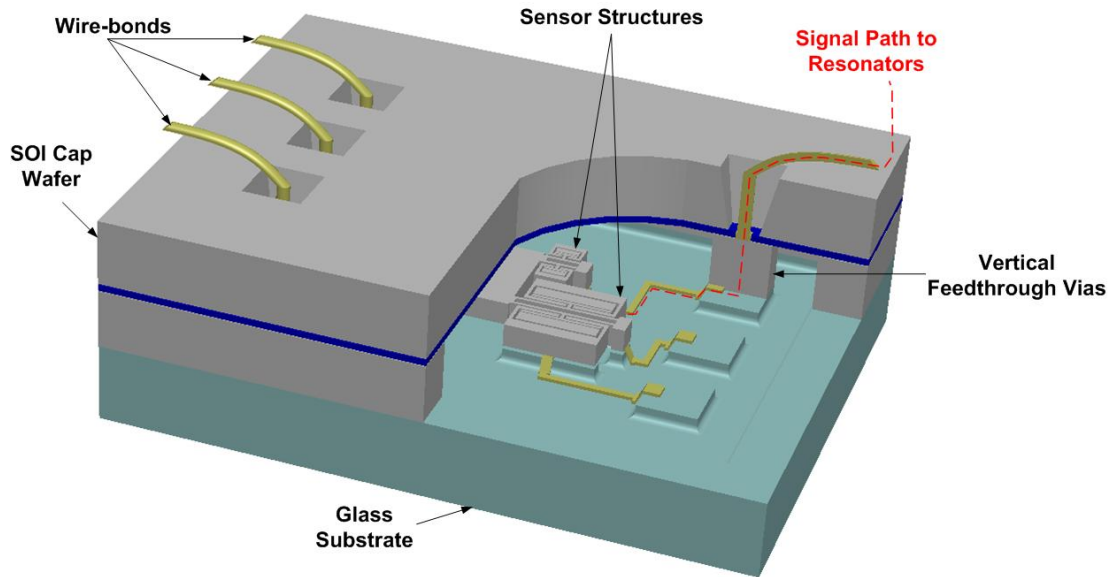


Figure 3.3: 3D model of the fabricated sensor chip used in this study.

3.3 Fabrication Results

After the fabrication has finished, SEM images of the fabricated sensor dies are captured in METU-MEMS Research and Application Center in order to check the critical dimensions of the sensor structures. The most common fabrication error faced after fabrication is the undercuts. Hence, it is expected that some undercuts may occur in the sensor structures that may result due to wet etch processes or lithography steps performed, or different-sized gap openings etched via DRIE. The undercut appeared on the tines of the resonators or the springs of the accelerometers leads to a change in resonance frequency of the related parts on account of the change in the stiffness of the related members. The undercut amount can be detected via SEM images of the sensor parts as seen in Figure 3.5 below.

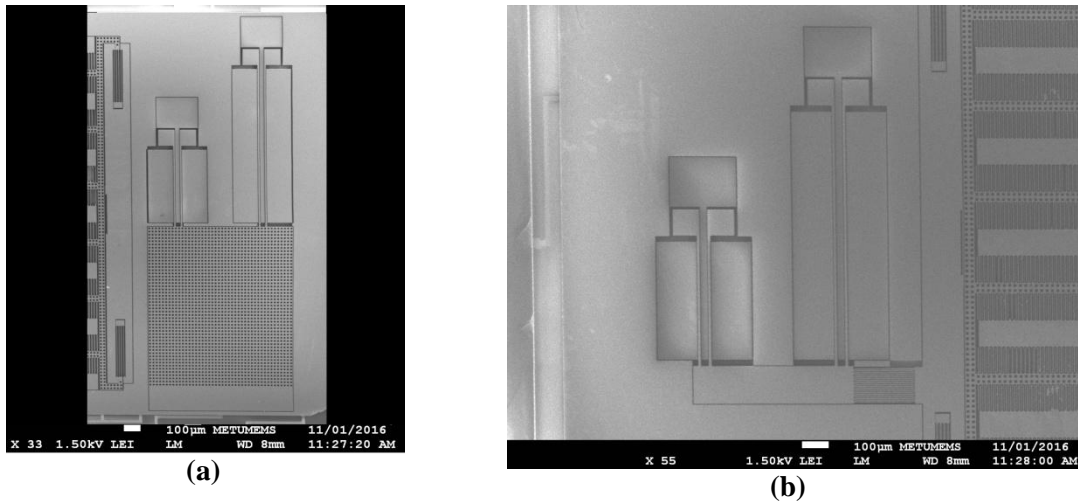


Figure 3.4: *a) SEM images of the fabricated long and short DETF resonators in Design 1A. SEM images of the on-chip integrated DETF resonators (on the right) and a part of the capacitive accelerometer to be temperature-compensated (on the left). b) SEM images of the fabricated DETF resonators belonging to Design 1C. SEM images of the on-chip integrated DETF resonators (on the left) and a part of the capacitive accelerometer to be temperature-compensated (on the right).*

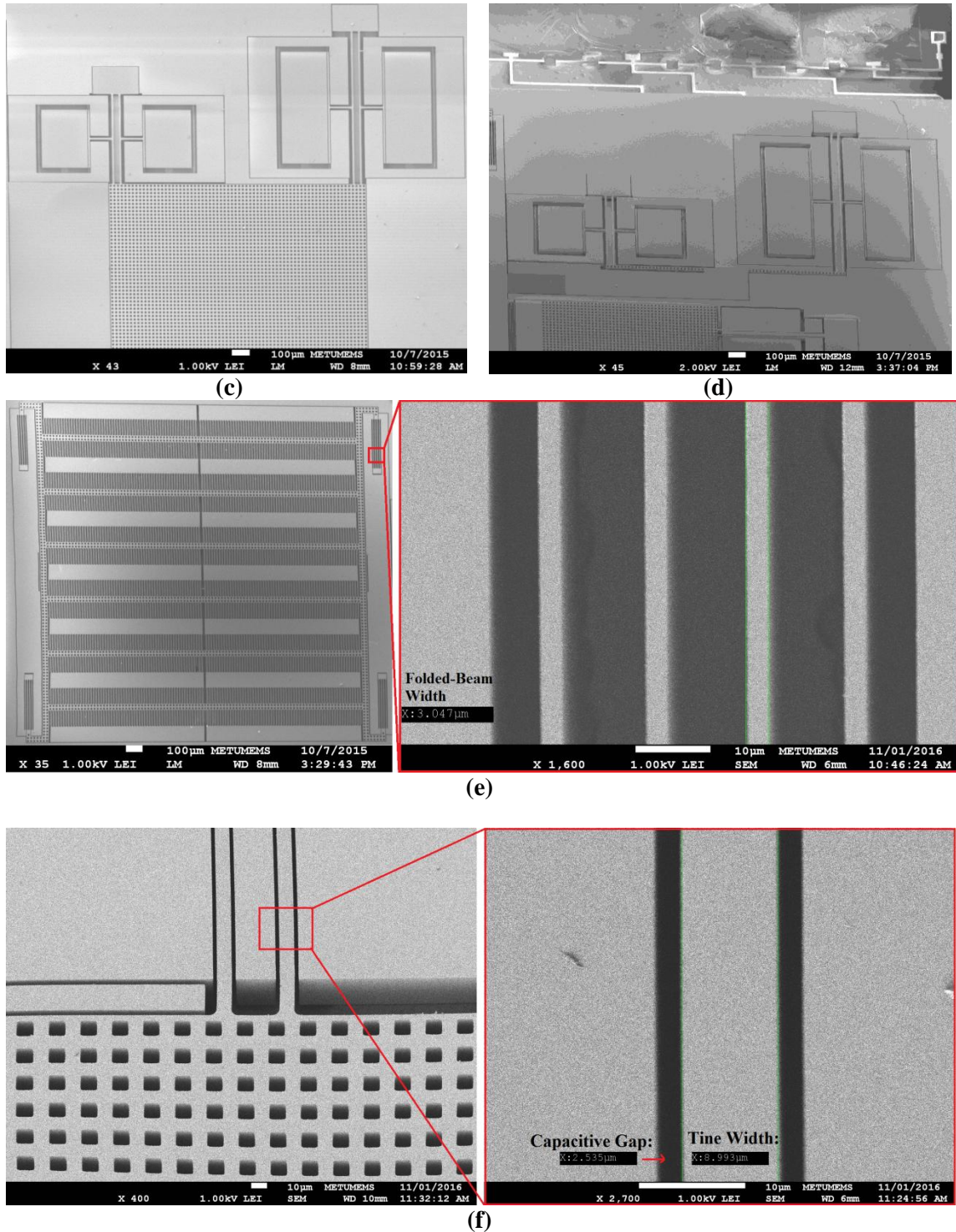


Figure 3.5 (continued): *c) SEM images of the fabricated long and short DETF resonators in Design 2A. d) SEM images of the fabricated DETF resonators belonging to Design 2B. e) SEM images of the fabricated MEMS accelerometer together with the zoomed-view showing $\sim 1 \mu\text{m}$ undercut is observed on the width of the folded-beam springs. f) SEM images of the fabricated DETF resonator together with the zoomed-view showing $\sim 1 \mu\text{m}$ undercut is observed on the width of the tine, and $\sim 0.5 \mu\text{m}$ undercut for the capacitive gaps is observed.*

Since the undercuts are inevitable in the fabrication process, the sensor structures are supposed to be designed by considering the effects of the undercuts. As the small changes in resonance frequency does not affect the sensitivity of the designed resonators or accelerometers, the sensors are quite alright to be used in the tests.

In addition to the undercuts, there may exist contamination on the sensor structure coming from the fabrication steps due to sloppy use of clean-room tools. This type of contamination was monitored during the fabrication steps, and necessary actions were taken during the fabrication. Fortunately, no excess contamination is observed during the fabrication of the sensors.

3.4 Summary

In this chapter, fabrication processes that MEMS resonators and accelerometers used in this study underwent are described briefly with the help of illustrative figures starting from the fabrication of the sensor structures to the cap wafers. Fabricated sensors are also presented by SEM images, and fabrication results are discussed.

CHAPTER 4

TESTS AND MEASUREMENT RESULTS

This chapter describes the testing procedures and equipments of MEMS DETF resonators and accelerometers, and presents the measurement results of the tests obtained from these sensors. System-level temperature tests in which the MEMS DETF resonators and accelerometers are operated simultaneously inside a temperature-controlled oven are the main focus in this chapter although characterization tests are presented on the fabricated sensors before proceeding to the system-level temperature tests. Section 4.1 depicts the characterization tests of MEMS DETF resonators and MEMS accelerometers while Section 4.2 introduces the test setup for temperature tests of the fabricated sensors by explaining the preparation of sensor package, preparation of analog read-out package of the accelerometer, preparation of printed-circuit board (PCB) on which the sensor package and the accelerometer read-out package, and the overall test setup conducted in the temperature-controlled oven. Afterwards, Section 4.3 presents the measurement results obtained from the system-level temperature tests together with the temperature compensation results of MEMS accelerometers. Finally, Summary and Conclusions part in Section 4.4 presents the overview of the chapter and conclusions reached in this chapter.

4.1 Characterization Tests

The characterization tests are performed in order to see whether the fabricated sensors function properly or not. The characterization tests consist of the resonance tests for the

MEMS DETF resonators, and CV tests for the MEMS accelerometers. Hence, firstly, the resonance test results of DETF resonators will be presented in Section 4.1.1, and secondly, the CV test results of the MEMS accelerometers will be introduced in Section 4.1.2.

4.1.1 Characterization Test Results of MEMS Resonators

Characterization tests of MEMS resonators used in this study include the resonance test of the resonators by using Agilent 4395A Network Spectrum Analyzer, and probe station available in Electrical and Electronics Department, METU. Figure 4.1 illustrates the characterization test setup for the MEMS DETF resonators.

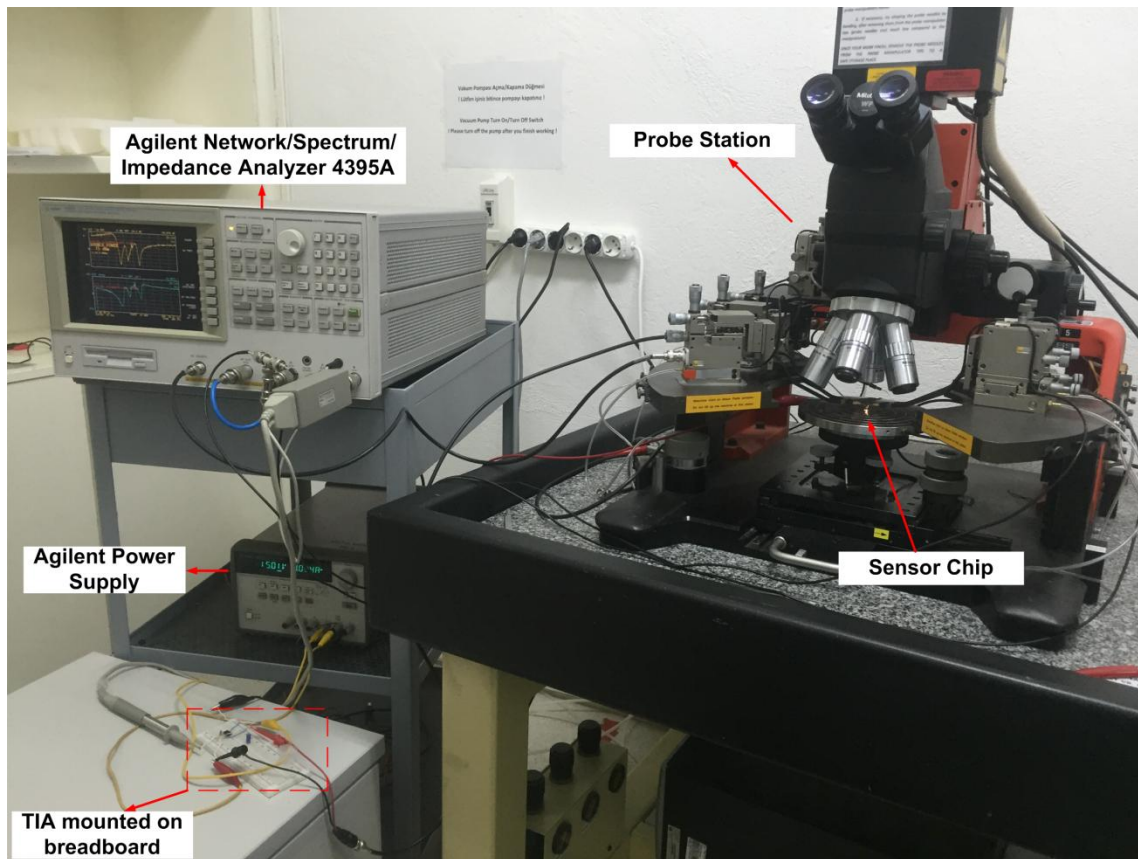


Figure 4.1: Photo of the characterization test setup prepared for the functionality tests of fabricated MEMS DETF resonators.

The probe station is utilized in the characterization tests of the DETF resonators in order to provide connections to the resonator components while the TIA (LF353) is mounted

on a breadboard as shown in the figure above. An Agilent power supply is used to feed the supply voltages of TIA.

The resonance tests indicate the functionality of the fabricated resonators die as well as the vacuum level inside the sensor. The vacuum level inside the sensor die can be estimated from the quality factor calculations. The resonance tests for the resonators are held by using only a resistive TIA with a 900 k Ω resistor. The proof mass voltage supplied to both long and short resonators is selected to be between 10 Volts and 40 Volts depending on the resonator type, and amplitude of AC signal fed to the drive electrode is chosen to be between 20-200 mV (peak-to-peak). The collected data are transferred via a GPIB cable and an add-on installed to MS Excel. Collected data are processed in MS Excel environment in order to obtain the pure mechanical resonance of the resonators. That achieved by collecting the stray data while the proof mass voltage turned off. The stray data are then subtracted from the original resonance data. Figure 4.2 presents the processed mechanical resonance data of DETF resonators. Table 4.1 presents the resonance test results together with the significant test configurations.

Table 4.1 presents the resonance frequency and quality factor data for the related proof mass voltage, belonging to the out-of-phase operation mode of the DETF resonators, since it has higher peak magnitude, which leads the self-resonance circuits to lock on that frequency. The calculated quality factors indicate the pressure level inside the sensor dies which are in between 10 mTorr and 100 mTorr [57].

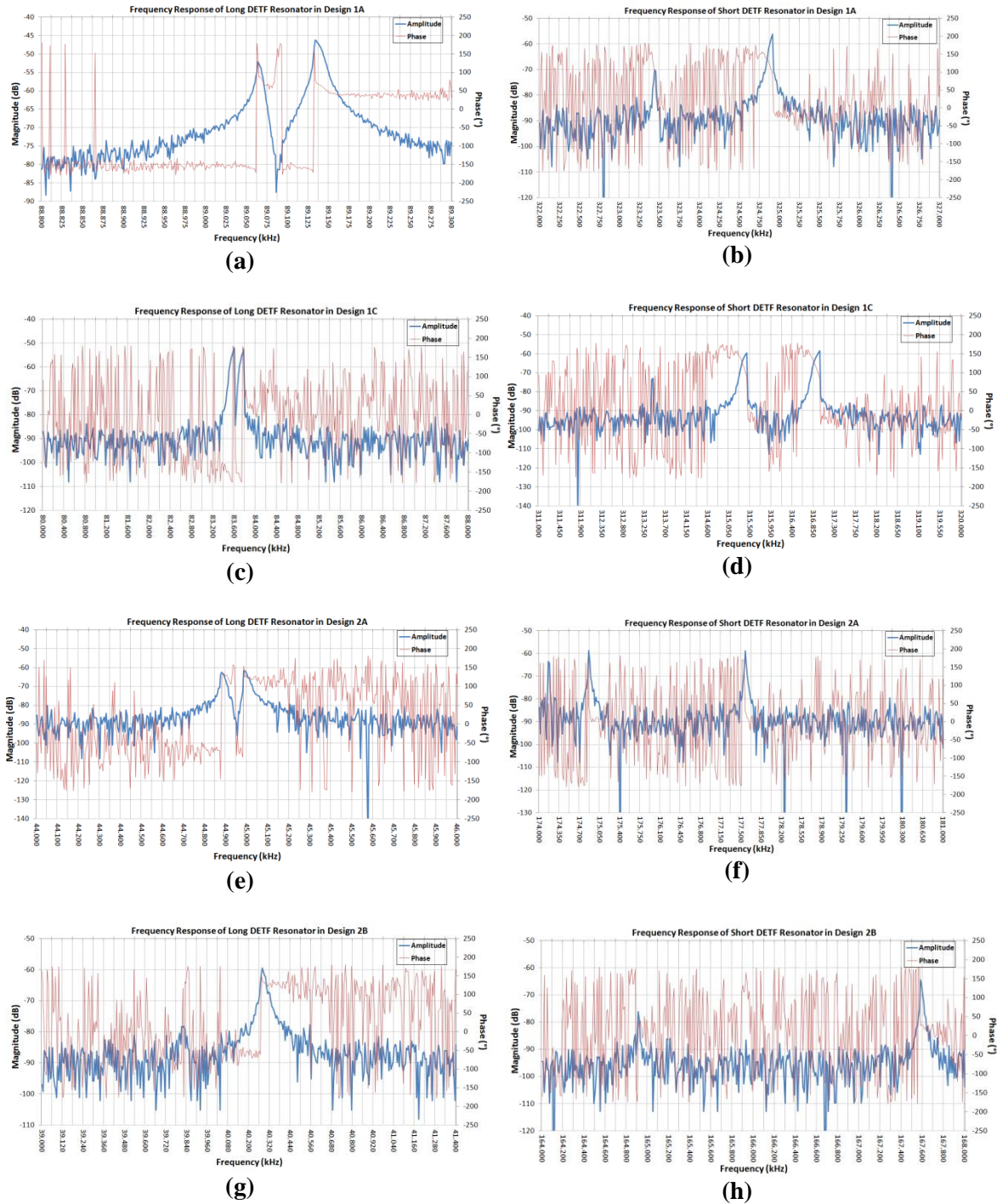


Figure 4.2: Characterization test results of the fabricated DETF resonators belonging to **a)** Long DETF resonator present in Design 1A, **b)** Short DETF resonator present in Design 1A, **c)** Long DETF resonator present in Design 1C, **d)** Short DETF resonator present in Design 1C, **e)** Long DETF resonator present in Design 2A, **f)** Short DETF resonator present in Design 2A, **g)** Long DETF resonator present in Design 2B and **h)** Short DETF resonator present in Design 2B.

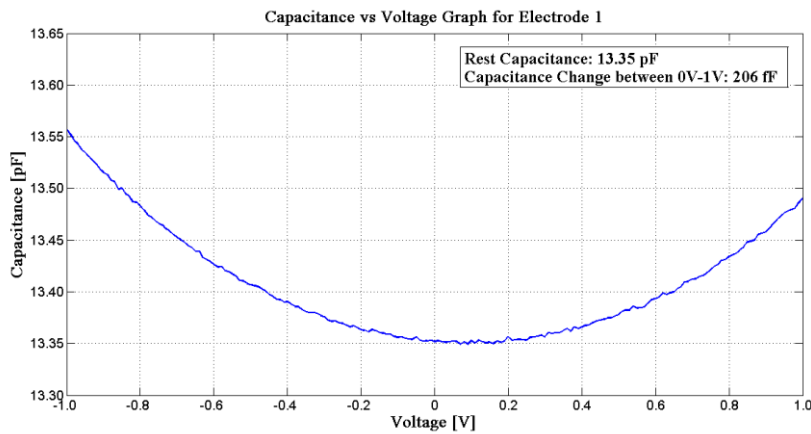
Table 4.1: Results of the characterization tests of MEMS DETF resonators.

Quantity	Design 1A		Design 1C		Design 2A		Design 2B	
	Short DETF	Long DETF	Short DETF	Long DETF	Short DETF	Long DETF	Short DETF	Long DETF
Resonance Frequency	324,910 Hz	89,140 Hz	316,920 Hz	83,525 Hz	177,610 Hz	45,020 Hz	167,680 Hz	40,270 Hz
Proof Mass Voltage	40 V	15 V	40 V	10 V	20 V	12 V	20 V	10 V
Quality Factor	32,996	25,914	35,778	25,345	16,023	13,201	16,758	14,030

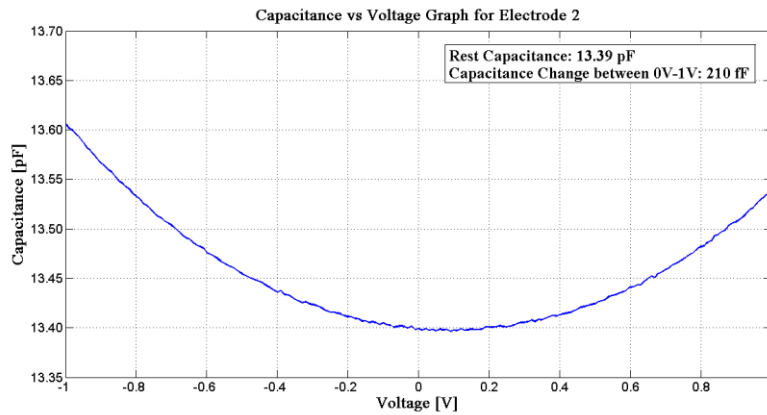
The nonlinearities in the frequency responses of some DETF resonators such as long DETF resonator in Design 1A and long DETF resonators in Design 2A, i.e., the tendency to the lower frequency in the peak magnitude, called “duffing”, are the result of non-linear electrostatic spring constant effect due to large proof mass voltage [19]. The large proof mass voltages increase the effects of nonlinear electrostatic spring constant terms, which reduce the effective spring constant, and hence create a tendency to lower frequencies. The solution to prevent this type of nonlinearities is lowering the proof mass voltage to suppress the effects of the nonlinear electrostatic spring constant terms. In the similar manner, the nonlinearities seen in the frequency response of the long and short DETF resonators in Design 1C are the outcome of the nonlinear mechanical spring constant terms, which try to increase the effective spring constant of the tines as mentioned in Chapter 2. The doubly-clamped DETF resonator type fosters the tensile stress on the tines while in resonance mode of the tine [19]. That’s an example of it. Lowering the AC signal fed to the drive electrodes can be the solution for this type of nonlinearities since it will reduce the magnitude of the deflection. The configurations that prevent these nonlinearities will be utilized in the system-level tests, i.e., proof mass voltage of 10 Volts and drive signal of 20 mV for the long resonators and 100 mV for the short resonators.

4.1.2 Characterization Test Results of MEMS Accelerometers

Characterization tests for the MEMS accelerometers are comprised of CV tests which indicate how the capacitances of the electrodes of accelerometer change with the applied DC voltages. CV tests also show the rest capacitance of the electrodes from which the parasitic capacitances can be estimated by comparing the theoretical calculations with the CV test results. Figure 4.3 illustrates CV test results of the accelerometer present in Design 1C die. Again, it should be noted that CV test results of other MEMS accelerometers present in the used dies will not be given in separate figures here since they have pretty much the same results. Table 4.2 illustrates the CV test results of MEMS accelerometers used in this study.



(a)



(b)

Figure 4.3: CV test results of the MEMS accelerometer in Design 1C.

Table 4.2: Summary of the CV test results of the MEMS accelerometers used in this thesis study.

Accelerometer Type	Electrode 1		Electrode 2	
	Rest Capacitance [pF]	Capacitance Change [fF] (between 1V-0V)	Rest Capacitance [pF]	Capacitance Change [fF] (between 1V-0V)
Accelerometer 1A	13.25	189	13.37	195
Accelerometer 1C	13.35	206	13.39	210
Accelerometer 2A	13.27	193	13.35	198
Accelerometer 2B	13.75	200	13.89	217

Although it is expected to have a symmetric plot of capacitance change with respect to positive and negative DC voltages, the asymmetric plots are observed as seen in Figure 4.3. The reason behind that asymmetry is probably the charging effects of the glass substrate. The rest capacitance values of the accelerometer electrodes are around 13.5 pF which agrees with the estimated capacitance value which is 13.97 pF presented in Chapter 2. The reason behind that 0.5 pF difference between the test and theoretical results of the capacitances is the inevitable fabrication imperfections such as undercut of the finger structures. Hence, the results show that the accelerometers are ready for the system-level tests.

4.2 Test Setup Preparation for the System-Level Temperature Tests

System-level temperature tests where MEMS resonators and accelerometer are operated concurrently, include many components, namely: the sensor package, the accelerometer read-out package, the test PCB where the sensor package and read-out circuits are mounted, and placed inside the temperature-controlled oven, power supplies, function generators and multi-meters placed outside the temperature-controlled oven, etc. In this section, first, the package preparations i.e. sensor package preparation and accelerometer read-out package preparation, will be explained. Then, the test PCB design and overall test setup will be demonstrated.

4.2.1 Preparation of Sensor Package

Sensor package is a Schott™ 16-pin gold-based package with its silver cap which is used as Faraday Cage. A glass PCB placed inside this package is utilized as a base on which the surface-mount read-out components are mounted. The glass board is also fabricated in METU-MEMS Research and Application Center utilizing thermal evaporator system to form gold (Au) lines on it. Gold-lines are patterned on the glass board with respect to the arrangements of the read-out components. Figure 4.4 presents the overview of the sensor package prepared for the system-level tests.

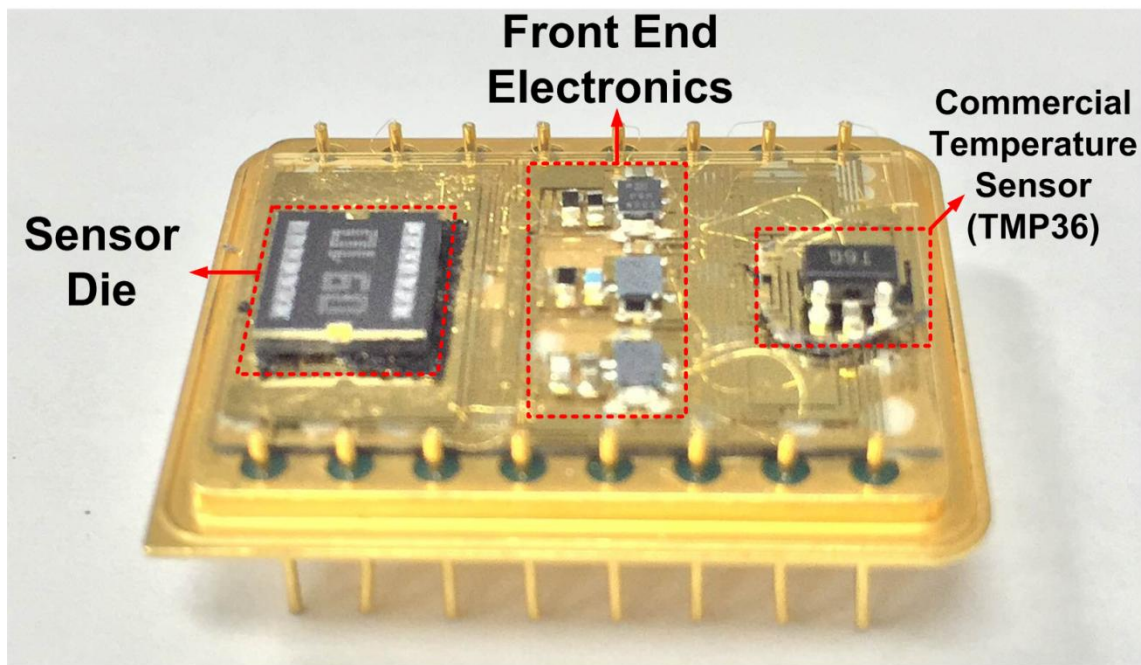


Figure 4.4: Overview of the sensor package employed throughout the system-level tests.

The glass board is then placed over the base of the sensor package by means of silver epoxy. After the glass base is successfully placed on the package, the front-end electronic components, i.e. preamplifiers of the resonators and accelerometer (AD8606), are mounted on the glass base by using pick-and-place tool available in METU-MEMS Research and Application Center. To guarantee the robustness of the components placed on the glass base, solder paste is preferred as the glue between the gold lines and the component legs. Some additional electrical connections of the components placed on the glass base are achieved through the wire-bonds. The fabricated sensor die containing the accelerometer and the resonators is placed on the glass base by means of carbon tape so

that the sensor die can be replaced easily to utilize other dies by using the same package. A commercial temperature sensor, TMP36, is placed on the glass base to be able to monitor the temperature inside the package. Although it is known that this sensor does not provide the exact temperature of the sensor die, it is used to have an idea about the approximate temperature inside the package.

4.2.2 Preparation of Analog Force-Feedback Read-Out Package for Accelerometer

The analog force feedback read-out circuit introduced in Section 2.4, is used for the single-axis MEMS accelerometer utilized in this thesis. Figure 2.32 shows the schematic of the read-out circuit utilized to operate the accelerometer. The read-out circuit is fitted inside a 16-pin SchottTM package same as the sensor package. Similarly, a glass PCB on which the Au lines are formed is utilized to provide the electrical connections between the circuit components.

Wire-bond connections are also set where necessary on the glass board to complete the circuit connections. The pick-and-place tool is benefited for mounting of the surface-mount read-out components on the glass board as it did in sensor package preparation. Figure 4.5 presents the overview of the analog-force-feedback read-out package for accelerometer used in the tests.

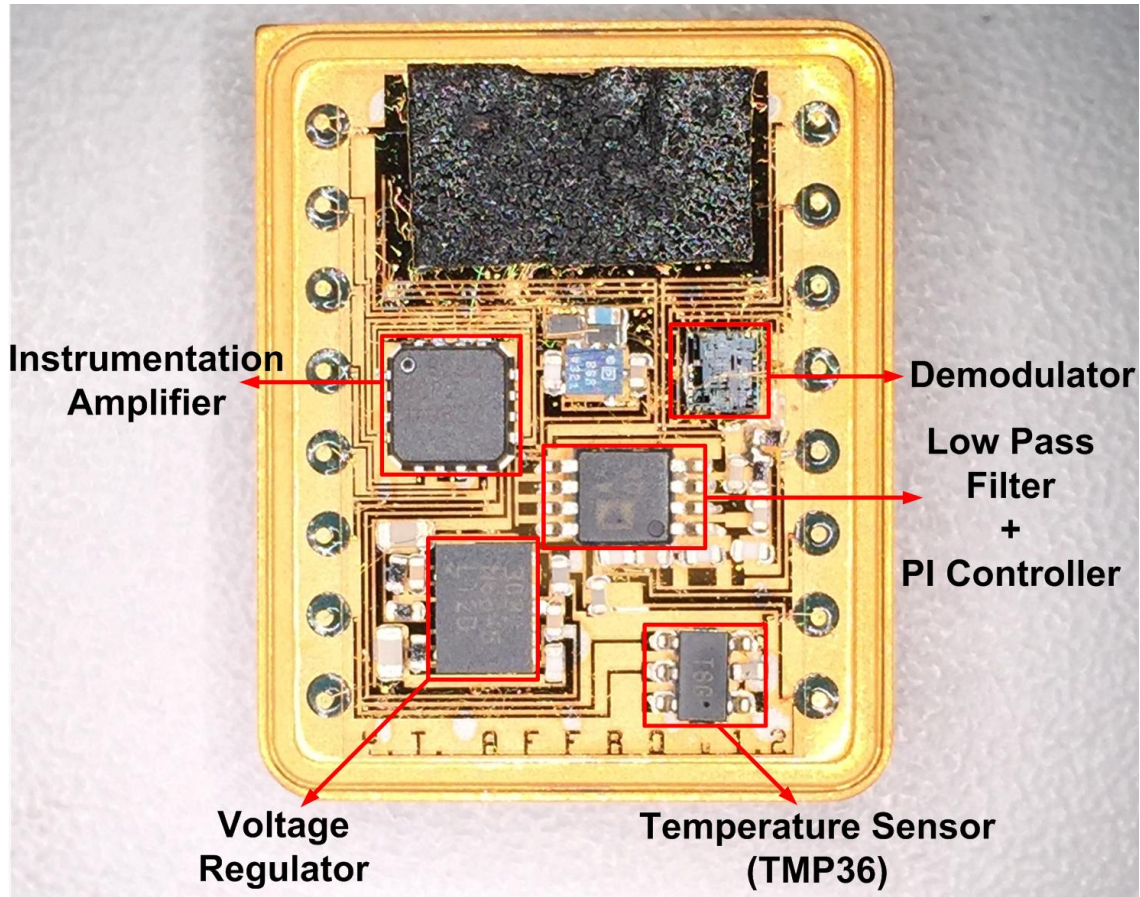


Figure 4.5: Overview of the readout package [48] for the system-level tests of MEMS accelerometers. Note that there are only the readout components in this package while the sensor chip is placed inside the sensor package presented in Figure 4.4.

After preparation of the package, the preliminary functionality tests are handled to test each component in the read-out circuit before proceeding to the system-level tests. These preliminary tests are mentioned in [48] if one needs further information.

4.2.3 Preparation of Test PCB

Simultaneous operation of MEMS accelerometer and MEMS resonators requires a platform to integrate the read-out circuits of all sensors in a compact way. The test printed-circuit-board (PCB) is designed to fulfill this requirement for easy-handling of test setup. All read-out components of both resonators and accelerometer and sensor packages are mounted on this PCB. Since the read-out circuit of the accelerometer can be placed inside a 16-pin package, only electrical connections between the sensor

package and the accelerometer read-out package are set while implementing the accelerometer related read-out components. However, since there is no package for the read-out circuits of the resonators, the components of the read-out circuit of the resonators are placed on the PCB. Figure 2.20 illustrates the schematic of the read-out circuit of the resonators. Figure 4.6 shows the overview of the PCB designed on Eagle Software.

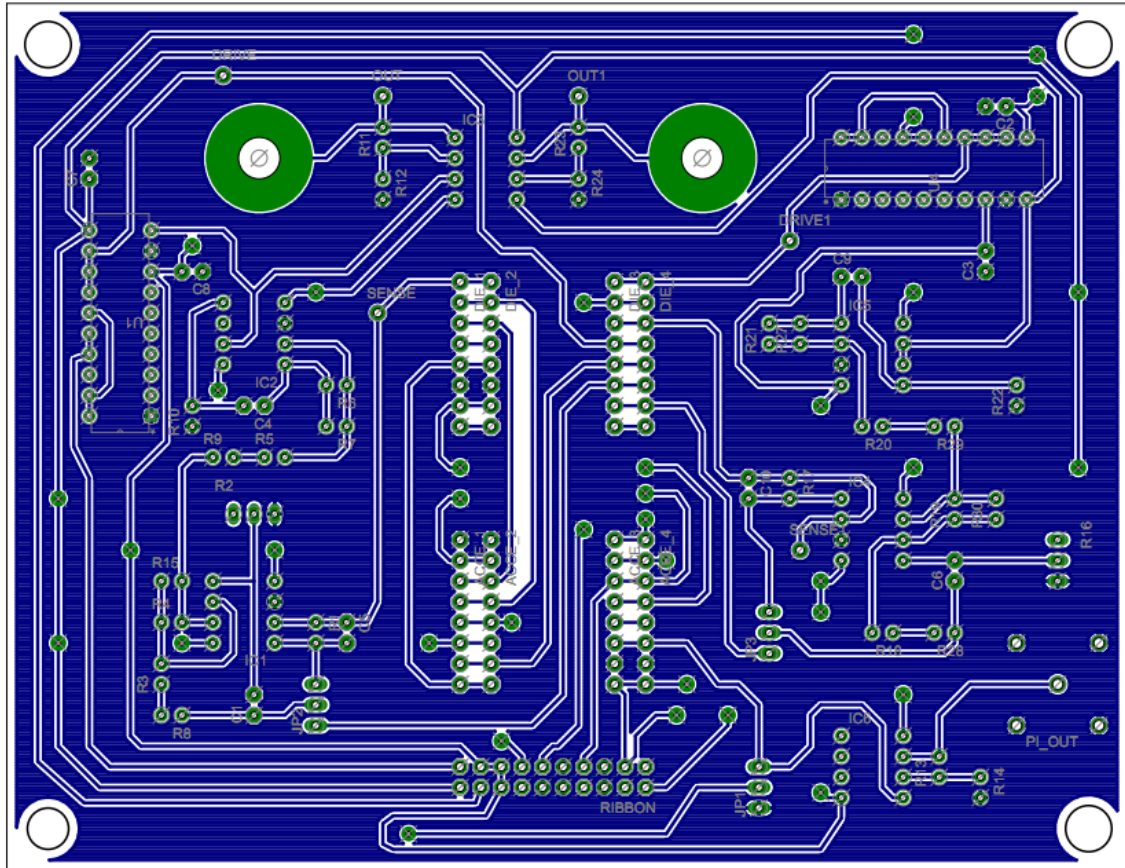


Figure 4.6: Layout of the test PCB prepared via Eagle software. Note that the test PCB is designed as one-sided PCB, and the connections showed in this figure processed the bottom side of fabricated test PCB.

While designing the PCB, only one-side of the PCB is used since there are no complex wirings. Besides, that would provide an ease of fabrication. A prototype of test PCB is fabricated in METU Ayasli Center by using LPKF tool. After necessary soldering is done, the PCB becomes ready to use in the tests. Figure 4.7 presents the overview of the prototype PCB on which the read-out circuit components and sensor packages are mounted.

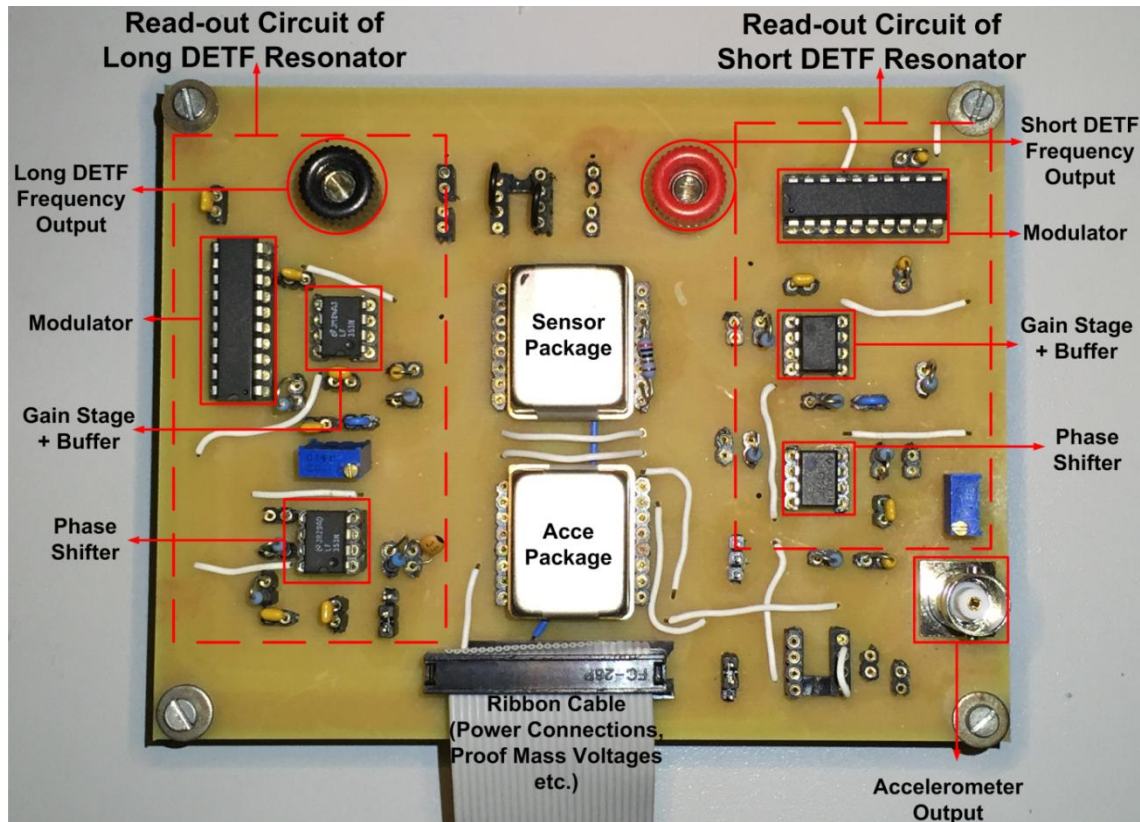


Figure 4.7: Overview of the fabricated prototype test PCB.

The test PCB shown in Figure 4.7 is used for testing of all resonators presented in Chapter 2, hence, PCB should be configurable depending on the resonator type used in the tests. In order to ease the change of certain circuit components, female headers are utilized to create places for each read-out circuit component. These headers allow easy plugging in and out the circuit components.

4.2.4 Implementation of Test Setup for the System-Level Tests

The system-level tests are held by utilizing the temperature-controlled oven while test PCB is placed inside the oven. The electrical connections of the test PCB are supplied into the oven via ribbon cable, BNC cables and banana-type cables depending on the signal passing through the cable. Non-critical connections such as power connections, ground, or DC voltages are carried by means of ribbon cable, while the output of the accelerometer is carried along the BNC cable. The outputs of the self-resonance loop of resonators are carried via banana cables. The same outputs are fed to two separate

Agilent 6-digit Multimeters for each resonator. Frequency data are then collected by using Agilent BenchVue software. The output of the accelerometer is fed to the data acquisition computer, and accelerometer output data are collected via this computer. The output of the commercial temperature sensor, TMP36 that is placed inside the sensor package, is also connected to the other input channel of the same DAQ computer. The data acquisition of accelerometer output and TMP36 sensor output is achieved by LabView software. Figure 4.8 shows the picture of the test setup by showing the test equipments.

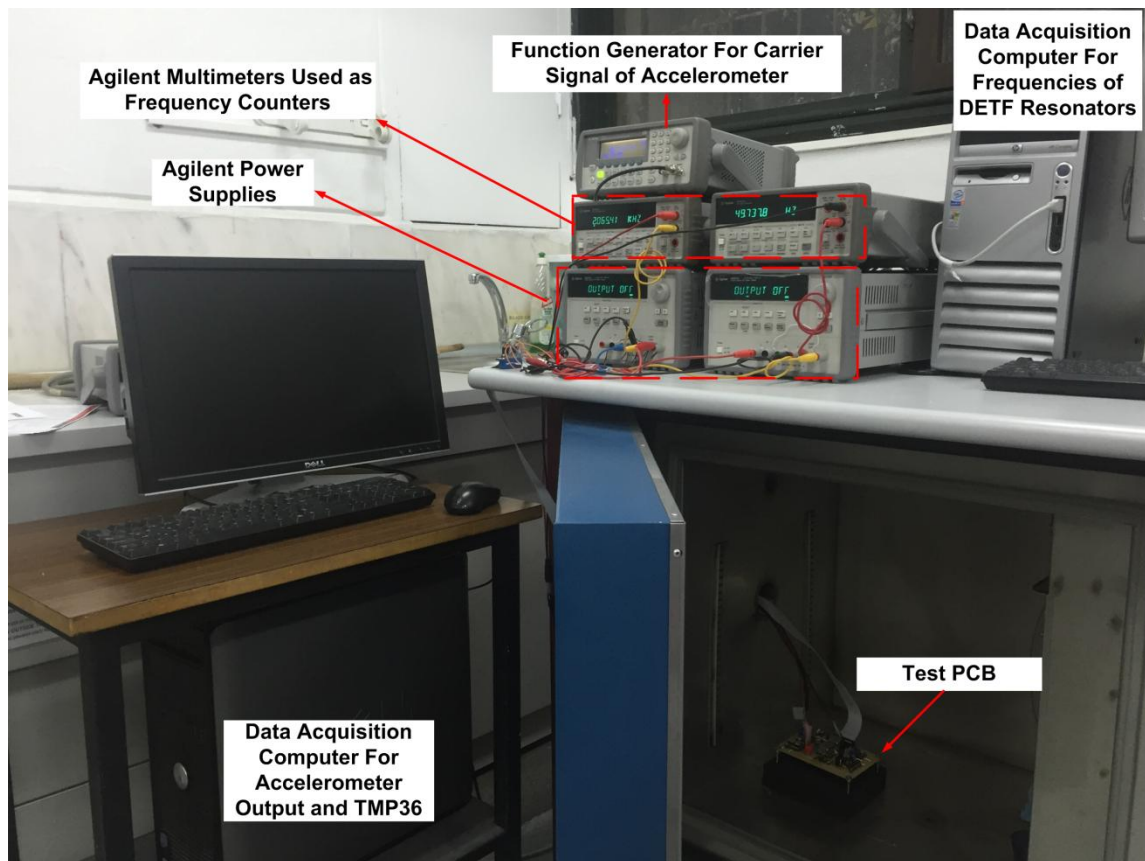


Figure 4.8: Photo of the test setup used in the system-level temperature tests.

System-level temperature tests are performed for the range in between $-20\text{ }^{\circ}\text{C}$ and $60\text{ }^{\circ}\text{C}$. The temperature of the oven can be controlled via the control panel of the oven. The temperature inside the oven can be monitored on the control panel screen. However, temperature tests are held by relying on the output of TMP36 sensor inside the sensor package since it supplies more reliable temperature data of sensor die. Tests are started

when TMP36 sensor shows $-20\text{ }^{\circ}\text{C}$. Then, the oven temperature is set to $60\text{ }^{\circ}\text{C}$, and data collection is started simultaneously when all sensors are operated in closed-loop configuration. Since all sensors can be operated in closed-loop system, real-time data acquisition can be achieved. After a successful data acquisition is achieved from a die, the tests are repeated for another die and so on. The sensors in the same die are quite susceptible the coupling of the signals which made the system fragile to the external factors such as vibration etc. The temperature-controlled oven produces an excess vibration in cooling operations, which causes failure of the data collection. Hence, only the heating data is presented in this study.

4.3 Measurement Results of System-Level Temperature Tests

Measurement results of system-level temperature tests where two MEMS DETF resonators and a MEMS accelerometer present in the same die are operated simultaneously will be demonstrated in this sub-section. First, the measurement results of MEMS DETF resonators will be presented in “frequency versus temperature plots”, then, the measurement results of MEMS accelerometer will be displayed in “accelerometer output versus temperature” plots. Finally, the temperature compensation results obtained by using the previously presented resonator and accelerometer outcomes will be illustrated.

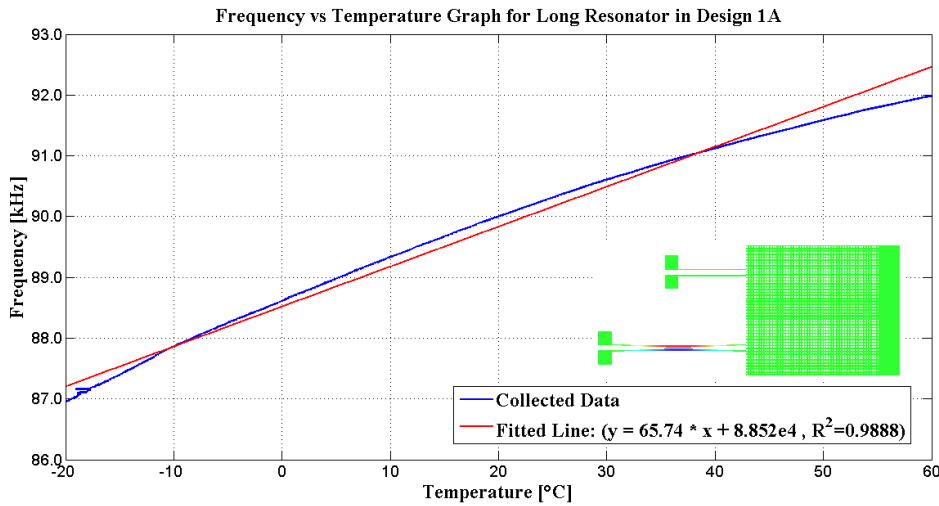
4.3.1.1 System-Level Test Results of MEMS Resonators

System-level tests are conducted in temperature-controlled oven while two MEMS resonators and a MEMS accelerometer present in the same die are operated in the closed-loop configuration. The tests are held in between $-20\text{ }^{\circ}\text{C}$ and $60\text{ }^{\circ}\text{C}$ where these temperatures are monitored from the temperature sensor, TMP36, placed inside the sensor package. The resonance frequency data are collected from the read-out circuits that sustain the self-resonance of the resonators. The common proof mass voltage used for both short and long resonators in each design is selected to be 10 Volts which is determined such that it provides enough gain to the resonance peaks of both resonators,

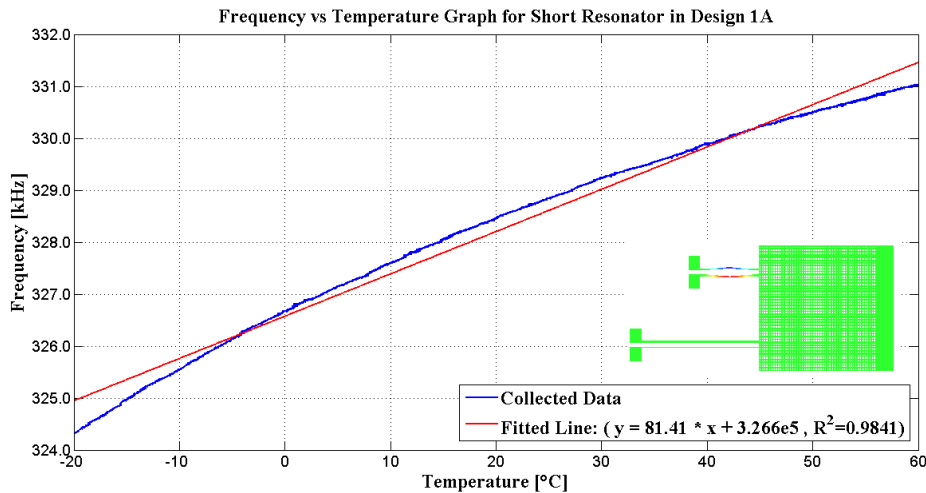
and suppress the nonlinear effects mentioned in the characterization tests of the DETF resonators section. The DC voltages that are converted to square wave signals at the modulator stage to drive the resonators in self-resonance configuration are selected to be 100 mV for the short resonators while it is 10 mV for the long resonators. Data collection of resonance frequency information of the resonators is held by using Agilent Digital Multimeters as a frequency counter. The temperature data is collected from TMP36 by means of the data acquisition (DAQ) computer. The frequency change versus temperature graphs are then plotted by means of MATLAB software by using the collected data from resonators and the temperature sensor data. The measurement results will be presented as “frequency versus temperature graphs” for each resonator design in the following subsections. The temperature coefficient of frequency (TCf) is the figure of merit for the temperature sensitivity of each resonator. Hence, average TCf values are also calculated for the related resonator by utilizing a fitted line to the frequency versus temperature graph. The fitted line equations are also given in the legends of figures as well as the R^2 values of the fitted lines showing the goodness of the fitting processes. The frequency information at 25 °C is used in the calculations of TCf since TCf also depends on the nominal frequency of the resonator. The measurement results of the resonators are also presented as temperature look-up plots which indicates the temperature equivalence of the resonator frequencies, i.e., temperature versus frequency graphs are plotted to create the temperature look-up plots. These look-up plots are necessary for the users who will use the resonators as temperature sensors as mentioned in the objectives of this thesis study. The second order polynomial fit is utilized in these temperature look-up plots in order to minimize the fitting errors. The counterpart equation of the fitted curve, which is presented in the related figures as well as the R^2 values, shows the empirical relationship between the frequency and temperature for the related resonator. These curve equations allow the user to calculate the temperature for the given frequency of the resonator.

4.3.1.2 System-Level Test Results of MEMS Resonators in Design 1A

System-level test results of short and long MEMS resonators in Design 1A are presented as frequency versus temperature graphs prepared by using MATLAB software. Figure 4.9 illustrates the resonance frequency change of the related resonator under temperature change.



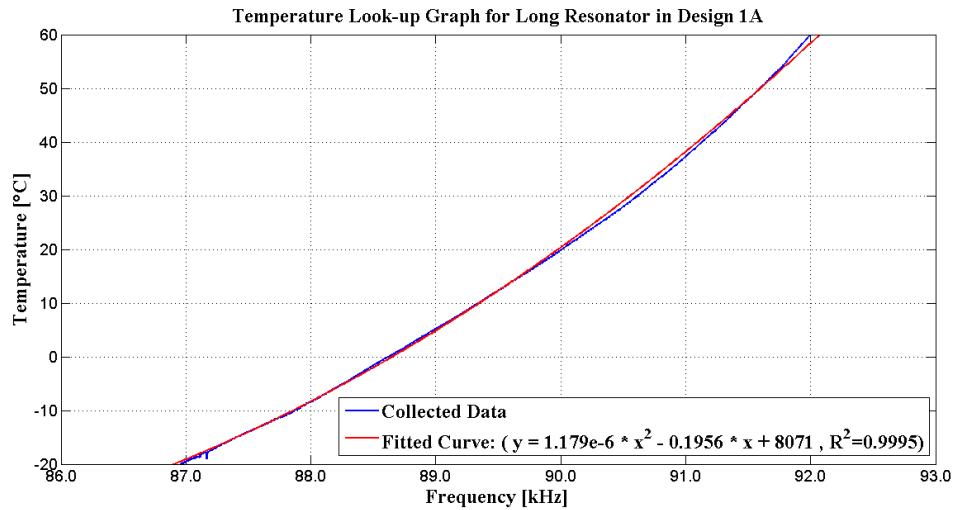
(a)



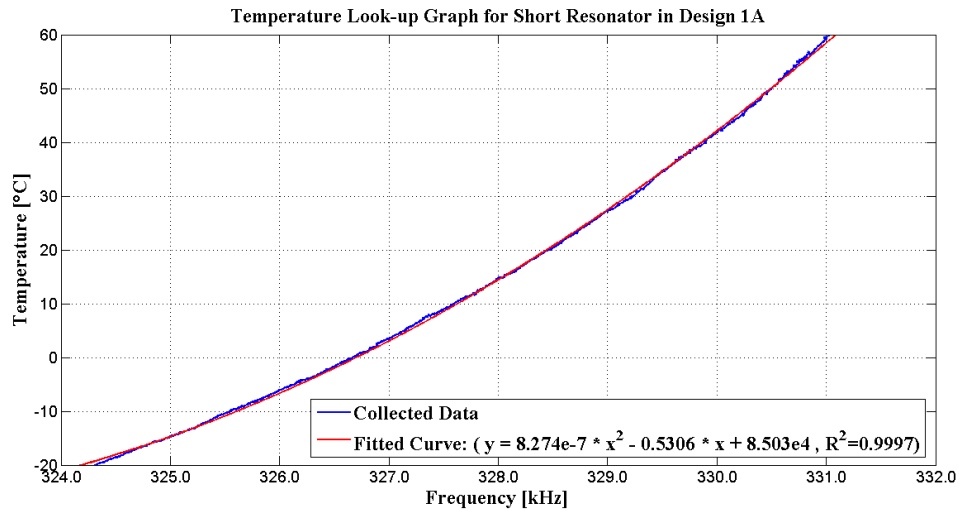
(b)

Figure 4.9: a) System-level test result of the long DETF resonator in Design 1A. The resulting TCf of the long DETF resonator is calculated as 730 ppm/K. b) System-level test result of the short DETF resonator in Design 1A. The resulting TCf of the short DETF resonator is calculated as 248 ppm/K.

Figure 4.10 presents the temperature look-up plots for the resonators in Design 1A together with the equation of the fitted curve enabling the user to estimate the temperature by using the frequency information of the related resonator.



(a)



(b)

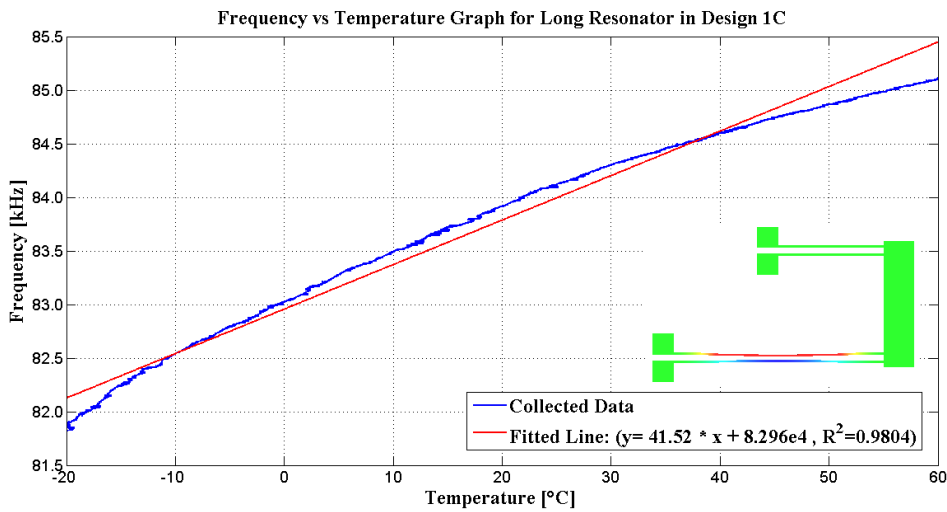
Figure 4.10: Temperature look-up graph **a)** for the long DETF resonator, and **b)** for the short DETF resonator in Design 1A.

The calculated TCf for the long resonator in Design 1A is 730 ppm/K whereas the TCf of the short resonator is found as 248 ppm/K. These values are in good agreement with

the analytical model and thermal simulation results. The comparison table can be found below in Table 4.3.

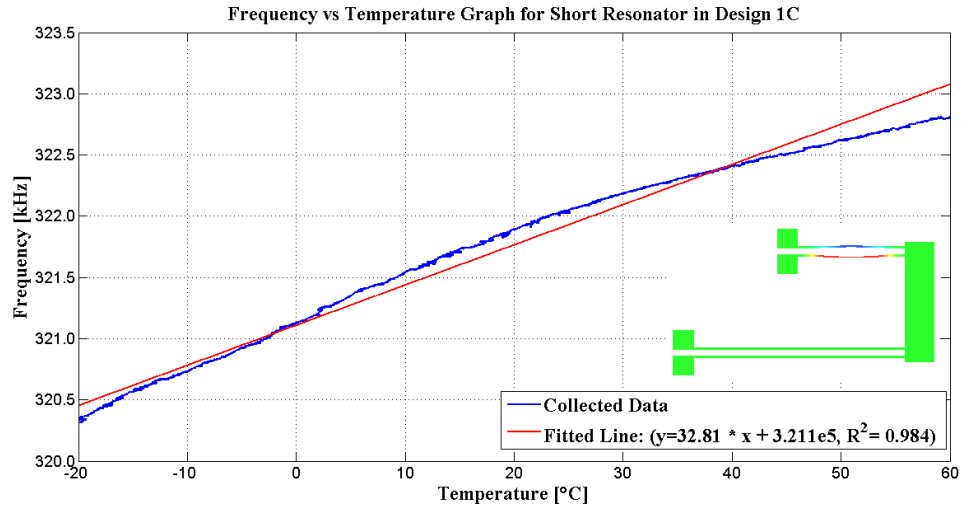
4.3.1.2 System-Level Test Results of MEMS Resonators in Design 1C

System-level test results of short and long MEMS resonators in Design 1C are exhibited as frequency versus temperature graphs prepared by using MATLAB software. Figure 4.12 presents the resonance frequency change of the related resonator under temperature change with a fitted line to calculate the average TCf of the related resonator.



(a)

Figure 4.11: a) System-level test result of the long DETF resonator in Design 1C. The resulting TCf of the long DETF resonator is calculated as 497 ppm/K.

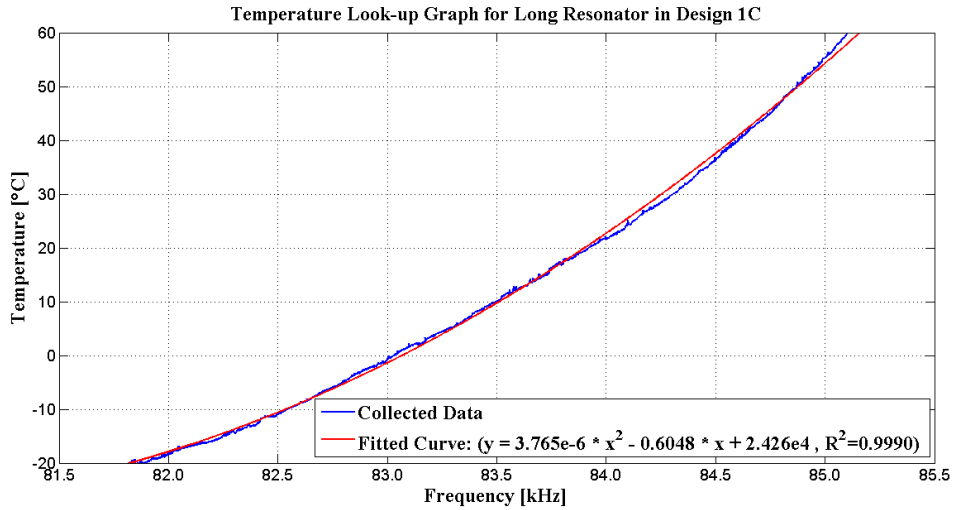


(b)

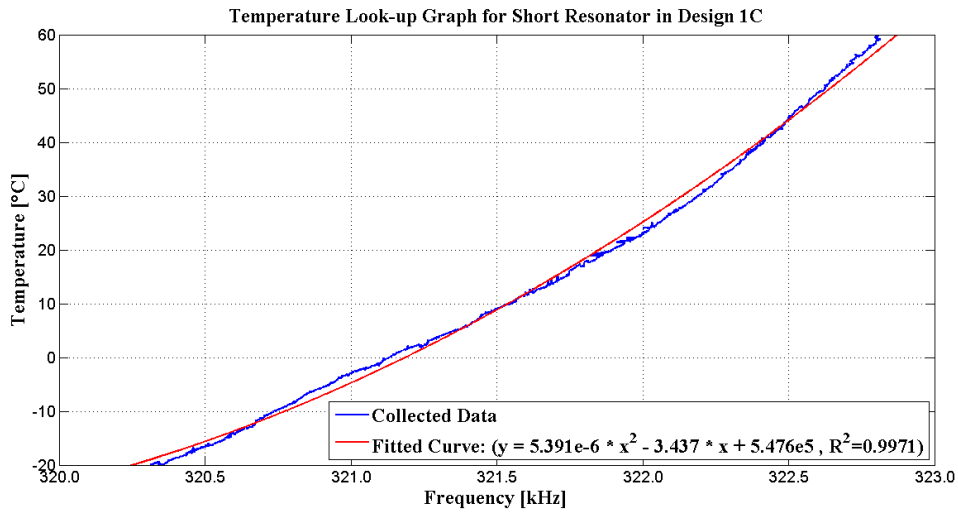
Figure 4.12 (continued): b System-level test result of the short DETF resonator in Design 1C. The resulting TCf of the short DETF resonator is calculated as 102 ppm/K.

The temperature look-up plots for the resonators in Design 1C are illustrated in Figure 4.13 including the equation of the fitted curve for the calculation of the temperature by using the frequency information of the related resonator.

The calculated TCf for the long resonator in Design 1C is 497 ppm/K whereas the TCf of the short resonator is around 102 ppm/K. These values are in good agreement with the analytical model and thermal simulation results. The comparison table can be found below in Table 4.3.



(a)



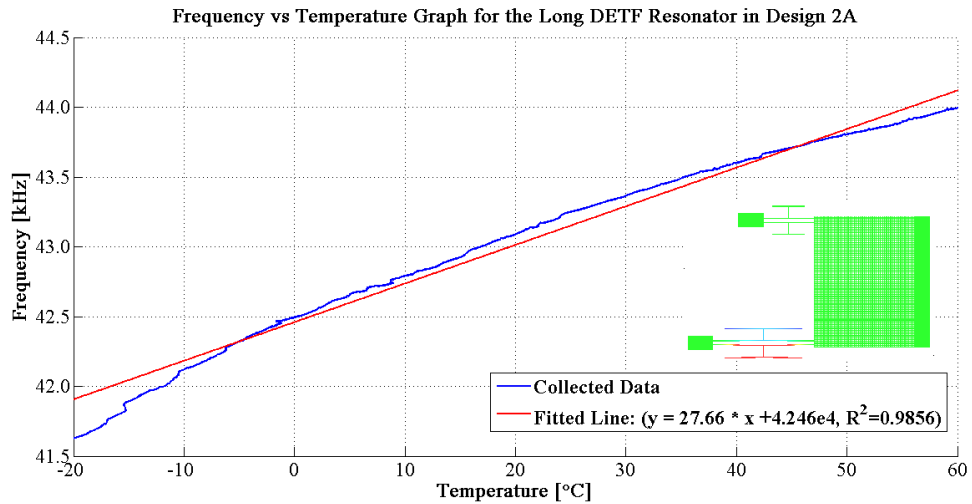
(b)

Figure 4.13: Temperature look-up graph **a)** for the long DETF resonator, and **b)** for the short DETF resonator in Design 1C.

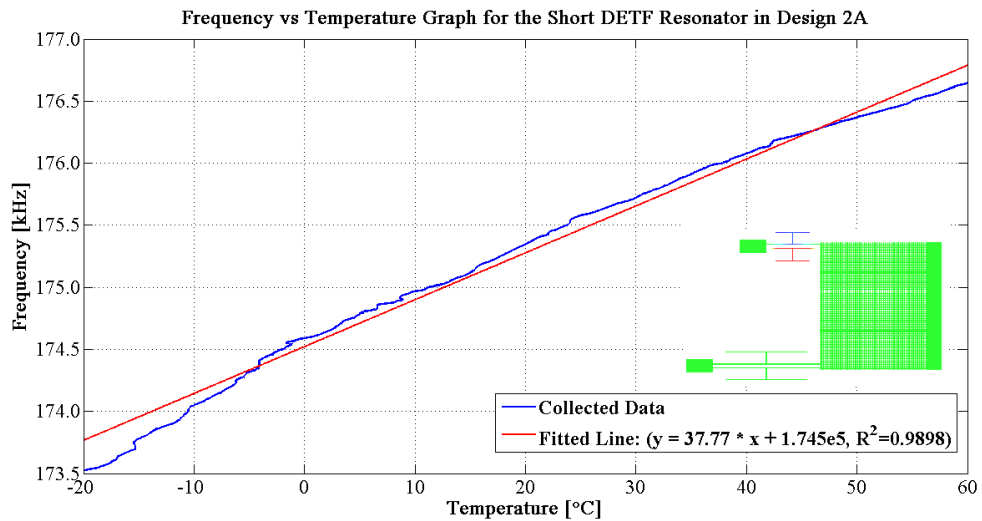
The calculated TCf for the long resonator in Design 1C is 497 ppm/K whereas the TCf of the short resonator is around 102 ppm/K. These values are in good agreement with the analytical model and thermal simulation results. The comparison table can be found below in Table 4.3.

4.3.1.3 System-Level Test Results of MEMS Resonators in Design 2A

The frequency versus temperature graphs prepared to show the measurement results of the system-level tests of short and long MEMS resonators in Design 2A can be seen in Figure 4.14.



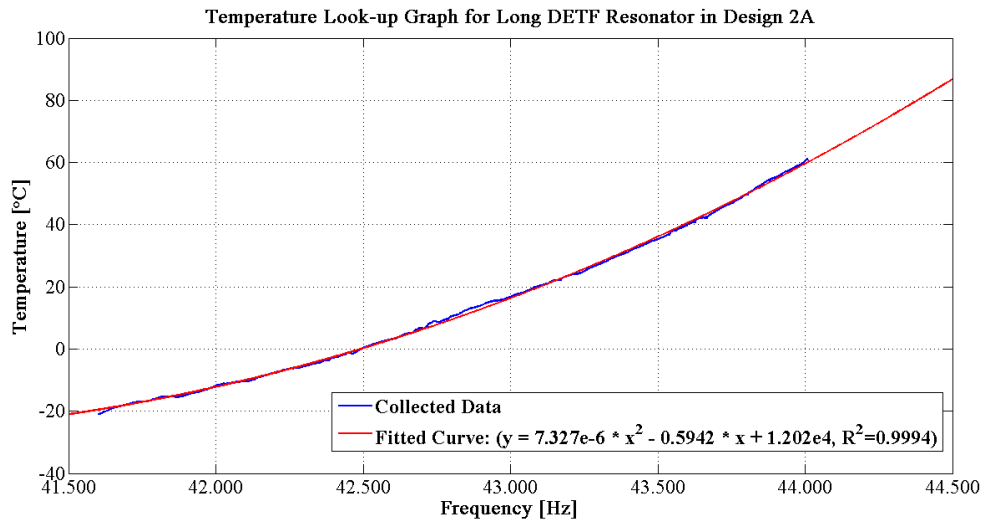
(a)



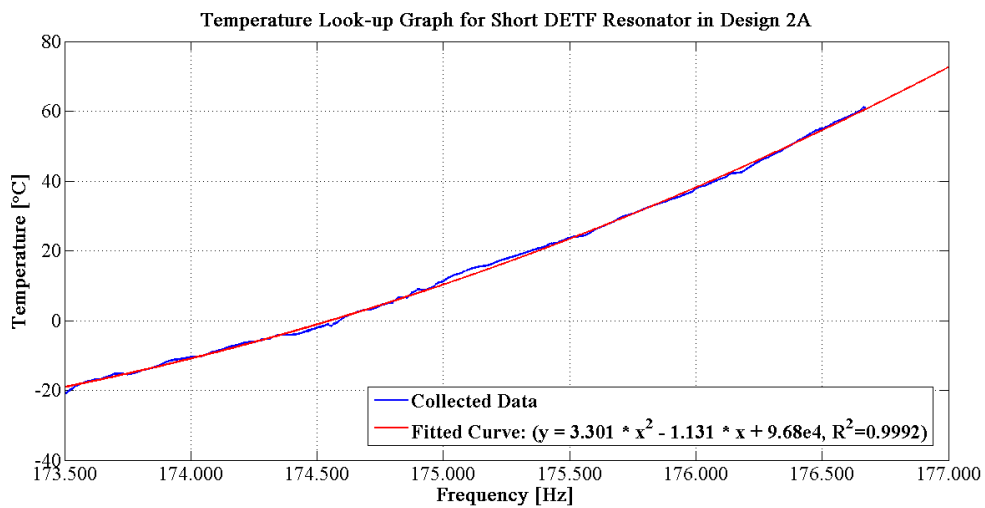
(b)

Figure 4.14: **a)** System-level test result of the long DETF resonator in Design 2A. The resulting TCf of the long DETF resonator is calculated as 636 ppm/K. **b)** System-level test result of the short DETF resonator in Design 2A. The resulting TCf of the short DETF resonator is calculated as 215 ppm/K.

The temperature look-up plots for the resonators in Design 2A are illustrated in Figure 4.15 including the empirical relation between the resonance frequency and the temperature to be used in the conversion of frequency to the temperature.



(a)



(b)

Figure 4.15: Temperature look-up graph **a)** for the long DETF resonator, and **b)** for the short DETF resonator in Design 2A.

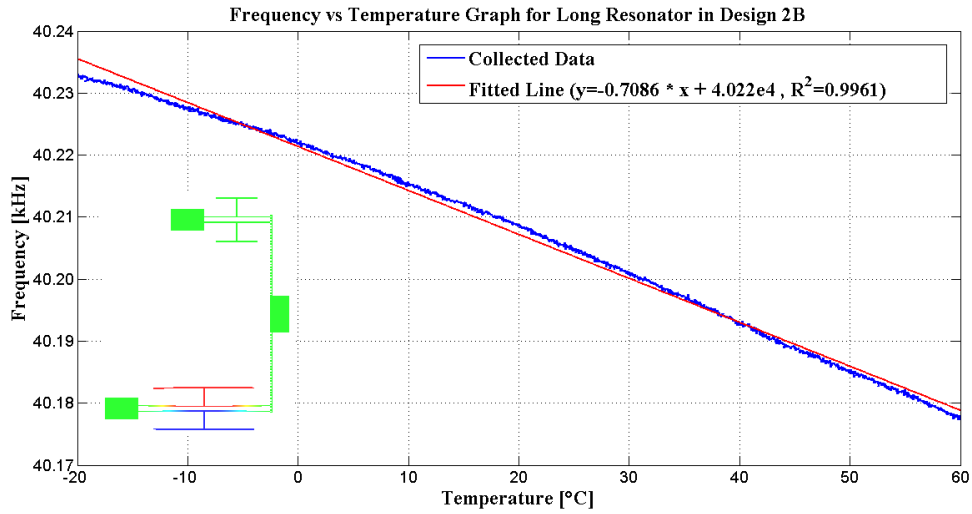
The calculated TCf for the long resonator in Design 2A is 636 ppm/K whereas the TCf of the short resonator is around 215 ppm/K. The comparison of the measurement results,

analytical model results and the thermal simulation results can be found below in Table 4.3.

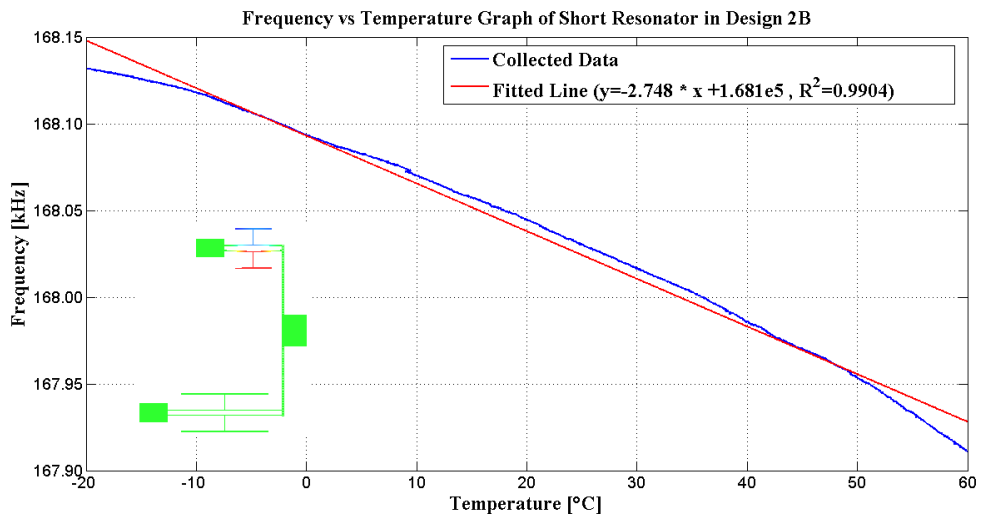
4.3.1.4 System-Level Test Results of MEMS Resonators in Design 2B

The frequency versus temperature graphs prepared to show the measurement results of the system-level tests of short and long MEMS resonators in Design 2B can be seen in Figure 4.16 while the temperature look-up plots for the resonators in Design 2B are presented in Figure 4.17 including the empirical relation between the resonance frequency and the temperature.

The temperature look-up plots for the resonators in Design 2B are illustrated in Figure 4.17 including the empirical relation between the resonance frequency and the temperature to be used in the conversion of frequency to the temperature.

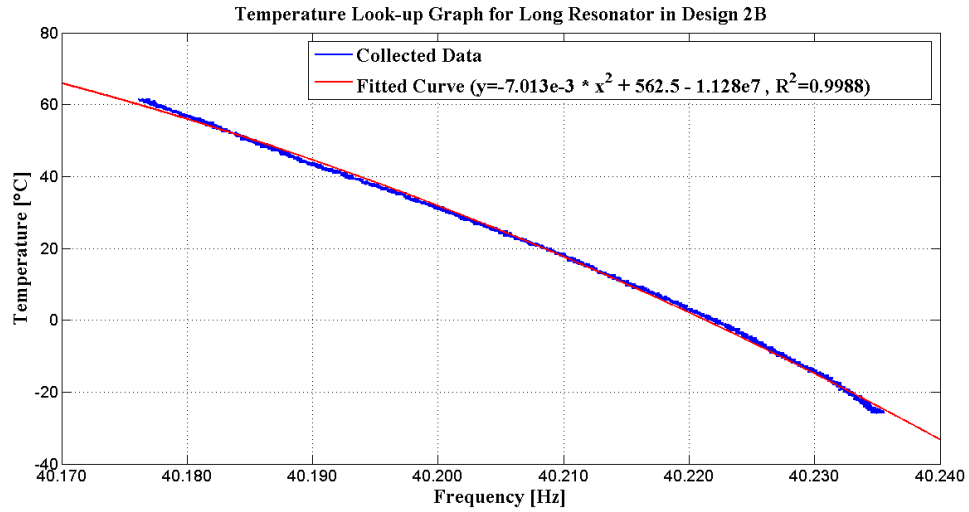


(a)

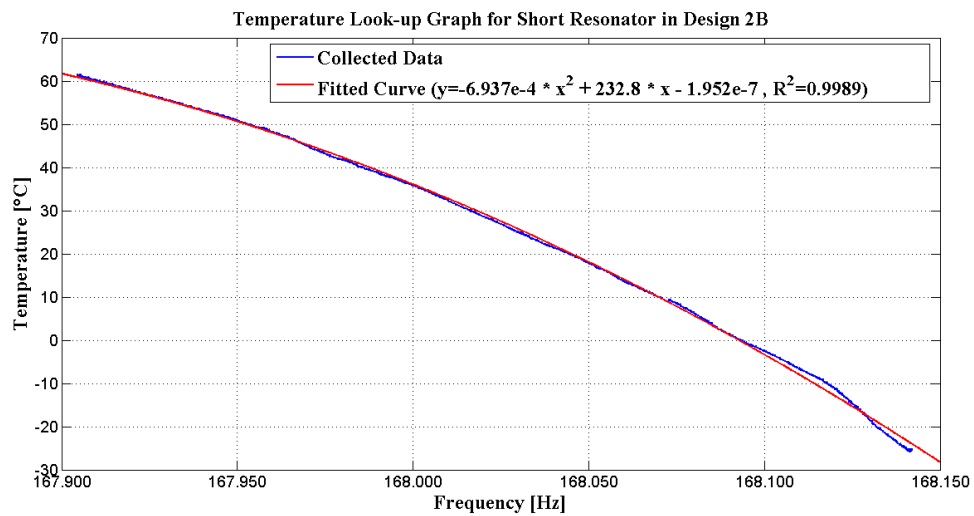


(b)

Figure 4.16: **a)** System-level test result of the long DETF resonator in Design 2B. The resulting TCf of the long DETF resonator is calculated as -18 ppm/K. **b)** System-level test result of the short DETF resonator in Design 2B. The resulting TCf of the long DETF resonator is calculated as -17 ppm/K.



(a)



(b)

Figure 4.17: Temperature look-up graph **a)** for the long DETF resonator, and **b)** for the short DETF resonator in Design 2B.

The calculated TCf for the long resonator in Design 2B is -18 ppm/K whereas the TCf of the short resonator is around -17 ppm/K. The comparison of the measurement results, analytical model results and the thermal simulation results can be found below in Table 4.3. The discussions on the measurement results belonging to the resonant MEMS temperature sensors are available after Table 4.3.

Table 4.3: Summary of all results including mathematical model results, thermo-mechanical simulation results and measurement results of MEMS DETF results utilized in this thesis study.

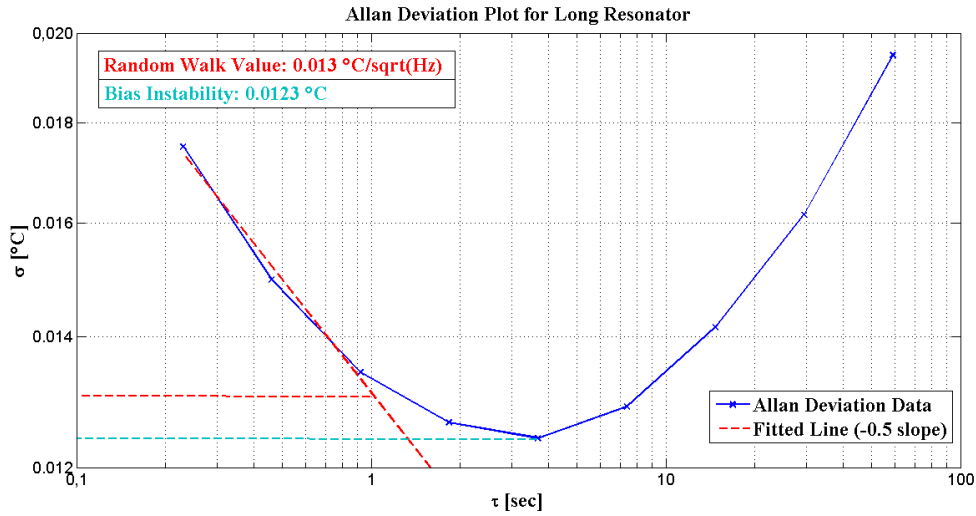
Quantity	Temperature Coefficient of Frequency [ppm/K]							
	Design 1A		Design 1C		Design 2A		Design 2B	
	Short DETF	Long DETF	Short DETF	Long DETF	Short DETF	Long DETF	Short DETF	Long DETF
Mathematical Model Results	203	622	51	305	206	623	-30	-29
Thermal Simulation Results	172	638	115	337	180	697	-30	-31
Measurement Results	248	730	102	497	215	636	-17	-18

The overall results obtained from the resonant MEMS temperature sensors in this thesis are summarized in Table 4.3. The mathematical model results and the test results have shown quite good agreement with small deviations. The reason behind the discrepancies between the analytical model results and measurement results is mainly the fabrication imperfections, i.e., inevitable undercut resulting from the lithography processes, DRIE steps, wet etch processes etc. The undercuts directly affect the sensor properties such as spring constant, mass, sensitivity etc, which reflects as a change in TCf of the DETF resonators. Since the undercut amount and profile occurred on the sensor structures cannot be known precisely, the ultimate effects on TCf can only be guessed. However, the estimated TCf values by using mathematical model are a bit lower than the measurement results, which also supports the argument of that the undercuts could be responsible for the discrepancies because the undercuts leads to a decrease mechanical spring constants of the devices and hence, the natural frequencies. The deviations seen in thermal simulation results are basically coming from inappropriate meshing. The thermal simulations took 1.5-2 days to be completed since the whole chip including the cap and the substrate rather than the sensor structure is modeled. Hence, with a meticulous convergence study to find the appropriate mesh element size for each temperature sensor design, the discrepancies between the measurement results and thermal simulation results can be eliminated although that would need too much time

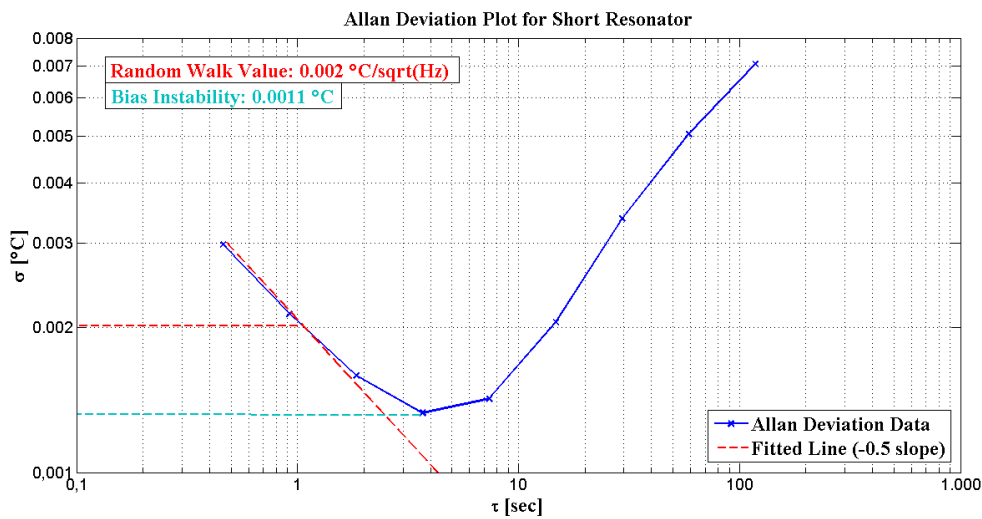
and effort on this issue. All in all, it can be concluded from Table 4.3 that the mathematical model results and thermal simulation results are in good agreement with the measurement results.

The resolution of the offered temperature sensor designs can be found by using Allan deviations of the frequency output of the DETF resonators. The signal coupling is the major problem faced during simultaneous operation of the sensors. To overcome this issue, the frequency output data were collected while the accelerometer turned off. Figure 4.18 below illustrates the result of the Allan-deviation plot obtained from the DETF resonators in Design 2A.

Minimum detectable temperature values are determined by using the bias instability values which are 0.0123 °C and 0.0011 °C for 4 seconds integration time for the long and short DETF resonators, respectively. The better resolution achieved by the short DETF resonator despite its less TCf value is the outcome of high signal-to-noise ratio of the short DETF resonator due to the relatively higher magnitude of the DC signal fed to the modulator to create the square wave signal as drive signal (100 mV). This signal is 20 mV for the long resonator which results with noisier data for the long DETF resonator.



(a)



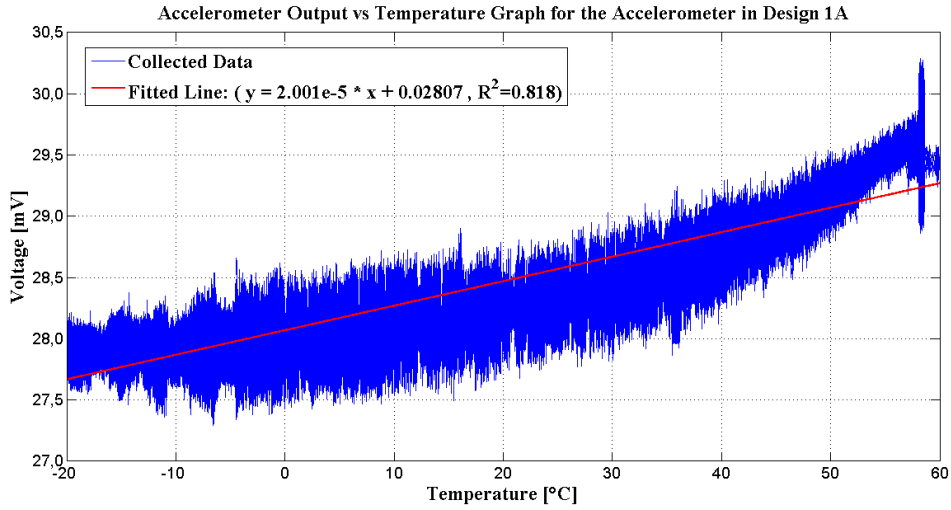
(b)

Figure 4.18: Allan-deviation plots **a)** for the frequency output of long DETF resonator in Design 2A, **b)** for the frequency output of short DETF resonator in Design 2A. Minimum detectable temperature values are determined by using the bias instability values which are 0.0123 °C for 4 seconds integration time and 0.0011 °C for 4 seconds integration time for the long and short DETF resonators respectively.

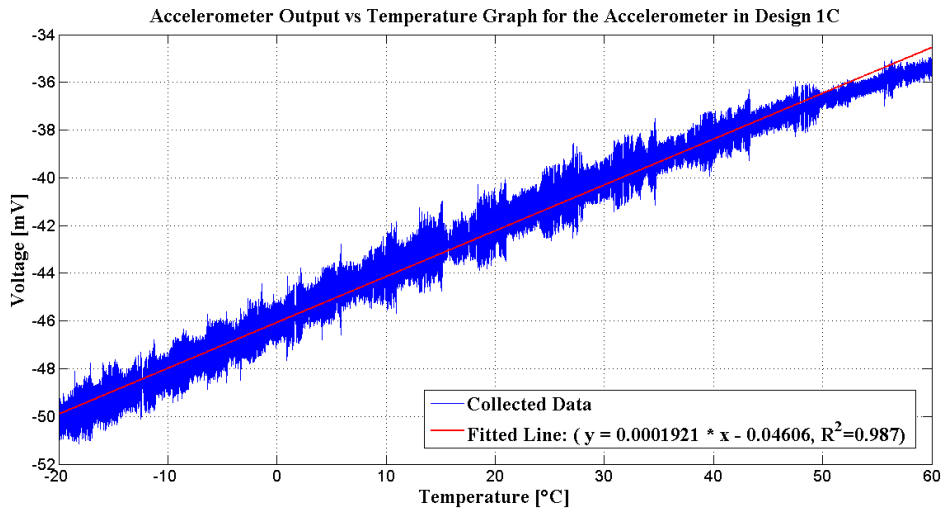
4.3.2 System-Level Test Results of MEMS Accelerometers

System-level tests are conducted in the temperature-controlled oven while two MEMS resonators and a MEMS accelerometer present in the same die are operated in the closed-loop configuration as it was mentioned earlier. The test results of MEMS accelerometer are collected from the controller output in the analog read-out circuit of the accelerometer. The accelerometer is operated in the closed configuration under zero-g condition during the system-level tests, i.e., the accelerometer started to operate in closed-loop and left inside the oven on a straight plane exposed of no acceleration. The proof mass voltage supplied to both electrodes is 1 Volt while the carrier signal fed to the electrodes and the modulator is selected as 20 kHz during the closed-loop operation of the accelerometers. The relevant scale factors of the accelerometers, together with the range of the accelerometers are presented in Table 4.4. Figure 4.20 presents the output of the accelerometers present in the same die with the resonators under changing temperature.

The output of the accelerometer is expected to drift with the changing temperature. The reasons of the drift are mentioned in Section 2.5. This drift depends on the expansion/contraction of the sensing element structures, i.e., the capacitive finger structures, spring structures etc., which leads to a change in the capacitive gaps. The change in the capacitive gap of each electrode directly affects the electrostatic forces produced by the electrodes, which are also utilized to keep the proof mass in equilibrium by means of the controller output of the accelerometer. Furthermore, it is known that a stress occurs on the sensor structures due to different thermal expansion coefficients of the substrate material (glass) and the sensor structure material (single crystal silicon). The stress over the sensing element structures has effects on the accelerometer output [53] since it may disturb the equilibrium point of the proof mass when in closed-loop operation. Hence, the temperature change is expected to trigger a drift in the controller output of the accelerometer. Moreover, it should be noted that the accelerometer output shift is the result of the exposure of whole test PCB including the sensor, read-out circuit and connection cables. There are also the temperature dependent material property effects of the components in the read-out circuit, such as resistors, capacitors, op-amps etc, which may influence the accelerometer output drift.

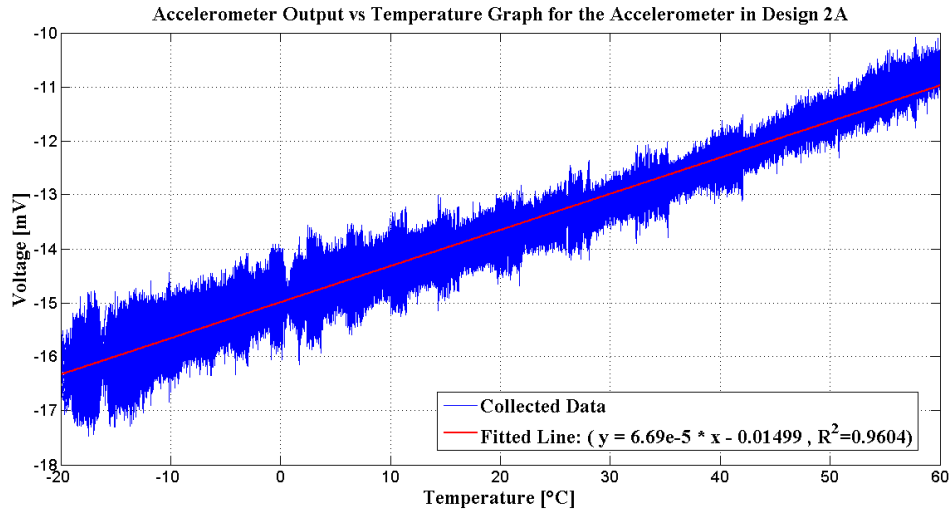


(a)

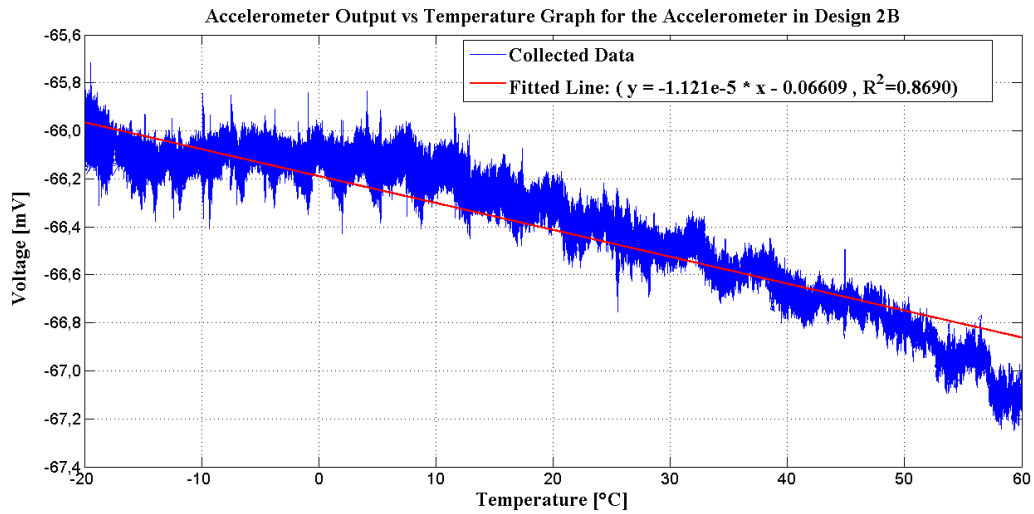


(b)

Figure 4.19: a) System-level temperature test result of the MEMS accelerometer in Design 1A. The result shows the temperature dependence of $133 \mu\text{g}/^\circ\text{C}$ for this accelerometer. b) System-level temperature test result of the MEMS accelerometer in Design 1C. The results show that the temperature dependence of this accelerometer is $1,164 \mu\text{g}/^\circ\text{C}$.



(c)



(d)

Figure 4.20 (continued): *c)* System-level temperature test result of the MEMS accelerometer in Design 1A. The result shows the temperature dependence of $417 \mu\text{g}/^\circ\text{C}$ for this accelerometer. *d)* System-level temperature test result of the MEMS accelerometer in Design 1A. The results show that the temperature dependence of this accelerometer is $-72 \mu\text{g}/^\circ\text{C}$.

The temperature dependence of the accelerometer outputs is calculated as averages by using the fitted lines shown in the figures and the scale factors of the accelerometers to express the temperature dependence in terms of acceleration ($\text{g}/^\circ\text{C}$). The line equations of the fitted lines are also presented in the figures above. The estimated average

temperature dependences of the accelerometers are exhibited in Table 4.5. The temperature dependence of the accelerometer outputs will be eliminated by using the resonance frequency data of the resonators. This temperature compensation method and the compensated accelerometer output data will be presented in the next section.

The noise performances of the accelerometers presented in this study are also examined by collecting the output data under zero-g condition out-of the temperature controlled oven. The collected noise data are then processed by using the Alavar 5.2 software. Alavar utilizes the Allan Variance analysis which determines the velocity random walk (VRW) and bias instability (BI) performances of the accelerometers. The detailed information about the Alavar analysis can be found in [59]. The results can be examined in Allan deviation plots of all accelerometers used in this study are presented in Figure 4.21.

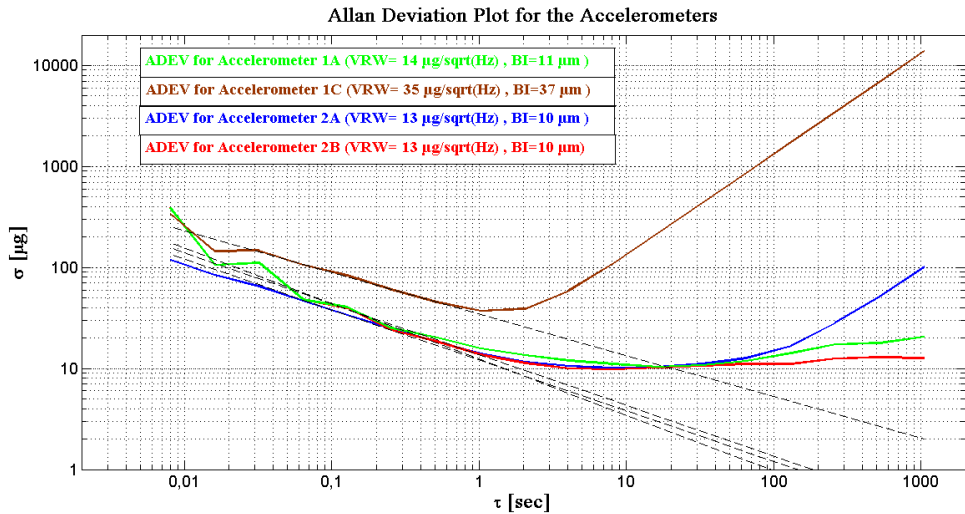


Figure 4.21: Allan deviation plots for the accelerometers used in this thesis study.

When the Allan-deviation plots are examined, it is observed that the bias drift of Accelerometer 1C is abnormally large, which may be the reason of the high temperature sensitivity of Accelerometer output as seen in Figure 4.20 (b). Although the sensing element structures are the same for each accelerometer utilized in this thesis study, the metal routing may show differentiation in each sensor die. This may be reason of excess bias drift of the accelerometer 1C. On the other hand, the accelerometers 1A, 2A and 2B

show quite elegant noise performances: bias instability of 10 μg sustained up to 100 seconds integration time and velocity random walk of 13 $\mu\text{g}/\sqrt{\text{Hz}}$ are achieved with these accelerometers. The other sensor characteristics belonging to the accelerometers can be seen in Table 4.4 below.

Table 4.4: Summary of the sensor characteristics of the MEMS accelerometers used in this thesis study.

Accelerometer Type	Velocity Random Walk [$\mu\text{g}/\sqrt{\text{Hz}}$]	Bias Instability [μg]	Scale Factor [mv/g]	Dynamic Range (FSR/HSR) [dB]	Range [$\pm\text{g}$]
Accelerometer 1A	14	11	150	117 / 111	6.7
Accelerometer 1C	35	37	164	108 / 102	6.1
Accelerometer 2A	13	10	145	118/ 111	6.9
Accelerometer 2B	13	10	155	117 / 111	6.5

4.3.3 Temperature Compensation of Accelerometer Output by Using Resonator Data

Temperature compensation of the accelerometer output is handled for each accelerometer present in each design by using the frequency information of the long resonator in the same die. Accelerometer output data are processed in Matlab environment where the collected data are imported. The accelerometer output can be expressed as the acceleration term, offset term and the temperature term as follows:

$$O_{uncomp} = a SF + T TCO + o_b \quad (4.1)$$

Where a is the applied acceleration, T is temperature, SF are the scale factor of the accelerometer and TCO is the temperature coefficient of the accelerometer output and o_b is the offset in the accelerometer output. By expressing the temperature in terms of frequency of the long DETF resonator, the accelerometer output can be expressed as follows:

$$O(f) = a SF + (c_1 f^2 + c_2 f + c_3) TCO + o_b \quad (4.2)$$

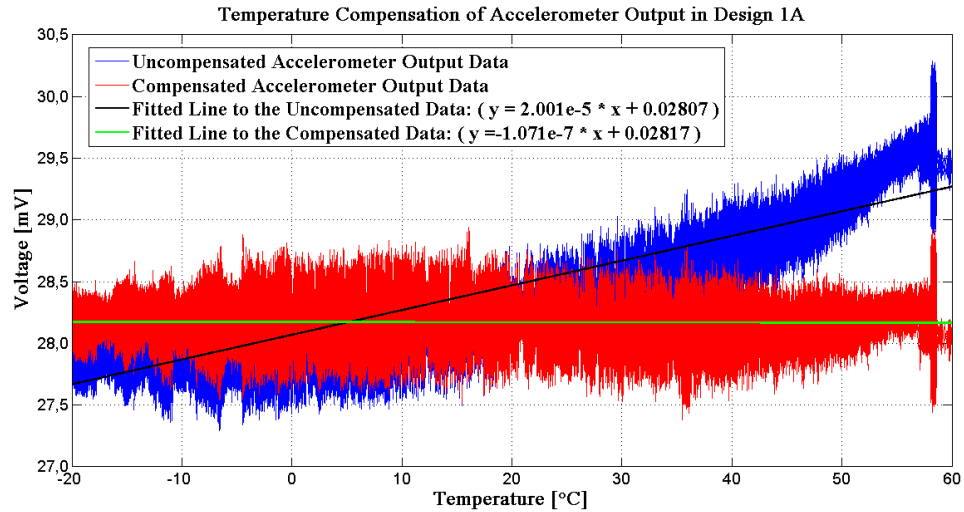
By removing the constants and normalizing the equation for the accelerometer output value at 20 °C, the compensation equation of the accelerometer output can be simplified to the following:

$$O(f) = (c_1 f^2 + c_2 f + c_3) TCo \quad (4.3)$$

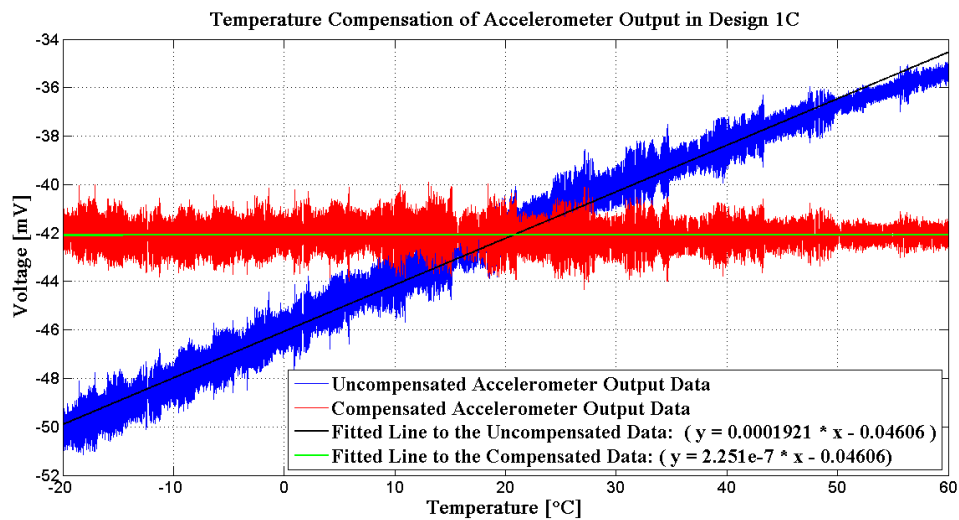
Then by subtracting this compensation equation from the raw acceleration data the compensated accelerometer equation can be obtained as follows:

$$O_{comp} = a SF + T TCo + o_b - (c_1 f^2 + c_2 f + c_3) TCo \quad (4.3)$$

According to the methodology presented above, the compensation is started with obtaining the relation between the accelerometer output and the frequency of the long resonator present in the same die by using the curve fitting tool of Matlab. This relation is then normalized around the accelerometer output at 20 °C. The normalized data is used in the compensation of the accelerometer output data by utilizing simple mathematical operations, i.e., subtraction or addition. Figure 4.23 illustrates the compensated and uncompensated accelerometer data belonging to the accelerometers present in the same die with the DETF resonators.

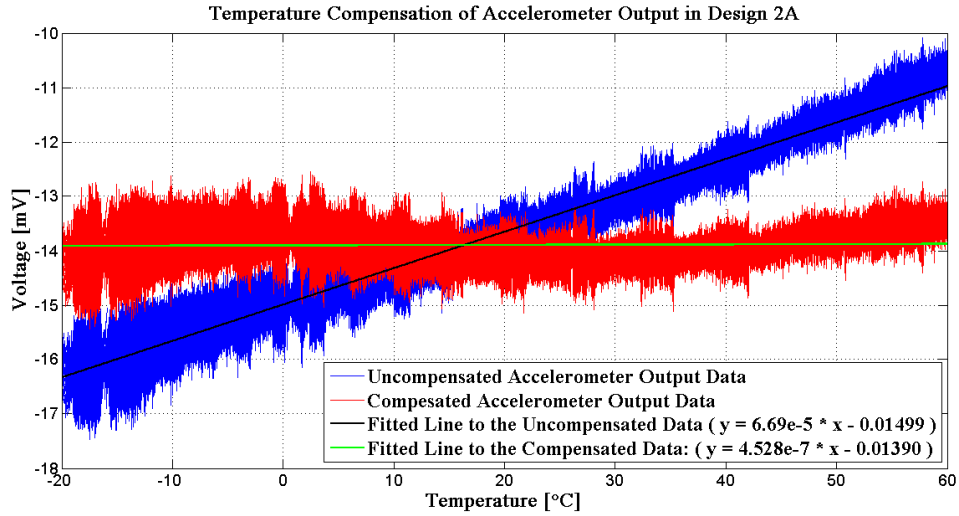


(a)

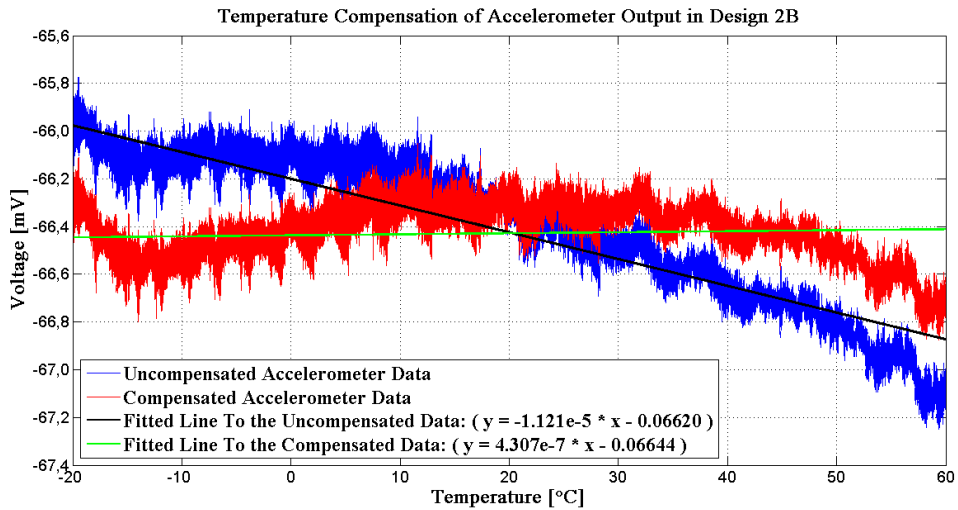


(b)

Figure 4.22: a) Temperature compensation plots of the MEMS accelerometer in Design 1A presenting both compensated and uncompensated accelerometer outputs. The temperature dependence is reduced to $-0.7 \mu\text{g}/^\circ\text{C}$ from $133 \mu\text{g}/^\circ\text{C}$, which indicates 190 times improvement for this accelerometer. b) Temperature compensation plots of the MEMS accelerometer in Design 1A presenting both compensated and uncompensated accelerometer outputs. The temperature dependence is reduced to $1.4 \mu\text{g}/^\circ\text{C}$ from $1,164 \mu\text{g}/^\circ\text{C}$, which indicates 831 times improvement for this accelerometer.



(c)



(d)

Figure 4.23 (continued): *c)* Temperature compensation plots of the MEMS accelerometer in Design 1A presenting both compensated and uncompensated accelerometer outputs. The temperature dependence is reduced to $3.1 \mu\text{g}/^\circ\text{C}$ from $417 \mu\text{g}/^\circ\text{C}$, which indicates 135 times improvement for this accelerometer. *d)* Temperature compensation plots of the MEMS accelerometer in Design 1A presenting both compensated and uncompensated accelerometer outputs. The temperature dependence is reduced to $2.8 \mu\text{g}/^\circ\text{C}$ from $-72 \mu\text{g}/^\circ\text{C}$, which indicates 190 times improvement for this accelerometer.

The fitted lines to the compensated data are used in the calculation how the compensation improves the temperature dependence of the accelerometer output. Table 4.5 presents the results of the temperature compensation process by showing simply the temperature dependences of the accelerometer outputs before and after the compensation.

Table 4.5: Results of the temperature compensation of the MEMS accelerometers utilized in this study.

Accelerometer Type	Temperature Dependencies		Improvement	Scale Factor
	Uncompensated	Compensated		
Accelerometer 1A	133 $\mu\text{g}/^\circ\text{C}$	-0.7 $\mu\text{g}/^\circ\text{C}$	~190 times	150 mV/g
Accelerometer 1C	1,164 $\mu\text{g}/^\circ\text{C}$	1.4 $\mu\text{g}/^\circ\text{C}$	~831 times	165 mV/g
Accelerometer 2A	417 $\mu\text{g}/^\circ\text{C}$	3.1 $\mu\text{g}/^\circ\text{C}$	~135 times	145 mV/g
Accelerometer 2B	-72 $\mu\text{g}/^\circ\text{C}$	2.8 $\mu\text{g}/^\circ\text{C}$	~25 times	155 mV/g

According to the results shown in Table 4.5, the temperature dependences of the accelerometers are improved from 1164 $\mu\text{g}/^\circ\text{C}$ to 1.4 $\mu\text{g}/^\circ\text{C}$. The results show that the performance deteriorations of the accelerometers depending on the temperature fluctuations can be successfully removed by using the frequency information of the resonators co-fabricated with the accelerometers.

To further exemplify the same temperature compensation method, [60] can be examined. to remove bias drift of the accelerometers based on the temperature fluctuations. This method is explained in detail in [60], and the result of corrected noise data can be examined in Figure 4.24.

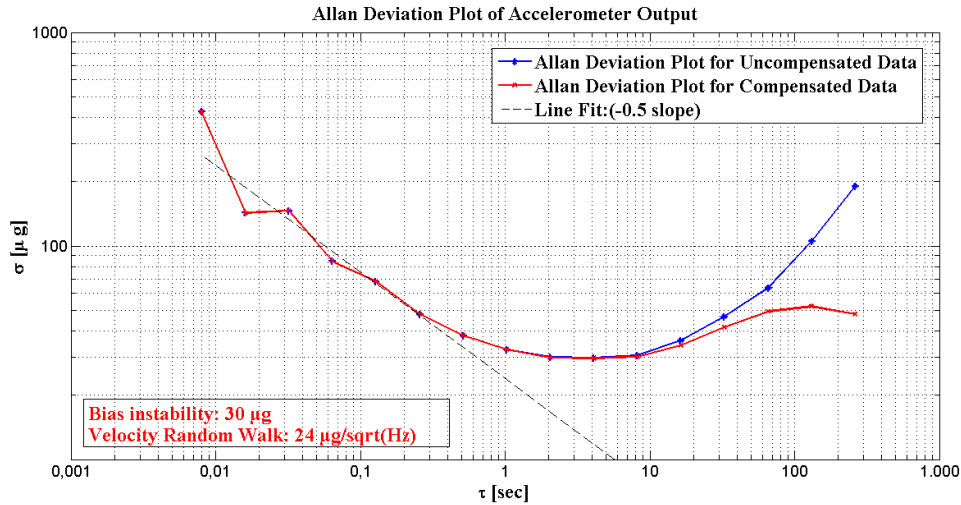


Figure 4.24: Allan deviation plot of the compensated and uncompensated noise data belonging to an accelerometer with the same sensing element structure of those presented in this thesis study [60].

The uncompensated noise data presented in Figure 4.24 shows a ramp after bias instability point due to temperature fluctuation in the environment. This phenomenon, called temperature ramp [54], is removed by the temperature compensation process as shown in compensated noise data in Figure 4.24.

4.4 Summary and Conclusion

This chapter has presented the characterization and system-level tests conducted for the co-fabricated resonant MEMS temperature sensors and capacitive MEMS accelerometers with the significant measurement results. The characterization tests are handled to observe the fabricated sensors in separate tests, i.e., the resonance test for MEMS temperature sensors and CV test for MEMS accelerometers. The results of the characterization tests for DETF resonators show that the fabrication yields good vacuum environment (pressure inside the sensor dies in range of 10-100 mTorr) which corresponds to quality factors in the order of 10000. Also, the closed-loop operation conditions for the resonators are determined by observing the nonlinear behavior of DETF resonators during characterization tests. On the other hand, CV tests are performed to check the functionality of MEMS accelerometers to be utilized in system-level tests. After characterization tests, the sensors to be used in the system-level tests

are selected. The testing equipment preparations are depicted in separate sections with detailed explanations and supplementary figures.

The system-level temperature tests are held in between $-20\text{ }^{\circ}\text{C}$ and $60\text{ }^{\circ}\text{C}$ by employing a temperature-controlled oven. Temperature monitoring is provided via a commercial temperature sensor placed inside the sensor package to achieve more precise measurements. Three sensors, two DETF resonators used as temperature sensor and an accelerometer integrated on the same chip, are operated simultaneously in closed-loop configuration in order to realize the real-time data acquisition from sensors. The measurement results of the system-level tests are illustrated separately for each sensor together with the extracted key parameters such as TCf and temperature dependencies for the MEMS temperature sensors and accelerometers, respectively. TCf values of 730 ppm/K and 636 ppm/K are achieved for the long DETF resonators in Design 1A and Design 2A, respectively, while 248 ppm/K and 215 ppm/K are the results of short DETF resonators in Design 1A and Design 2A, respectively. With the results presented in Table 4.3, the effectiveness of the strain-amplifying beam presented in Design 1A and Design 2A can be observed. According to the measurement results, the strain-amplifying beam provides up to 2.4 times improvement when compared to doubly-clamped DETF resonators (Design 1C), and up to 35 times improvement when compared to the one-end-free DETF resonators (Design 2B). Minimum detectable temperature is determined as 1.1 mK for the short DETF resonator in Design 2A, which points out a good resolution when compared with smart temperature sensors [32]. The measurement results are in good agreement with the thermal simulation results and the mathematical model results for the resonant MEMS temperature sensor designs.

The temperature dependencies of the MEMS accelerometer outputs are also extracted from the obtained data. Reported accelerometer outputs indicate a range of bias drift in between $1,164\text{ }\mu\text{g}/^{\circ}\text{C}$ and $-72\text{ }\mu\text{g}/^{\circ}\text{C}$ which are compensated by using the resonance frequency information of long DETF co-fabricated with the sensing element of the accelerometers. After temperature compensation, the bias drift in $-20\text{ }^{\circ}\text{C}$ - $60\text{ }^{\circ}\text{C}$ range is reduced up to $0.7\text{ }\mu\text{g}/^{\circ}\text{C}$ by showing an improvement of up to 830 times. The noise

performances of the MEMS accelerometers used in this study points out the bias instability of $10 \mu\text{g}$, and the velocity random walk of $13 \mu\text{g}/\sqrt{\text{Hz}}$.

Consequently, the proposed resonant MEMS temperature sensors have been successfully operated, and the measurement results prove the effectiveness of the strain-amplifying beam that increases the temperature sensitivity of temperature sensors. Meanwhile, the temperature compensation of MEMS accelerometers on-chip integrated with the MEMS temperature sensors are performed successfully.

CHAPTER 5

CONCLUSION AND FUTURE WORK

The resonance-based high performance MEMS temperature sensors and the temperature compensation of capacitive MEMS accelerometer as the use of MEMS temperature sensors are presented in this thesis study. The detailed operation principles, mechanical design, and electronic circuit simulations are presented for four distinct MEMS temperature sensor design in Chapter 2. Additionally, the brief explanation of mechanical design and analog read-out circuit of the capacitive MEMS accelerometer are presented in Chapter 2. The fabrication process of MEMS resonators and MEMS accelerometers is examined in Chapter 3 while the sensor characterization and system-level temperature test results of MEMS accelerometer and MEMS resonators are presented in Chapter 4 together with the temperature compensation results of MEMS accelerometer. The conclusions of the related work presented in this thesis are summarized as follows:

- The theory of the operation principles of MEMS resonators are examined by explaining the capacitive actuation and detection methods. The effects of electrostatic forces on the mechanical structures of the MEMS resonators such as electrostatic spring constant and the pull-in phenomenon are presented. Similarly, the operation principles of capacitive MEMS accelerometers are introduced briefly by mostly referring to the previous works.
- The use of MEMS resonators as high performance temperature sensors is explained in detail by implementing the thermal strain relations. The mathematical models of four different designs of MEMS temperature sensors

are exhibited in order to compare the performances of each design. Two DETF resonators are placed in each design in order to verify the created mathematical model. On the other hand, the mechanical design of the sensing element of the MEMS accelerometers used in this study is mentioned by focusing on the spring and proof mass designs. Additionally, some sensor characteristics of MEMS accelerometers such as sensitivity of the sensing element ($\partial C/\partial x$), and scale factor are introduced.

- The optimization of the geometric parameters of the MEMS resonators is handled by the help of a GUI created by using Matlab. The GUI helped showing how parameters affect the performance of resonators as the temperature sensors.
- The MEMS resonator structures whose geometric quantities are determined via GUI are modeled and FEM simulations of MEMS resonators are performed by using CoventorWare software. Modal analyses are conducted to analyze the modal behavior of the mechanical structures. Additionally, the thermo-mechanical simulations are also held via CoventorWare, in order to simulate the performance of the resonators as the temperature sensors. For the design analysis of the MEMS accelerometers, the modal analysis of the sensing element is conducted.
- The electronic read-out circuit for MEMS resonators are proposed with schematics and the simulations of the read-out circuit that ensures the self-resonance of the resonators are conducted in LT Spice environment. The simulations showed that the circuits for the presented circuit components function as intended. The read-out circuits designed for the oscillation of the resonators enable real-time data acquisition from the resonators, which means the capability of sensing instant temperature changes has been achieved by the offered MEMS temperature sensor designs.
- The working principles of the analog force-feedback read-out circuit of the MEMS accelerometers are explained in order to supply enough knowledge about the closed-loop operation of the MEMS accelerometers. For the detailed information, the necessary references are given to [48].

- The fabrication process of the MEMS resonators and accelerometers, aMEMS1 process, is described with the process flow. The fabrication results are illustrated by SEM images taken from the fabricated sensor dies.
- The characterization and system-level test procedures are introduced together with the preparation of the test setup. The system-level test results of each resonator in each design are demonstrated in frequency versus temperature plots, where the TCf of the resonators can be calculated as the figure of merit for the temperature sensor designs. The proposed temperature sensor designs have the TCf of 730 ppm/K, and 636 ppm/K for the long DETF resonators in Design 1A and Design 2A. It is seen that the TCf results are in good agreement with the mathematical model thermo-mechanical simulation results.
- The minimum detectable temperature for the short DETF resonator in Design 2A is found as 0.0011 °C, which is estimated by using the Allan-deviation plot of the noise data of short resonator. This value indicates a quite good resolution when compared with the sensors in smart temperature sensor survey [32].
- The temperature look-up graphs are also created to be able to express the temperature in terms of the resonator frequency. The relations between the frequency and the temperature are also given in order for users to be able to calculate the temperature for the associated frequency.
- The temperature dependencies of the accelerometer outputs obtained from system-level tests are also declared in terms of the acceleration per unit temperature. The temperature compensation is handled by using the frequency information of the MEMS temperature sensor present in the same die. The most temperature-dependent accelerometer output has 1,164 $\mu\text{g}/^\circ\text{C}$ sensitivity, which is then reduced to 1.4 $\mu\text{g}/^\circ\text{C}$. This temperature compensation provides 830 times improvement of the temperature dependency of the accelerometer output, which is the best improvement achieved in this thesis study. The noise performances of the accelerometers points out the bias instability of 10 μg and velocity random walk of 13 $\mu\text{g}/\sqrt{\text{Hz}}$.

The reported high performance MEMS temperature sensor designs and temperature compensation of the co-fabricated MEMS accelerometer are the major achievements in

this thesis. The performances and applications of the proposed MEMS temperature sensors and accelerometers can be improved with further research as listed below:

- The sensor structure is made of silicon while the substrate is made of glass in aMEMS1 process utilized in this study. The material selection is quite significant on the performance of the temperature sensors. If the materials of the substrate and the sensor structure are selected so that the difference in thermal expansion coefficients becomes larger than presented in this thesis, the TCf of the resonators can be increased. Besides, if the substrate material has the lower thermal expansion coefficient than the material of the sensor structure has, the sensor performances can be improved with negative TCf values.
- The test circuit used in this thesis is a prototype circuit board fabricated using a milling machine. This prototype circuit caused unexpected failures during the system-level tests due to low circuit board quality. For the ease of data collection and improvement in data quality, a professional printed circuit board (PCB) can be manufactured and used for further research on this topic.
- The minimum detectable temperature values achieved by the current read-out topology and prototype test PCB can be improved by decreasing the noise level on the resonator output.
- The temperature compensation of the accelerometer output is handled by means of software by processing the acquired data from the resonators and accelerometers co-fabricated on the same die. The compensation can be adapted to the closed-loop operation of the accelerometer as the future work to achieve the instant temperature compensation of the accelerometer output.
- The hysteresis analysis is not conducted in the scope of this thesis since the proposed temperature compensation method is not integrated to the closed-loop operation of the MEMS accelerometers. The reason is that temperature-controlled-oven used in the system-level tests produces serious vibration for cooling processes, which deteriorate the collected data of the sensors placed inside. The detailed hysteresis analysis of the presented temperature sensors and the accelerometers can be handled with more robust test setup and test PCB.

REFERENCES

- [1] J. Bouchaud, "High Value MEMS Market Overview," 12 May 2011. [Online]. Available: http://cmp.imag.fr/conferences/dtip/dtip2011/ppt/DTIP_highvalueMEMS_iSuppli_handout.pdf, [Last accessed date: 04 January 2016].
- [2] J.-C. Eloy, "MEMS Industry Evolution: From Devices to Function," 2010. [Online]. Available: http://semiconwest.org/sites/semiconwest.org/files/JC%20Eloy.Yole_.pdf, [Last accessed date: 04 January 2016].
- [3] K. Lightman, "MEMS and Sensor Trends," 2013. [Online]. Available: https://c.ymcdn.com/sites/www.memsiindustrygroup.org/resource/collection/A1DAAF83-11BC-4D42-A98F-BF250C325EE8/MEMS_and_Sensor_Trends_Smaller_Faster_and_Available_to_the_Mass_Market.pdf, [Last accessed date: 04 January 2016].
- [4] Y. Development, "MEMS Markets Status of the MEMS Industry 2015," May 2015. [Online]. Available: http://i-micronews.com/images/Flyers/MEMS/Yole_Status_of_the_MEMS_Industry_April_2015_web.pdf, [Last accessed date: 04 January 2016].
- [5] G. Stemme, "Resonant Silicon Sensors," *Journal of Micromechanics and Microengineering*, vol. 1, no. 2, pp. 113, 1991.

- [6] H. Dessalegn, and T. Srinivas, "Optical MEMS Pressure Sensor Based on Double Ring Resonator," *2013 International Conference on Microwave and Photonics (ICMAP)*, pp. 1-4, Dhanbad, December 2013
- [7] C. Errando-Herranz, F. Niklaus, G. Stemme *et al.*, "A MEMS Tunable Photonic Ring Resonator with Small Footprint and Large Free Spectral Range." *TRANSDUCERS 2015*, pp. 1001-1004, Alaska, USA, 2015.
- [8] W. Guoqiang, X. Dehui, X. Bin *et al.*, "Wafer-Level Vacuum Packaging for MEMS Resonators Using Glass Frit Bonding," *Journal of Microelectromechanical Systems*, vol. 21, no. 6, pp. 1484-1491, 2012.
- [9] M. Rinaldi, H. Yu, C. Zuniga *et al.*, "High Frequency AlN MEMS Resonators with Integrated Nano Hot Plate for Temperature Controlled Operation," *2012 IEEE International Frequency Control Symposium (FCS)*, pp. 1-5, Baltimore, 2012.
- [10] P. Hauptmann, R. Lucklum, and J. Schroder, "Recent Trends in Bulk Acoustic Wave Resonator Sensors," *2003 IEEE Symposium on Ultrasonics*, pp. 56-65, Vol.1.
- [11] R. J. Halford, "Pressure Measurement Using Vibrating Cylinder Pressure Transducer," *Instrument Practice*, vol. 18, pp. 823-829, 1964.
- [12] S. Seok, H. Kim, and C. Kukjin, "An Inertial-grade Laterally-driven MEMS Differential Resonant Accelerometer," *IEEE Sensors 2004*, pp. 654-657 vol.2, Vienna, Austria, 2004.

- [13] Y.-b. Jia, Y.-l. Hao, and R. Zhang, "Double Tuning-fork Resonant Accelerometer," 7th International Conference on Solid-State and Integrated Circuits Technology, pp. 1812-1815 vol.3, 2004.
- [14] R. G. Azevedo, Z. Jingchun, D. G. Jones *et al.*, "Silicon Carbide Coated MEMS Strain Sensor for Harsh Environment Applications," *MEMS 2007 Conference*, pp. 643-646, Hyogo, 2007.
- [15] K. Azgin, T. Akin, and L. Valdevit, "Ultrahigh-Dynamic-Range Resonant MEMS Load Cells for Micromechanical Test Frames," *Journal of Microelectromechanical Systems*, vol. 21, no. 6, pp. 1519-1529, 2012.
- [16] H. A. C. Tilmans, and S. Bouwstra, "A Novel Design of A Highly Sensitive Low Differential-pressure Sensor Using Built-in Resonant Strain Gauges," *Journal of Micromechanics and Microengineering*, vol. 3, no. 4, pp. 198, 1993.
- [17] C. T. C. Nguyen, "MEMS Technology for Timing and Frequency Control," *IEEE Transactions on Ultrasonics, Ferroelectrics, and Frequency Control*, vol. 54, no. 2, pp. 251-270, 2007.
- [18] M. A. Hopcroft, M. Agarwal, K. K. Park *et al.*, "Temperature Compensation of a MEMS Resonator Using Quality Factor as a Thermometer," in *MEMS 2006*, pp. 222-225, Istanbul, Turkey, 2006.
- [19] M. A. Hopcroft, "Temperature-stabilized Silicon Resonators for Frequency References," *Ph.D. Thesis*, Stanford University, 2007.
- [20] R. Melamud, S. A. Chandorkar, K. Bongsang *et al.*, "Temperature-Insensitive Composite Micromechanical Resonators," *Journal of Microelectromechanical Systems*, vol. 18, no. 6, pp. 1409-1419, 2009.

- [21] R. Melamud, B. Kim, S. A. Chandorkar *et al.*, “Temperature-compensated High-stability Silicon Resonators,” *Applied Physics Letters*, vol. 90, no. 24, pp. 244107, 2007.
- [22] C. M. Jha, G. Bahl, R. Melamud *et al.*, “Cmos-Compatible Dual-Resonator MEMS Temperature Sensor with Milli-Degree Accuracy,” in *TRANSDUCERS 2007*, pp. 229-232, Lyon, France, 2007.
- [23] C. Chiang, A. B. Graham, E. J. Ng *et al.*, “A Novel, High-resolution Resonant Thermometer Used for Temperature Compensation of a Cofabricated Pressure Sensor,” in *Proc. Solid-State Sensors, Actuat., Microsyst. Workshop*, pp. 54-57, South Carolina, USA, 2012.
- [24] J. C. Salvia, R. Melamud, S. A. Chandorkar *et al.*, “Real-Time Temperature Compensation of MEMS Oscillators Using an Integrated Micro-Oven and a Phase-Locked Loop,” *Journal of Microelectromechanical Systems*, vol. 19, no. 1, pp. 192-201, 2010.
- [25] P. Dufilie, J. V. Adler, and A. Sawyer, “Performances of Monolithic Micro-oven Heated SAW and STW Resonators,” in *2011 IEEE International Ultrasonics Symposium (IUS)*, pp. 87-91, Florida, USA, 2011.
- [26] L. Ming-Huang, C. Chao-Yu, L. Cheng-Syun *et al.*, “A Monolithic CMOS-MEMS Oscillator Based on an Ultra-Low-Power Ovenized Micromechanical Resonator,” *Journal of Microelectromechanical Systems*, vol. 24, no. 2, pp. 360-372, 2015.
- [27] K. E. Wojciechowski, and R. H. Olsson, “A Fully Integrated Oven Controlled Microelectromechanical Oscillator--Part II: Characterization and Measurement,”

Journal of Microelectromechanical Systems, vol. 24, no. 6, pp. 1795 - 1802, 2015.

- [28] Z. Chong, W. Qi-song, Y. Tao *et al.*, "A MEMS Gyroscope Readout Circuit with Temperature Compensation," *NEMS 2010 Conference*, pp. 458-462, Xiamen, 2010.
- [29] Y. Tao, W. Huanming, W. Qisong *et al.*, "A TIA-based Readout Circuit with Temperature Compensation for MEMS Capacitive Gyroscope," *NEMS 2011 Conference*, pp. 401-405, Kaohsiung, 2011.
- [30] C. Pramanik, S. Banerjee, D. Mukherjee *et al.*, "Development of SPICE Compatible Thermal Model of Silicon MEMS Piezoresistive Pressure Sensor for CMOS-MEMS Integration," in *5th IEEE Conference on Sensors 2006*, Daegu, Korea, 2006, pp. 761-764.
- [31] R. G. Azevedo, W. Huang, O. M. O'Reilly *et al.*, "Dual-mode temperature compensation for a comb-driven MEMS resonant strain gauge," *Sensors and Actuators A: Physical*, vol. 144, no. 2, pp. 374-380, 6/15/, 2008.
- [32] K. A. A. Makinwa, "Smart Temperature Sensor Survey," [Online] http://ei.ewi.tudelft.nl/docs/TSensor_survey.xls [Last accessed date: 14 January 2016]
- [33] M. H. Perrott, J. C. Salvia, F. S. Lee *et al.*, "A Temperature-to-Digital Converter for a MEMS-Based Programmable Oscillator With Frequency Stability and Integrated Jitter," *IEEE Journal of Solid-State Circuits*, vol. 48, no. 1, pp. 276-291, 2013.

- [34] M. Shahmohammadi, K. Souri, and K. A. A. Makinwa, "A Resistor-based Temperature Sensor for MEMS Frequency References," *ESSCIRC 2013*, pp. 225-228, Bucharest, 2013.
- [35] N. Inomata, M. Toda, M. Sato *et al.*, "Resonant Thermal Sensor for a Living Cell in Liquid," in *2012 IEEE 25th International Conference on Micro Electro Mechanical Systems (MEMS)*, pp. 108-111, Paris, France, 2012.
- [36] M. Agarwal, S. A. Chandorkar, R. N. Candler *et al.*, "Optimal Drive Condition for Nonlinearity Reduction in Electrostatic Microresonators," *Applied Physics Letters*, vol. 89, no. 21, pp. 214105, 2006.
- [37] M. E. T. University, "Capacitive Sensors," *EE610 Lecture Notes*, pp. 8-13.
- [38] M. M. Torunbalci, S. E. Alper, and T. Akin, "Advanced MEMS Process for Wafer Level Hermetic Encapsulation of MEMS Devices Using SOI Cap Wafers With Vertical Feedthroughs," *Journal of Microelectromechanical Systems*, vol. 24, no. 3, pp. 556-564, 2015.
- [39] A. Torrents, K. Azgin, S. W. Godfrey *et al.*, "MEMS Resonant Load Cells for Micro-mechanical test frames: Feasibility Study and Optimal Design," *Journal of Micromechanics and Microengineering*, vol. 20, no. 12, pp. 125004, 2010.
- [40] V. Kaajakari, T. Mattila, A. Oja *et al.*, "Nonlinear Limits for Single-crystal Silicon Microresonators," *Journal of Microelectromechanical Systems*, vol. 13, no. 5, pp. 715-724, 2004.
- [41] M. A. Hopcroft, W. D. Nix, and T. W. Kenny, "What is the Young's Modulus of Silicon?," *Journal of Microelectromechanical Systems*, vol. 19, no. 2, pp. 229-238, 2010.

- [42] K. Azgin, and L. Valdevit, "The Effects of Tine Coupling and Geometrical Imperfections on the Response of DETF Resonators," *Journal of Micromechanics and Microengineering*, vol. 23, no. 12, pp. 125011, 2013.
- [43] S. E. Alper, "MEMS Gyroscopes for Tactical-Grade Inertial Measurement Applications," *Ph.D. Thesis*, Middle East Technical University, September 2005.
- [44] S. Microelectronics, "High Performance Ultra-Low-Power 3-axis Accelerometer with Digital Output for Industrial Applications," *IIS328DQ Technical Datasheet*, 2015.
- [45] Y. Dong, P. Zwahlen, A. M. Nguyen *et al.*, "Ultra-high Precision MEMS Accelerometer," *TRANSDUCERS 2011*, pp. 695-698, Beijing, 2011.
- [46] T. Kose, Y. Terzioglu, K. Azgin *et al.*, "A Single Mass Two-axis Capacitive MEMS Accelerometer with Force Rebalance," *2015 IEEE International Symposium on Inertial Sensors and Systems*, pp. 1-4, 2015.
- [47] S. Tez, U. Aykutlu, M. M. Torunbalci *et al.*, "A Bulk-Micromachined Three-Axis Capacitive MEMS Accelerometer on a Single Die," *Journal of Microelectromechanical Systems*, vol. 24, no. 5, pp. 1264-1274, 2015.
- [48] Y. Terzioglu, "A High Performance Closed-Loop Analog Readout Circuit for Capacitive MEMS Accelerometers," *M.Sc. Thesis*, Middle East Technical University, September 2015.
- [49] U. Aykutlu, "5th Order Sigma Delta MEMS Accelerometer with Enhanced Linearity," *M.Sc. Thesis*, Middle East Technical University, September 2015.

- [50] Y. Terzioglu, T. Kose, K. Azgin *et al.*, "A Simple Out-of-plane Capacitive MEMS Accelerometer Utilizing Lateral and Vertical Electrodes for Differential Sensing," *IEEE Sensors Conference*, pp. 1-3, Busan, Korea, 2015.
- [51] Y. Terzioglu, S. E. Alper, K. Azgin *et al.*, "A Capacitive MEMS Accelerometer Readout with Concurrent Detection and Feedback Using Discrete Components," *IEEE/ION Position, Location and Navigation Symposium (PLANS 2014)*, pp. 12-15, Monterey, CA, USA, May 5-8, 2014.
- [52] F. Gulmammadov, "Analysis, Modeling and Compensation of Bias Drift in MEMS Inertial Sensors," *4th International Conference on Recent Advances in Space Technologies, RAST '09*, pp. 591-596, Istanbul, Turkey, 2009.
- [53] Y. Hung-Te, S. Yen-Fu, and C. Kuo-Ning, "Research on Packaging Effects of Three-axis SOI MEMS Accelerometer," *16th International Conference on Thermal, Mechanical and Multi-Physics Simulation and Experiments in Microelectronics and Microsystems (EuroSimE)*, pp. 1-4, Budapest, 2015.
- [54] S. A. Zotov, B. R. Simon, A. A. Trusov *et al.*, "High Quality Factor Resonant MEMS Accelerometer With Continuous Thermal Compensation," *IEEE Sensors Journal*, vol. 15, no. 9, pp. 5045-5052, 2015.
- [55] M. M. Torunbalci, E. Tatar, S. E. Alper *et al.*, "Comparison of Two Alternative Silicon-on-Glass Microfabrication Processes for MEMS Inertial Sensors," *Procedia Engineering*, vol. 25, pp. 900-903, 2011.
- [56] M. M. Torunbalci, S. E. Alper, and T. Akin, "Wafer Level Hermetic Encapsulation of MEMS Inertial Sensors Using SOI Cap Wafers with Vertical Feedthroughs," *2014 International Symposium on Inertial Sensors and Systems (ISISS)*, pp. 1-2, California, USA, 2014.

- [57] M. M. Torunbalci, "Development of new, Simple, and Robust Wafer Level Hermetic Packaging Methods for MEMS Sensors," *Ph.D. thesis*, 2015.
- [58] S. Alper, M. Torunbalci, and T. Akin, "Method of Wafer Level Hermetic Packaging with Vertical Feedthroughs," *PCT/TR2013/000298*, 2013.
- [59] N. El-Sheimy, H. Haiying, and N. Xiaoji, "Analysis and Modeling of Inertial Sensors Using Allan Variance," *IEEE Transactions on Instrumentation and Measurement*, vol. 57, no. 1, pp. 140-149, 2008.
- [60] T. Kose, K. Azgin, and T. Akin, "Temperature Compensation of Capacitive MEMS Accelerometer by Using MEMS Oscillator," *Accepted, 2016 IEEE International Symposium on Inertial Sensors and Systems*, 2016.